EXPERIMENTAL AND NUMERICAL INVESTIGATION OF LASER ASSISTED MILLING OF SILICON NITRIDE CERAMICS

by

BUDONG YANG

B. S., Beijing University of Aeronautics and Astronautics, 1992
M.S., Shanghai Jiao Tong University, 1995

AN ABSTRACT OF A DISSERTATION

submitted in partial fulfillment of the requirements for the degree

DOCTOR OF PHILOSOPHY

Department of Industrial and Manufacturing Systems Engineering
College of Engineering

KANSAS STATE UNIVERSITY
Manhattan, Kansas

2009

Abstract

This study experimentally and numerically investigates laser assisted milling (LAMill) of silicon nitride ceramics. Experiments are conducted to study the machinability of Si_3N_4 under LAMill. The effects of temperature on cutting forces, tool wear, surface integrity, edge chipping and material removal mechanisms are investigated. It is shown that when temperature increases, cutting force and tool wear are significantly decreased, surface integrity is improved, chip size is increased and material removal demonstrates more plastic characteristics. The mechanisms of edge chipping at elevated temperature are investigated theoretically and experimentally. When temperature is above the softening point and below the brittle/ductile transition temperature, the mechanism is mainly through softening. When temperature is above the brittle/ductile transition temperature, toughening mechanism contributes significantly to the reduced edge chipping. The coupled effect of softening and toughening mechanisms shows that temperature range between 1200 to 1400°C has the most significant effect to reduce edge chipping.

Distinct element method (DEM) is applied to simulate the micro-mechanical behavior of Si_3N_4. First, quantitative relationships between particle level parameters and macro-properties of the bonded particle specimens are obtained, which builds a foundation for simulation of Si_3N_4. Then, extensive DEM simulations are conducted to model the material removal of machining Si_3N_4. The simulation results demonstrate that DEM can reproduce the conceptual material removal model summarized from experimental observations, including the initiation and propagation of cracks, chip formation process and material removal mechanisms. It is shown that material removal is mainly realized by propagation of lateral cracks in machining of silicon nitride. At the elevated temperature under laser assisted machining, lateral cracks are easier to propagate to form larger machined chips, there are fewer and smaller median cracks therefore less surface/subsurface damage, and crushing-type material removal is reduced. The material removal at elevated temperature demonstrates more plastic characteristics. The numerical results agree very well with experimental observations. It shows that DEM is a promising method to model the micro-mechanical process of machining Si_3N_4.

EXPERIMENTAL AND NUMERICAL INVESTIGATION OF LASER ASSISTED MILLING OF SILICON NITRIDE CERAMICS

by

BUDONG YANG

B. S., Beijing University of Aeronautics and Astronautics, 1992
M.S., Shanghai Jiao Tong University, 1995

A DISSERTATION

submitted in partial fulfillment of the requirements for the degree

DOCTOR OF PHILOSOPHY

Department of Industrial and Manufacturing Systems Engineering
College of Engineering

KANSAS STATE UNIVERSITY
Manhattan, Kansas

2009

Approved by:

Major Professor
Dr. Shuting Lei

Abstract

This study experimentally and numerically investigates laser assisted milling (LAMill) of silicon nitride ceramics. Experiments are conducted to study the machinability of Si_3N_4 under LAMill. The effects of temperature on cutting forces, tool wear, surface integrity, edge chipping and material removal mechanisms are investigated. It is shown that when temperature increases, cutting force and tool wear are significantly decreased, surface integrity is improved, chip size is increased and material removal demonstrates more plastic characteristics. The mechanisms of edge chipping at elevated temperature are investigated theoretically and experimentally. When temperature is above the softening point and below the brittle/ductile transition temperature, the mechanism is mainly through softening. When temperature is above the brittle/ductile transition temperature, toughening mechanism contributes significantly to the reduced edge chipping. The coupled effect of softening and toughening mechanisms shows that temperature range between 1200 to 1400°C has the most significant effect to reduce edge chipping.

Distinct element method (DEM) is applied to simulate the micro-mechanical behavior of Si_3N_4. First, quantitative relationships between particle level parameters and macro-properties of the bonded particle specimens are obtained, which builds a foundation for simulation of Si_3N_4. Then, extensive DEM simulations are conducted to model the material removal of machining Si_3N_4. The simulation results demonstrate that DEM can reproduce the conceptual material removal model summarized from experimental observations, including the initiation and propagation of cracks, chip formation process and material removal mechanisms. It is shown that material removal is mainly realized by propagation of lateral cracks in machining of silicon nitride. At the elevated temperature under laser assisted machining, lateral cracks are easier to propagate to form larger machined chips, there are fewer and smaller median cracks therefore less surface/subsurface damage, and crushing-type material removal is reduced. The material removal at elevated temperature demonstrates more plastic characteristics. The numerical results agree very well with experimental observations. It shows that DEM is a promising method to model the micro-mechanical process of machining Si_3N_4.

Table of Contents

List of Figures

List of Tables

Acknowledgements

First of all, I would like to give thanks to the Lord Jesus. Without His guidance and encouragement, I can't imagine I can finish this work. Thank you, Jesus, for giving me the wisdom, endurance and persistence. Thank you for leading me all the way here.

I would like to express my sincere gratitude to Dr. Shuting Lei, my major professor. Dr. Lei's rigorous scientific attitude impressed me very much. His open-minded research approaches inspired me all the time in my research. I also would like to give special thanks to Dr. Z. J. Pei, who is always ready to give valuable advises and share his abundant experiences and broad knowledge. Dr. Pei is an academic mentor, an advisor for career development and a personal friend whom I can turn to at any time. I must thank God for Dr. Shing I. Chang, an academic and spiritual mentor, a dear brother and a truly family member. Dr. Chang's knowledge in data analysis significantly improved the scientific value of this research. His advice about research approaches will definitely benefit my academic career. His example will encourage me to live a righteous, Godly and peaceful life. I would like to express my gratitude to Dr. X.J. Xin, whose broad knowledge in numerical modeling impressed me very much. His valuable advice helped to refine the numerical model in this study. I also thank Dr. Glenn Horton-Smith from Physics Department to serve as the chairperson of my examining committee.

I would like to thank the constant support from our department head Dr. Bradley A. Kramer. His unchanging support triumphs over my weakness and encourages me to achieve this goal. I also thank the kind assistance from our department staff and the valuable help from Mr. Timothy W. Deines.

Thank the Lord for my wife Lin Xu, my sons Daniel and Samuel. Without my wife's constant support and encouragement, it is impossible for me to achieve this goal. Family is the place where happiness overflows, where I can find fun and peace, and where I can re-strengthen myself to face the daily challenges in my life and research. Special thanks also go to my parents, my sisters, my parents-in-law, brother-in-law and sisters-in-law. Family members' support encourages me to walk in this long journey.

Thank you, Lord, for Manhattan Chinese Christian Fellowship, a spiritual family where I can always find support, encouragement and renew my spiritual strength. The brothers and sisters' prayers encourage me to go through the difficulties in my research and daily life.

I also would like to thank all the friends surrounded me at Manhattan, Dr. Jianmei Zhang and Mr. Ping Hu, Dr. Zhifeng Cheng and Ms. Xiujuan Feng, Dr. Wangping Sun and Ms. Lian Li, Dr. Zhichao Li, Mr. Xinwei Shen and Ms. Qi Lu, Mr. Yu Chen, and many other friends for their friendship, love and care!

Last and most important, Lord, I thank you for all the above blessings! May your name be glorified forever!

CHAPTER 1 - Introduction

1.1 Motivation

Advanced ceramics have been increasingly used in automotive engine, aerospace, defense, medical, chemical & petrochemical, oil and gas, industrial wear and many other applications due to their high strength at elevated temperature, low density, thermal and chemical stability, and good wear resistance (Allor and Jahanmir, 1996; Allen, 1995; Jones, 1999). It was estimated that the total value of the U.S. advanced ceramic components market was $6.8 billion at 1997 and this would have increased to approximately $10 billion by 2002, with a growth rate of 7.9% from 1997 to 2002. However, this market was far below the predicted sales of advanced ceramics. In fact, the total value of the US advanced ceramics industry in 2006 was $8.6 billion and it was predicted to grow seven percent annually through 2010 (Freedonia market report, 2006). The predicted potential wider applications of advanced ceramics have been restrained largely because of the difficulty and high cost associated with shaping such extremely hard and brittle materials into products. Tressler and Howarth (2001) attributed the high cost of advanced ceramic components to expensive raw material, expensive machining, high inspection cost, and low yield. Recently, a new technology has been developed that can reduce the cost of the raw material by as much as 90-95%. Thus, the high machining cost has become the major bottleneck that is limiting the widespread use of advanced ceramic components. Studies have shown that the machining costs of advanced ceramics can account for 30 to 60%, and sometimes as much as 90%, of the total part cost (Pei et al., 1995; König and Wagemann, 1993). Therefore, the need to reduce machining cost becomes more urgent in order to reduce the overall fabrication cost for advanced ceramic components.

Machining is required for approximately 95% of the advanced ceramic components made today. Due to the high hardness and brittleness of ceramic materials, diamond grinding is the most commonly used industrial ceramic machining process, which accounts for approximately 80% of all machining performed on ceramics (Allor and Jahanmir, 1996). However, diamond grinding is a costly process due to its low material removal rate (MRR), high wear rates of diamond wheels, long wheel dressing times and serious surface/subsurface damage that needs expensive next processes like lapping to repair. Although improved grinding techniques have

been investigated trying to either minimize machining damage or maximize MRR, it has been found to be extremely difficult to achieve both (Bandyopadhyay and Ohmori, 1999; Westkämper, 1995; Marinescu, 1998). Various nontraditional machining procedures have been used in fabricating advanced ceramic parts, including ultrasonic machining, electrical-discharge machining, laser machining (LM), ductile regime machining and abrasive water-jet cutting. These techniques can either reduce the machining damage or increase the material removal rate. But these two aspects still seem to be largely exclusive of each other due to the features of advanced ceramics. Hence, there has always been an urgent demand in the industries for a cost effective, reliable and flexible machining technology for advanced ceramics.

Laser assisted machining (LAM) of advanced ceramics offers a potential method to increase the material removal rate and decrease the machining damage at the same time. LAM uses a laser to raise the cutting zone temperature of the workpiece before removing the material with a conventional tool. The elevated temperature lowers the yield strength of the ceramic material below its fracture strength so that the cutting zone material can demonstrate plastic deformation under machining. Studies in laser assisted turning of various advanced ceramics have shown that laser assistance offers important advantages over traditional machining, such as reduced power per volume of machined part, higher material removal rate, decreased cutting force, reduced chatter, smaller residual stresses, reduction of tool wear, avoidance of tool breakage, and crack-free machined surface (König and Zaboklicki, 1993; Rozzi, 1997; Rozzi et al. 1997, 2000a b c; Lei et al., 2001; Rebro et al., 2002; Pfefferkorn et al. 2004; Tian and Shin, 2006; Tian et al., 2006).

Although LAM of advanced ceramics has shown to be a very promising method to decrease the cost, improve the efficiency and reduce the surface/subsurface defects, to turn it from a laboratory art to a hardened production process, there are still many technical challenges to overcome. The micro-mechanism of material removal in LAM is still not fully understood. Currently, the LAM process design in laboratory is basically a trial and error process, assisted by usually stand-alone thermal models. No integrated design and optimization for LAM exists. Laboratory LAM process design requires extensive knowledge and experience to choose the operating parameters. In industry applications, however, it must be easy to choose machining and laser parameters for different parts and machining conditions, and the process design should not mainly depend on individual's experience. In order to move LAM technology into industrial

applications, there is a compelling demand to establish a methodology for LAM process design. In addition, very few studies have been done on laser assisted milling (LAMill) of ceramics. LAMill represents an even bigger challenge than laser assisted turning, because milling is an intermittent cut that involves frequent impact between the cutter and the workpiece. In order to turn laser assisted machining of advanced ceramics to a viable industrial technology, a comprehensive study on laser assisted milling is very much necessary. This study conducts a comprehensive experimental investigation of laser assisted milling of silicon nitride ceramics. Extensive experiments are conducted to study the cutting forces, tool wear, surface integrity, workpiece edge chipping and material removal mechanisms in laser assisted milling of silicon nitride ceramics. The mechanisms of workpiece edge chipping are investigated theoretically and experimentally and methods to minimize the workpiece edge chipping are studied. This study also applies distinct element method (DEM) to simulate the micro-mechanical behavior of LAMill of silicon nitride ceramics. The micro-mechanisms of material removal of LAMill of silicon nitride ceramics will be investigated. The DEM simulation lays a foundation for LAM process design and optimization.

1.2 Background

1.2.1 Silicon Nitride Ceramics

Industry has a critical need for materials that are light, strong, corrosion-resistant, and capable of performing in high-temperature environments. Although many ceramics perform well at considerably higher temperatures than conventional metal alloys, they are generally brittle and, as a result, can undergo catastrophic failure in service. Advanced ceramics are being developed to overcome this limitation. This new class of ceramic materials will have the high-temperature stability, corrosion resistance, and toughness necessary for a wide range of applications. One of the most significant advances in advanced ceramics has been to increase fracture toughness. Increased fracture toughness is important to industry because it reduces risk of fracture during service. Advanced ceramics can also provide substantial energy, environmental, and economical benefits, including lower maintenance, higher efficiency, and decreased operating costs (Freitag and Richerson, 1998). These traits enable many advanced ceramics to outperform other materials in numerous applications.

In the family of advanced ceramics, silicon nitride combines high strength and high toughness as a ceramic. Silicon nitride refers to an alloy family of ceramics whose primary constituent is Si_3N_4. The ceramics in this family have a favorable combination of properties that includes high strength over a broad temperature range, high hardness, moderate thermal conductivity, low coefficient of thermal expansion, moderately high elastic modulus, and unusually high fracture toughness for a ceramic. This combination of properties leads to excellent thermal shock resistance, ability to withstand high structural loads to high temperature, and superior wear resistance (Freitag and Richerson, 1998).

Si_3N_4 has been continuously under development in the U.S. since the late 1960s and the efforts have resulted in improved properties, increased reliability, complex shape fabrication capability, and some cost reduction (Freitag and Richerson, 1998). Si_3N_4 has been successfully demonstrated in a variety of applications. The first major application was cutting tool inserts. A more recent application for Si_3N_4 that is having revolutionary impact on many industries is bearings. Si_3N_4 balls similar to bearings are also in production for ball-and-seat check valves. In addition, Si_3N_4 is being vigorously evaluated for diesel and auto engine valves, valve guides, stator vanes and rotors for turbines, a variety of wear parts, tooling for aluminum processing, and many other potential products. The key message from the above examples is that the Si_3N_4 family is a new generation of ceramics that are much more durable and resistant to brittle fracture than traditional ceramics. As additional production applications are achieved and current production levels increase, it is anticipated that the cost of blank silicon nitride material will come down substantially. The machining cost would become the primary barrier limiting the potential broad use of advanced silicon nitride materials.

Since Si_3N_4 ceramic is one of the typical advanced ceramics with the most promising potential applications, this study uses Si_3N_4 ceramic as an example to investigate laser assisted milling on advanced ceramics.

1.2.2 Various Machining Methods for Advanced Ceramics

Currently, a broad range of manufacturing processes have been used to fabricate advanced ceramic products. Although forming processes can produce various shapes at a high production rate, a subsequent finishing process is often needed to achieve a high dimensional accuracy and/or a very fine surface finish. Turning, a very effective process in metal cutting,

encounters difficulties in machining ceramics. It was shown that, although machinable with a diamond or polycrystalline cubic boron nitride (PCBN) cutting tool, rough surfaces were formed due to irregular cracking of the material with surface/subsurface cracks (Zhang et al., 1994 and 2000). In addition, Due to the high hardness of ceramic materials, material removal rate is very low and tool wear is fast.

Diamond grinding is the most commonly used method to machine precision ceramic parts in industry. However, diamond grinding is a costly process due to its low material removal rate (MRR), high rates of wear of diamond wheels and long wheel dressing times (Bandyopadhyay and Ohmori, 1997). According to Konig and Wagemann (1993) and Chryssolouris et al. (1997), machining cost often constitutes 60-90% of the total cost of many ceramic parts. Another critical problem is that grinding causes surface/subsurface cracks which are often on the order of 50-100 mm under normal grinding conditions and thus cause material strength degradation (Mayer, 1999). Mochida et al. (1991) reported a 10-20 % reduction in the strength of high-speed ground ceramics. Although various grinding techniques have been investigated trying to either minimize machining damage or maximize MRR, it has been found to be extremely difficult to achieve both (Tuersley et al., 1994; Bandyopadhyay and Ohmori, 999;Westkämper, 1995; Marinescu, 1998). One proposed method is the so-called “ductile-regime” grinding. This method maintains a constant volume of material removal per grit and minimize the grinding forces to avoid the generation of cracks. The particular high ratio of normal to tangential forces leads to elastic deformation of structural parts of the machine such as the wheel and spindle. Thus, the machining efficiency lowers and the finishing accuracy decreases. It is necessary to use a “stiff” machine to compensate. The set-up of the wheel must be particularly precise and could be maintained at an exact setting during the machining process. Although ductile-regime grinding as a method reduces machining damage, it is time consuming. An alternative method is “creep-feed” grinding that offers greater material removal rate. Creep-feed grinding involves reduced power intensities and much lower stress levels in the grinding zone than in surface grinding. This method engages the wheel in the workpiece to the full depth of grind and advances the table at particularly low speeds. This demands consistent truing and dressing of the wheel and needs for precise table travel rates without vibration or slippage, as well as proper coolant application and flow rate. Bond-type and grit size aspects of the wheel have a significant effect. It was claimed that grinding time was reduced by 10% and tool wear was decreased considerably.

Various non-traditional machining procedures have been used in fabricating ceramic parts, including ultrasonic machining, electrical-discharge machining (EDM), and laser machining (LM). Ultrasonic machining is suitable for manufacturing components with complex shapes in small quantities (Gilmore, 1989; Pei et al., 1995). By using small abrasive particles, good surface finish can be obtained without subsurface damage or degradation of mechanical properties. In ultrasonic machining of ceramics, the material is removed primarily by repeated impact of the abrasive particles. Several studies have been shown that impact of brittle materials by hard and sharp particles are generally thought to result from elastic/plastic fracture. This type of fracture is characterized firstly by plastic deformation of the contact area between the impacting particle and the ceramic surface, with subsurface lateral cracks propagating outward from the base of the contact zone on the planes nearly parallel to the surface, and with median cracks propagating from the contact zone normal to the surface. The material removal is thought to occur primary by surface chipping when lateral cracks curve up and intersect the surface. While the median cracks remain in the surface and influence subsequent strength. Li et al. (2005) introduced rotary ultrasonic machining (RUM) into drilling holes on CMC panels and a typical advanced ceramic (alumina). Compared with diamond drilling process, RUM could reduce cutting force significantly (about 50%) and improve MRR (about 10%). With proper machining parameters, RUM experiments achieved high-quality holes on CMC panels. Deng and Lee (2002) investigated the effect of the properties and microstructure of the workpiece materials on the MRR in ultrasonic machining of alumina-based ceramic composites. Results showed that fracture toughness of the ceramic composite played an important role with respect to MRR. In USM of whisker-reinforced alumina composites, the MRR depended on the whisker orientation. Studies of strength distribution of alumina-based ceramic composites machined by USM demonstrated that the flexural strength varied narrowly from the mean value, and the composites with high fracture toughness showed higher Weibull modulus. However, its application is limited by the cost and wear of the sonotrodes, as well as low material removal rates for deeper cuts (Hahn et al., 1993; Chand and Guo, 1996).

Electrical discharge machining is a non-abrasive process which applies little mechanical stress to the workpiece and can machine complex parts with good surface finish, regardless of material hardness. However, its main disadvantage is the requirement that the electrical

resistivity of the material be less than approximately 100 Ω·cm for successful machining (Petrofes and Gadalla, 1988).

Laser machining (LM) is a non-contact process, which utilizes intense, localized heating to melt and/or vaporize materials, thus eliminating cutting tool and workpiece interaction, tool wear, chatter, and machine tool deflection (Islam and Campbell, 1993). Laser-based shaping operations may significantly reduce the cost of ceramic machining. Carrol et al. (2000) studied the heat affected zones in silicon carbide/silicon carbide ceramic composites. They also investigated the feasibility of using a carbon dioxide laser system to finish green ceramic composites. Comparison of the as-received, diamond saw cut, and laser machined SiC/SiC surfaces gave similar roughness trends. However, the disadvantages of LM are thermal damage and cracking, alterations of the surface microstructure, relatively poor surface finish caused by intense localized heating, and decreased material strength (Chryssolouris et al., 1997; Burck and Wiegel, 1995).

Despite the existence of various machining methods for ceramics, high costs and subsurface damage still impede the use of ceramic products. Especially, with the emergence of the new technology which promises significant savings for the blank material of Si_3N_4 and Al_2O_3 ceramics, machining cost is most likely to become the bottleneck in the battle for cost reduction of machined components. Therefore, There is a compelling need for new methods of machining ceramics that will decrease the cost and improve the efficiency without compromising part quality.

1.2.3 Laser Assisted Machining of Advanced Ceramics

Laser assisted machining (LAM) is a very promising technique to achieve high MRR without inducing additional surface damages. Since heating is used to increase the ductility and decrease the strength of ceramic materials in LAM, subsequent fast material removal with a cutting tool can be realized through more plastic deformation and less brittle cracking.

LAM uses a laser beam to heat the material before it is removed by a conventional single point cutting tool. Compared to LM, using a cutting tool to remove the material could eliminate the thermal damaged layer and produce desired surface finish and dimension tolerance. Bass et al. (1978) and Copley (1983) attempted to use LAM for hard metals such as stainless steels, nickel-based superalloys and titanium alloys. By focusing the laser beam on the shear plane

during chip formation, cutting force was significantly reduced while the material removal rate was greatly increased. However, Copley (1983) pointed out that the benefits of LAM must be economically justified by comparing its benefits against the added cost associated with the use of a laser. He also pointed out that further studies of tool wear and surface integrity is necessary to technologically justify LAM.

In the past decade, with the rapid development of laser systems and fiber optic beam delivery technologies, laser assisted machining (LAM) has been shown to be a very promising method to decrease the cost, improve the efficiency and reduce the surface/subsurface defects (Lei et al., 2001; Skvarenina and Shin, 2006; Rebro et al., 2004; König and Zaboklicki, 1993). LAM offers important advantages over traditional machining such as reduced power per volume of machined part, higher material removal rate, decreased cutting force, reduced chatter, small residual stresses, reduction of tool wear, avoidance of tool breakage, crack-free machined surface. König and Zaboklicki (1993) obtained continuous chips for hot pressed silicon nitride when workpiece temperature at the cutting zone exceeded 1200°C, a large material removal rate and a surface finish with less than 0.5 μm, which is equivalent to that of ground surfaces. The cutting force and tool wear were reduced up to 70% and 90% respectively. Lei et al. (2001) studied the material removal mechanisms, tool wear, and surface integrity in laser assisted turning of Si_3N_4. It was demonstrated that the tool life in LAM of silicon nitride was projected to be 19 and 42 minutes for cutting zone temperature of 1260 °C and 1410 °C respectively. Tool wear was mainly on the flank face with negligible crater wear on the rake face. Adhesion was the dominant mode of tool wear. The thickness of the affected layer of the workpiece for LAM ranged from 2 to 4 mm, which was significantly smaller than that in grinding. No surface and subsurface cracks on machined surface were observed in LAM and there was less degradation of material strength. Wang et al. (2002) showed that the cutting force in LAM of particle reinforced aluminum matrix composite, compared with conventional cutting, was reduced by 30-50% and the tool wear was reduced by 20-30% and the machined surface quality was improved. Tian and Shin (2006) extended their work into complex geometric silicon nitride parts. The authors developed a three-dimensional, transient thermal model to predict the temperature distribution and to achieve optimal operating conditions for LAM. In order to achieve good machining results and avoid thermal damage, the material removal temperature was carefully controlled by in-process control of laser power. The experiments obtained very impressive results of long tool

life, good surface finish, thermal damage-free surface, excellent subsurface integrity and moderate compressive residual stress.

The significance of determining temperatures in the workpiece is clear for successful LAM, since the benefits of LAM can be achieved and optimized only when the workpiece is heated properly. Although analytical solution continues to be attempted for the highly transient and three-dimensional temperature field in LAM (Gutierrez and Araya, 2004), the complexity of the problem usually demands the use of numerical means for a detailed understanding. A transient, three-dimensional thermal model was first developed by Rozzi et al. (1997, 1998a,b) for a rotating cylindrical workpiece subjected to a translating laser heat source, and later this model was extended to the workpiece undergoing laser-assisted turning with material removal (Rozzi et al., 2000b,c). Solved by a numerical scheme based on the finite volume method (FVM), this model provided the temperature field in an opaque, homogeneous (silicon nitride) workpiece during LAM. With the numerical solution approach, this model was able to account for the incident laser flux distribution, conduction within the workpiece, convection and radiation on all surfaces, heat loss resulting from material removal, temperature dependent thermo-physical properties of the workpiece, and heat generation at the machining zone due to the machining process. Empirical formulation and experimental data were used to determine the thermal effects of machining, i.e., heat generations due to the workpiece plastic deformation and the friction between the workpiece and the tool flank, respectively. Numerical simulations showed that such heat generation from machining had a smaller effect on the transient temperature field during LAM compared with the laser heating, while the laser power and feed rate were the most significant parameters affecting the temperature field and material removal temperature.

Surface temperature predictions given by the model were compared with transient surface temperature measurements by a laser pyrometer (Rozzi et al., 2000a; Pfefferkorn et al., 1997). The laser pyrometer measured the surface temperature and emissivity of the workpiece concurrently at the wavelength of 0.865 μm, at which silicon nitride is opaque. In general, it was shown that the temperature histories predicted by the thermal model agreed reasonably with the experimental measurements under all operating conditions.

Later on, Pfefferkorn et al. (2005) extended the model to semitransparent, homogeneous material undergoing LAM. Two approaches, the discrete-ordinates method and the diffusion

approximation, were used to account for the internal radiation inside the semitransparent workpiece. The predicted temperatures by the two approaches were shown to be close to each other and validated by temperature measurements with a long-wavelength pyrometer (Pfefferkorn et al., 2003, 2005). The diffusion approximation, which uses effective thermal conductivity to account for internal radiative transfer under the optically thick assumption, was chosen for further investigations (Pfefferkorn et al., 2004), because it costed less computer time and compared more favorably with the measurements.

Tian and Shin (2006) reformulated the standard enthalpy-based heat transfer model into a transient three-dimensional temperature-based iterative method to simulate the temperature distributions of the workpiece undergoing laser-assisted machining. By adopting the technique of partial activation and deactivation of control volumes, the new modeling technique provided the simulation of LAM with material removal during profiling of a part with complex part geometry, similar to the actual process. Tian et al. (2006) also presented a transient, three-dimensional prismatic thermal model applicable to laser assisted milling and showed good agreement with surface temperature measurements by an infrared camera.

Previous work has shown that LAM has many advantages over other machining techniques, such as reduced cost, less subsurface cracks, high material removal, however, the foregoing research in LAM of ceramics is still not far from the concept-proving stage. There is a significant amount of innovative work that remains to be done to realize the potential of LAM to become an alternative machining process to grinding, which does not create subsurface cracks in the machined parts, has the flexibility for cost-effective machining of complex parts, and is insensitive to part quantity and geometry.

1.2.4 Micro-Mechanical Modeling of LAM of Advanced Ceramics

Although extensive experimental studies have been conducted to understand the material removal mechanisms in machining of ceramics, there are still many questions regarding the micro-mechanisms of material removal based on the available experimental observations. Different hypotheses are developed to explain the material removal mechanisms in machining ceramics. Komanduri (1996) discussed the hypothesis of “ductile” grinding of ceramics over the hypothesis of “gentle” grinding. According to “ductile” grinding hypothesis, all materials, regardless of their hardness and brittleness, will undergo a transition from brittle to ductile

machining when the depth of cut is smaller than a critical depth of cut. It is assumed that the energy required for plastic deformation is smaller than the energy required to propagate the cracks. Plastic deformation is the predominant material removal mechanism in "ductile" grinding of ceramics. However, there is little plastic deformation in "gentle" grinding hypothesis. According to this hypothesis, the mode of deformation (plastic or brittle) depends on the state of stress, not on the magnitude of the stress. It is hard to explain why the mode of deformation will change merely by decreasing the depth of cut. The superior surface obtained at small depth of cut is due to the light load but not necessary due to plastic deformation. Microcracks are formed but may not propagate to form larger cracks under small loads. This example shows that it is hard to accurately understand the micromechanisms of machining ceramics merely from experimental observations. There is a need to develop a micro-mechanical model of the material removal process for machining ceramics.

Numerical simulation is an alternative way to investigate the micromechanisms of machining ceramics. It has been shown that the material removal in conventional machining of ceramics is dominated by brittle fractures, and the mechanical behavior of ceramics is controlled by the propagation of small cracks, including median cracks, lateral cracks and radial cracks. In order to simulate the material removal mechanisms of ceramic machining, how to treat large amount of crack formation and propagation is therefore very important and always a challenge. Finite element method (FEM) has been used to study chip formation and surface damage in machining of ceramics (Ueda et al. 1991; Zhang et al., 2000; Cao, 2001; Chiu et al. 2001; Kumbera at al. 2001). But FEM faces difficulty in dealing with a large number of cracks and treating interactions among broken elements when they come into contact again.

Distinct element method (DEM) provides an alternative way by treating materials as arbitrarily sized particles bonded together. When the bonds break, cracks are formed or extended. DEM has proven to be a promising method to simulate rock cutting. Huang (1999) applied DEM to rock cutting and demonstrated that DEM could reproduce the experimental observation of a failure mode transition from brittle to ductile failure depending on a critical depth of cut. Lei and Kaitkay (2002) and Kaitkay (2002) used DEM to model rock cutting and demonstrated that the cutting forces in the simulation agrees well with the experimental results. Tannant and Wang (2002, 2004) applied DEM to thin liners of underground rock support to simulate the liner support mechanisms. Potyondy and Cundall (2004) demonstrated that DEM simulation could

reproduce most of the mechanical properties of Lac du Bonnet granite. Extensive studies have shown that DEM is capable to simulate the mechanical behavior of brittle materials.

In order to model the initiation and propagation of a large number of microcracks, this study will try to apply DEM simulation in laser assisted machining of silicon nitride ceramics. Bonded circular particles are used to model the ceramic workpiece. Particles are clustered to model the rod-shaped microstructure of silicon nitride. Bond breakage during simulation represents crack formation and propagation. This is the first effort to apply DEM to model the micro-mechanical behavior of LAM of advanced ceramics.

1.3 Objectives and Scope of this Research

This study experimentally and numerically investigates laser assisted milling (LAMill) of silicon nitride ceramics. Extensive experiments are conducted to investigate the effects of the elevated temperature on cutting forces, chip formation, tool wear, surface integrity and workpiece edge chipping. In order to better control the serious workpiece edge chipping in LAMill, the mechanisms of elevated temperature on the material behavior of silicon nitride ceramics are investigated. Numerical simulation of distinct element method (DEM) is used to investigate the micro-mechanical behavior of silicon nitride ceramics. The micro-mechanism of material removal is modeled by DEM simulation which lays a foundation for LAM process design and optimization.

The objectives of this research are summarized as the following:

(1) Study the machinability of silicon nitride ceramics under laser assisted milling.

(2) Investigate the mechanisms of elevated temperature on the material behavior of silicon nitride ceramics.

(3) Investigate the material removal mechanisms in LAMill of silicon nitride ceramics.

(4) Develop a micro-mechanical model to simulate the material removal in LAM of advanced ceramics by applying distinct element method (DEM) to modeling LAM of silicon nitride ceramics.

This thesis follows the alternate format accepted by Industrial and Manufacturing Systems Engineering Department, which is organized as a collection of four papers, each of which is complete in itself. Chapter 1 is an introduction of the background, motivation and the

objectives of this work. Chapter 2 is experimental investigation of LAMill of silicon nitride ceramics, which includes two technical papers. Section 2.1 is a paper about the machinability study of LAMill of silicon nitride ceramics. Section 2.2 investigates the mechanisms of edge chipping at elevated temperature in LAMill of silicon nitride ceramics. Chapter 3 uses distinct element method (DEM) to simulate the micro-mechanical behavior of machining silicon nitride ceramics, which also includes two papers. Section 3.1 investigates the relationships between microparameters at particle level and macroproperties of the specimens that are modeled by bonded particles. This study provides guidelines to generate a specimen. Section 3.2 applies DEM to simulate the material removal process in conventional and LAM of silicon nitride ceramics. Chapter 4 presents the overall conclusions from this work and further research development in this field.

1.4 References

Allor, R. L., Jahanmir, S., 1996, “Current problems and future directions for ceramic machining”, American Ceramic Society Bulletin, v 75, n 7, P40-43.

Allen, T., 1995, “Engineering ceramics”, Engineering (London), v 236, n 4, p 2.

Bandyopadhyay, B.P.; Ohmori, H., 1999, “Effect of ELID grinding on the flexural strength of silicon nitride”, International Journal of Machine Tools & Manufacture, v 39, n 5, p 839-853.

Bass, M., Beck, D., and Copley, S. M., 1978, "Laser Assisted Machining," Fourth European Electro-Optics Conference, Utrecht, Netherlands, pp. 233-240.

Burck, P.; Wiegel, K., 1995, “Laser machining of Si_3N_4 ceramics”, Optical and Quantum Electronics, v 27, n 12, p1349-1358.

Cao, Y., 2001, “Failure analysis of exit edges in ceramic machining using finite element analysis,” Engineering Failure Analysis, Vol.8, p.325-338.

Carroll, J.W.; Todd, J.A.; Ellingson, W.A.; Polzin, B.J., 2000, “Laser machining of ceramic matrix composites”, Ceramic Engineering and Science Proceedings, v 21, n 3,p 323-330.

Chand, R.; Guo, C. S., 1996, “New concept in cost-effective machining”, American Ceramic Society Bulletin, v 75, n 7, p 58-59.

Chiu, W.-C, Endres, W.J., and Thouless, M.D., 2001, “An analysis of surface cracking during orthogonal machining of glass,” Machining Science and Technology, Vol.5, No.2, p.95-215.

Chryssolouris, G.; Anifantis, N.; Karagiannis, S., 1997, “Laser assisted machining: An overview”, Journal of Manufacturing Science and Engineering, Transactions of the ASME, v 119, n 4(B), Nov, 1997, p766-769.

Copley, S. M., 1983, "Laser Shaping of Materials," Lasers in Materials Processing, Proceedings of ASM conference, Los Angles, CA, Vol. 8301, pp. 82-86.

Deng, J. and Lee, T., 2002, “Ultrasonic machining of alumina-based ceramic composites”, Journal of the European Ceramic Society, v. 22, pp.1235-1211.

Freedonia market report, 2006, Advanced Ceramics to 2010 - Demand and Sales Forecasts, Market Share, Market Size, Market Leaders.

Freitag, D. W. and Richerson, D. W., 1998, “Opportunities for Advanced Ceramics to Meet the Needs of the Industries of the Future”, US Advanced Ceramics Association and Oka Ridge National Labotary.

Gilmore, R., 1989, “Ultrasonic machining”, SME Technical Paper (Series) EM, var paging EM89-123.

Gutierrez, G., and Araya, J. G., 2004, "Analytical Solution for a Transient Three-Dimensional Temperature Distribution in Laser Assisted Machining Processes," Proceedings of the ASME Heat Transfer/Fluids Engineering Summer Conference 2004, HT/FED 2004, Vol. 3, pp. 1055-1063.

Hahn, R.; Lost, C.; Schulze, P., 1993, “Ultrasonic shaping: an economical procedure to machine complex ceramic components”, NIST Special Publication, n 847, p 385-389.

Huang, H. Y., (1999), Discrete element modelling of tool-rock interaction, Ph.D. Thesis, University of Minnesota, Minneapolis, Minnesota, USA.

Islam, M.U., Campbell, G., 1993, “Laser machining of ceramics: a review”, Materials and Manufacturing Processes, v 8, n 6, p 611-630.

Jones, A.C., 1999, “Design, analysis and testing of ceramic components for an advanced military expendable turbojet engine”, Ceramic Engineering and Science Proceedings, v 20, n 4, p 523-532.

Kaitkay, P., 2002, Modelling of rock cutting using distinct element method, Master Thesis, Kansas State University, Manhattan, Kansas, USA.

Komanduri R., 1996, "On material removal mechanisms in finishing of advanced ceramics and glasses", Annals of the CIRP, Vol. 45, No. 1, p.509-513.

Konig, W.; Wagemann, A., 1993, "Machining of ceramic components: process-technological potentials", NIST Special Publication, n 847, p 3-16.

König, W., and Zaboklicki, U., 1993, "Laser –Assisted Hot Machining of Ceramics and Composite Materials", Machining of Advanced Materials, NIST Special Publication 847, pp. 455-463.

Kumbera T. G., Cherukuri H. P., Patten J. A., Brand C. J., and Marusich T. D., (2001), "Numerical simulations of ductile machining of silicon nitride with a cutting tool of defined geometry," Machining Science and Technology, Vol.5 No.3, p.341-352.

Lei, S., and Kaitkay, P., 2002, "Micromechanical modelling of rock cutting under pressure boundary conditions using distinct element methods," Transactions of the North American Manufacturing Research Institution of SME, Vol. 30, p.207-214.

Lei, S., Shin, Y.C., Incropera, F.P., 2001, "Experimental Investigation of Thermal-Mechanical Characteristics in Laser-Assisted Machining of Silicon Nitride Ceramics", Journal of Manufacturing Science and Engineering, v 123, p 639-646.

Li, Z.C., Jiao, Y., Deines, T.W., Pei, Z.J. and Treadwell, C., 2005, "Rotary ultrasonic machining of ceramic matrix composites: Feasibility study and designed experiments", International Journal of Machine Tools and Manufacture, v 45, n 12-13, p 1402-1411.

Marinescu, I.D., 1998, Laser Assisted Grinding of Ceramics, InterCeram, v 47, n 5, p 314-316.

Mayer, J. E. Jr., 1999, "Grinding of ceramics with attention to strength and depth of grinding damage", Technical Paper - Society of Manufacturing Engineers. MR, n MR99-237, p.1-15.

Mochida, M., Suzuki, H.; Shimamune, T., 1991, "Effects of grinding conditions on the ground surface aspects of fine ceramics (1st report): Forming mechanism of ground surface in case of SiC, Si3N4 and Al2O3", Journal of the Japan Society of Precision Engineering/Seimitsu Kogaku Kaishi, v 57, n 2, p 304-309.

Pei, Z.J.; Khanna, N.; Ferreira, P.M., 1995, “Rotary ultrasonic machining of structural ceramics - a review”, Ceramic Engineering and Science Proceedings, v 16, n 1, p 259-278.

Petrofes, N. F.; Gadalla, A. M., 1988, “Electrical Discharge Machining of Advanced Ceramics”, American Ceramic Society Bulletin, v 67, n 6, p1048-1052.

Pfefferkorn, F. E., Incropera, F. P., and Shin, Y. C., 2005, "Heat Transfer Model of Semi-Transparent Ceramics Undergoing Laser-Assisted Machining," International Journal of Heat and Mass Transfer, 48, pp. 1999-2012.

Pfefferkorn, F. E., Incropera, F. P., and Shin, Y. C., 2003, "Surface Temperature Measurement of Semi-Transparent Ceramics by Long-Wavelength Pyrometry," ASME Journal of Heat Transfer, 125(1), pp. 48-56.

Pfefferkorn, F. E., Rozzi, J. C., Incropera, F. P., and Shin, Y. C., 1997, "Surface Temperature Measurement in Laser-Assisted Machining Processes," Experimental Heat Transfer, 10(4), pp. 291-313.

Pfefferkorn, F.E., Shin, Y.C., Incropera, F.P. and Tian, Y., 2004, "Laser-Assisted Machining of Magnesia-Partially-Stabilized Zirconia," ASME Journal of Manufacturing Science and Engineering, v 126, n 1, p 42-51.

Potyondy, D. O., and Cundall, P. A., 2004, “A bonded-particle model for rock,” International Journal of Rock Mechanics and Mining Sciences, Vol.41, p.1329-1364.

Rebro, P. A., Shin, Y. C., and Incropera, F. P., 2002, "Laser-Assisted Machining of Reaction Sintered Mullite Ceramics," ASME Journal of Manufacturing Sciences and Engineering, 124(4), pp. 875-885.

Rebro P. A. , Shin Y.C., Incropera, F.P., 2004, “Design of Operating Conditions for Crackfree Laser-assisted Machining of Mullite”, International Journal of Machine Tools and Manufacture, v. 44, p 677-694.

Rozzi, J. C., 1997, "Experimental and Theoretical Evaluation of the Laser Assisted Machining of Ceramic Materials," Ph.D. thesis, Purdue University, West Lafayette, IN.

Rozzi, J. C., Incropera, F. P., and Shin, Y. C., 1997, "Transient, Three-Dimensional Heat Transfer Model for the Laser Assisted Machining of Ceramic Materials," 1997 ASME International Mechanical Engineering Conference and Exposition, Dallas, TX, HTD, Vol. 351, pp. 75-85.

Rozzi, J. C., Pfefferkorn, F. E., Incropera, F. P., and Shin, Y. C., 1998a, "Transient Thermal Response of a Rotating Cylindrical Silicon Nitride Workpiece Subjected to a Translating Laser Heat Source: I-Comparison of Surface Temperature Measurements with Theoretical Results," ASME Journal of Heat Transfer, 120(4), pp. 899-906.

Rozzi, J. C., Incropera, F. P., and Shin, Y. C., 1998b, "Transient Thermal Response of a Rotating Cylindrical Silicon Nitride Workpiece Subjected to a Translating Laser Heat Source: II-Parametric Effects and Assessment of a Simplified Model," ASME Journal of Heat Transfer, 120(4), pp. 907-915.

Rozzi, J. C., Pfefferkorn, F. E., Shin, Y. C., and Incropera, F. P., 2000a, "Experimental Evaluation of the Laser Assisted Machining of Silicon Nitride Ceramics," ASME Journal of Manufacturing Science and Engineering, 122(4), pp. 666-670.

Rozzi, J. C., Pfefferkorn, F. E., Incropera, F. P., and Shin, Y. C., 2000b, "Transient, Three-Dimensional Heat Transfer Model for the Laser Assisted Machining of Silicon Nitride: I-Comparison of Predictions with Measured Surface Temperature Histories," International Journal of Heat and Mass Transfer, 43, pp. 1409-1424.

Rozzi, J. C., Incropera, F. P., and Shin, Y. C., 2000c, "Transient, Three-Dimensional Heat Transfer Model for the Laser Assisted Machining of Silicon Nitride: II-Assessment of Parametric Effects," International Journal of Heat and Mass Transfer, 43, pp. 1425-1437.

Skvarenina, S., Shin, Y.C., 2006, “Laser-assisted Machining of Compacted Graphite Iron”, International Journal of Machine Tools and Manufacture, Vol. 46, P7-17.

Tannant, D. D. and Wang, C. G., 2002, “Thin rock support liners modeled with particle flow code”, Geotechnical Special Publication, n 117, p.346-352.

Tannant, D. D. and Wang, C. G., 2004, “Thin tunnel liners modelled with particle flow code”, Engineering Computations, v 21, n 2, 2004, p 318-42.

Tian, Y., Wu, B., and Shin, Y. C., 2006, "Laser-Assisted Milling of Silicon Nitride Ceramics," *Proceedings of the 2006 ASME International Conference on Manufacturing Science and Engineering*, 7p.

Tian, Y. and Shin, Y.C., 2006, “Laser-assisted Machining of Silicon Nitride with Complex Geometric Features via In-process Control”, Journal of the American Ceramic Society, v.89, n. 11, p 3397-3405.

Tressler, J.F.; Howarth, T. R., 2001, "Failure analysis of prototype cymbal panels under high drive conditions", Ceramic Engineering and Science Proceedings, v 22, n 4, p 531-542.

Tuersley, I.P., Jawaid, A. and Pashby, I.R., 1994, "Review: Various methods of machining advanced ceramic materials", Journal of Materials Processing Technology, v. 42, p. 377-390.

Ueda, K., Sugita, T., and Hiraga, H., 1991, "J-integral approach to material removal mechanisms in microcutting of ceramics," CIRP Annals, Manufacturing Technology, Vol.40, No.1, p.61-64.

Wang, Y., Yang, L.J. and Wang, N.J., 2002, "An Investigation of Laser-assisted Machining of Al_2O_3 Particle Reinforced Aluminum Matrix Composite", Journal of Materials Processing Technology, v 129, p. 268-272.

Westkämper, E., 1995, "Grinding Assisted by Nd: YAG Lasers", CIRP Annals - Manufacturing Technology, v 44, n 1, p 317-320.

Zhang, G.M., Cao, Y., and Rekow, D., 2000, "A computational approach to evaluate surface integrity of glass ceramics," Transactions of NAMRI/SME, Vol.28, p.279-284.

Zhang, B.; Howes, V.R.; Trevor, D., 1994, "Material-removal mechanisms in grinding ceramics", CIRP Annals, v 43, n 1, p305-308.

Zhang, Z.; Hung, N. P., 2000, "Diamond turning and grinding of aluminum-based metal matrix composites", Materials and Manufacturing Processes, v 15, n 6, p.853-865.

CHAPTER 2 - Experimental Investigation of Laser Assisted Milling of Silicon Nitride Ceramics

This chapter focuses on experimental investigation of laser assisted milling (LAMill) of silicon nitride ceramics. First, the machinability of LAMill of silicon nitride ceramics is studied. It is found that laser assistance significantly improves the machinability of silicon nitride ceramics. But workpiece edge chipping is a major macro-scale defect in LAMill of silicon nitride. Therefore, the mechanisms of workpiece edge chipping under laser assistance are investigated and the temperature range to minimize workpiece edge chipping is proposed. The results are presented in the following sections. Each section is organized as a technical paper.

2.1 Laser Assisted Milling of Silicon Nitride Ceramics: A Machinability Study

Published in:

International Journal of Mechatronics and Manufacturing Systems, Vol. 1, No. 1, 2008, pp.116-130.

Author's Names:

Budong Yang, Shuting Lei

Author's Affiliation:

Department of Industrial and Manufacturing Systems Engineering, Kansas State University, 212 Durland Hall, Manhattan, KS 66506

2.1.1 Abstract

The machinability of silicon nitride ceramic under laser assisted milling (LAMill) is presented in this section. Cutting force, surface roughness, tool wear, edge chipping and chip morphology were examined. The effect of workpiece temperature on cutting force was analyzed.

Chips were collected and observed under optical microscope to understand the material removal mechanism. Surface integrity was examined and compared with that of ground surface. Tool wear and workpiece edge chipping were measured under different temperatures. It was found that laser heating strongly affect all the above-mentioned quantities but surface roughness. Cutting force decreases and chip size increases with temperature. Brittle fracture of the PCBN cutting tool was avoided when temperature is higher than 1000 °C. And tool wear was significantly reduced as temperature increases. But tool wear is quite large in LAMill of silicon nitride ceramics. Surface roughness comparable to the as-received ground surface was obtained. Chipping at the (tool) exit edge is much more severe than at the entry edge. When combining high temperature and blunt exit angle, macroscale exit edge chipping can be completely eliminated in LAMill of silicon nitride ceramics.

Keywords: Laser-Assisted Milling; LAMill; Silicon Nitide Ceramics; Machinability.

2.1.2 Introduction

Since the early 1990s, laser assisted machining (LAM) of structural ceramics has attracted worldwide attention and significant amount of research has been done in an attempt to further understand the complex process and to show LAM's viability as an economical industrial machining process for ceramics. Experimentally, it has been shown that laser heating induces plastic behavior for ceramics through either softening of glass boundary phase (König and Zaboklicki, 1993; Lei et al., 2001) or high temperature dislocation motions (Pfefferkorn et al., 2004). Longer chips are produced with higher temperatures. Cutting force generally decreases with cutting zone temperature while the dependence of tool life on temperature is more complex. Singh and Melkote (2005) studied laser assisted mechanical machining process for micromachining applications. It was shown that thermal softening induced by laser heating could reduce the cutting force by up to 34%. Surface roughness from LAM is comparable with grinding (Rebro et al., 2002). Surface/subsurface damage is reduced in LAM compared to grinding, resulting in stronger machined parts (Klocke and Bergs, 1997). More recently, significant cost-reduction has been demonstrated for LAM of silicon nitride (Tian, 2006). Besides experimental investigations, rigorous numerical modeling has deepened our basic understanding of the workpiece temperature field in LAM for both opaque ceramics such as silicon nitride (Rozzi et al., 2000a; Rozzi et al., 2000b; Tian and Shin, 2006) and semitransparent

ceramics such as partially-stabilized zirconia (Pfefferkorn et al., 2005). The modeling and simulation of the coupled thermo-mechanical material removal process in LAM is also underway towards complete understanding of the fundamental mechanisms (Shen and Lei, 2005; Tian and Shin, 2007).

While significant progress has been made in research on laser assisted turning, as mentioned above, few studies have concerned laser assisted milling. The feasibility of laser assisted milling was first shown by König and Zaboklicki (1993) on a difficult-to-machine material, stellite 6. More recently, Shen et al. (2005) developed a finite element model to simulate the temperature and stress fields during LAMill of silicon nitride. Jeon and Pfefferkorn (2005) investigated laser assisted micro-end milling and demonstrated that laser assistance could increase chip load, reduce cutting force and specific cutting energy. Tian et al. (2006) recently developed a transient, three-dimensional thermal model for laser assisted milling and successfully conducted experiments on silicon nitride ceramics using TiAlN coated carbide end mills. Very good surface roughness and acceptable tool wear were obtained.

Laser assisted milling represents an even bigger challenge than laser assisted turning, because milling is an intermittent cut that involves frequent impact between the cutter and the workpiece, which is likely to cause tool fracture and serious workpiece edge chipping. This study attempts to make a more comprehensive assessment of laser assisted milling of silicon nitride ceramics. The main purpose is to evaluate the machinability of the material in terms of cutting force, surface roughness, tool wear, edge chipping and chip morphology. In the following sections, the experimental setup and conditions will be described first, then followed by results and discussions, and finally the conclusions will be summarized.

2.1.3 Experimental Conditions

2.1.3.1 Experimental System

The experimental system for laser assisted milling of silicon nitride ceramic is shown in Figure 2.1. The milling operation is carried out on a 15-HP CNC milling center. A 500-W diode laser system is used to generate a high power laser beam, which is delivered through the fiber optic and focused on the workpiece surface at an angle of about 60 deg. The laser focusing end is fixed on the spindle of the milling center and cooled by blowing air to prevent the optics from being overheated during milling. A laser pyrometer (Williamson pro series, model No. 23D) with

a range of 450-1750 °C is used to concurrently measure the temperature of the cutting zone. The pyrometer is also fixed on the spindle. During milling, the cutting tool rotates; the laser beam and the pyrometer do not move, while the workpiece translates with the worktable. Therefore, the relative positions of the laser spot, the cutting edge and the measurement spot remain the same during each milling pass, as shown by a schematic on the left in Figure 2.1.

The Si_3N_4 workpiece is a beam type sample with dimensions of 4.3 x 5.3 x 48 mm. It is sintered reaction bonded Si3N4 (~7% sintering agent), a fully dense material (>99.5% theoretical density) with the unique microstructure of interlocking needle shaped grains. The workpiece is clamped in a fixture, which is mounted on a Kistler three-component dynamometer (Type 9257B) for measuring the global x, y, and z direction forces. The electrical charges from the dynamometer are converted to voltage signals by a Kistler charge amplifier (Type 5010). The cutting force and temperature data are recorded on a computer automatically during each cut with a LabVIEW based system. A polycrystalline cubic boron nitride (PCBN) tipped insert is clamped in a self-made tool holder with a diameter of 76.2 mm. In order to minimize heat loss from the workpiece through the fixture, the workpiece is padded with two asbestos plates to decrease the temperature gradient by slowing down the heat loss.

Figure 2.1 Experimental System for Laser Assisted Milling

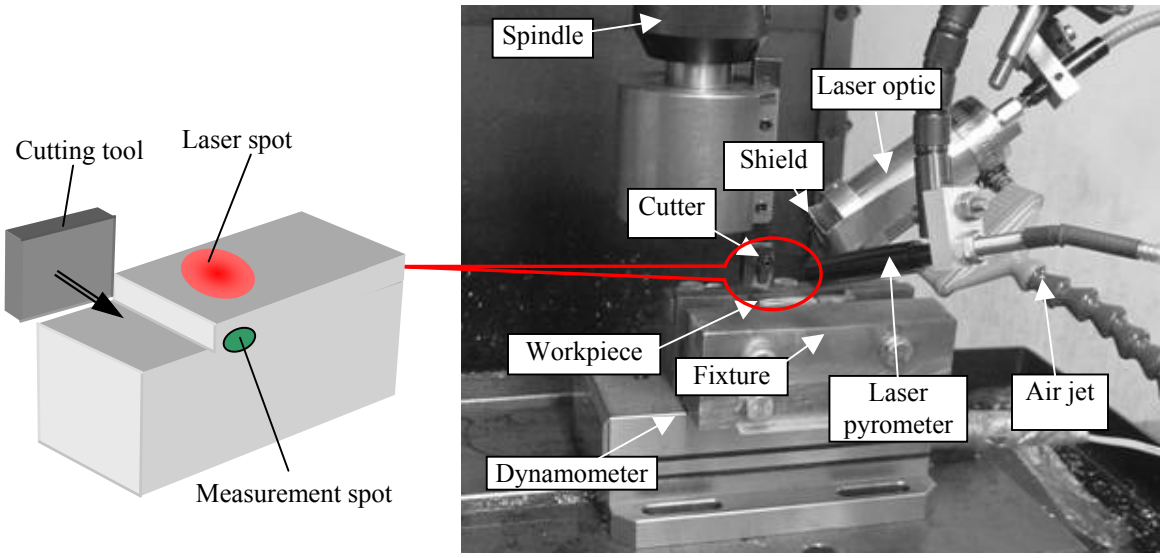

2.1.3.2 Operating Conditions

There are two sets of operating parameters, i.e., the laser parameters and the machining parameters. The machining parameters are cutting speed V, feed f, and depth of cut d. There are five parameters related to laser and pyrometer: laser power Pl, laser beam diameter D_l, laser-tool lead L_l (distance between laser spot and tool edge), preheat time t_p, and pyrometer-laser lead L_{pyro} (center distance between laser beam and pyrometer spot). Since the main purpose is to study the effect of temperature on the machinability, the machining conditions were selected based on some initial tests and fixed in this study. The machining parameters are set as following: the cutting speed V=1 m/s, feed f=0.02 mm/r, d=0.2 mm. As shown in Figure 2.1, the cutting tool has only one cutting edge, f is also the feed per tooth. To simplify the selection for laser parameters, the laser-tool lead and the pyrometer-laser lead were both set at 2.5 mm. Laser

power, laser beam diameter and preheat time were adjusted to achieve the desired temperatures as shown in Table 2.1. The temperature values in the table correspond to the surface temperatures at the measurement spot (Figure 2.1). This spot represents one of the minimum temperature points at the cutting zone. In this section, we use the measured temperature to indicate the workpiece temperature. Thus, the actual material removal temperature of the workpiece, which is defined as the average temperature of material as it enters the shear deformation zone, is slightly higher than this measured temperature.

Table 2.1 Laser Parameters

Laser power (W)	250	270	370	370	390
Laser beam diameter (mm)	3	2.9	3	2.8	2.5
Preheat time (s)	15	17	17	17	19
Temperature °C	838	1172	1349	1480	1595

2.1.4 Results and Discussions

2.1.4.1 Chip Morphology

Chip segments produced by laser assisted milling under 1480 °C and 1595 °C are shown in Figure 2.2a and 2.2b, respectively. The chips appear to be semi-continuous with various lengths. The larger chips at 1595 °C indicate more plastic deformation. Figure 2.3a shows a typical chip microstructure that consists of mostly amorphous lumps of material. Some broken Si3N4 grains are visible. For comparison purpose, the surface microstructure of an as-received workpiece is shown in Figure 2.3b. Interlocking Si_3N_4 grains with amorphous boundary phase can be seen.

Lei et al. (2001) proposed a model to explain the chip formation process in LAM. When the temperature is above 1000 °C, the viscosity of the glassy grain-boundary phase material decreases, which results in chip formation by viscoplastic deformation. This study seems to be a similar case. Based on the temperature dependent property data for the workpiece material, strength reduction begins at 1000 °C. At above 1400 °C, it is reasonable to believe that the glassy phase has become soft enough so that Si_3N_4 grains can slide and rotate with ease under the

advancement of the cutting tool; and this mixture of Si_3N_4 grains and glassy material flows at the shear zone, resulting in semi-continuous chip segments.

Figure 2.2 Optical Micrograph of Semi-continuous Chips at 1480 °C (a) and 1595 °C (b).

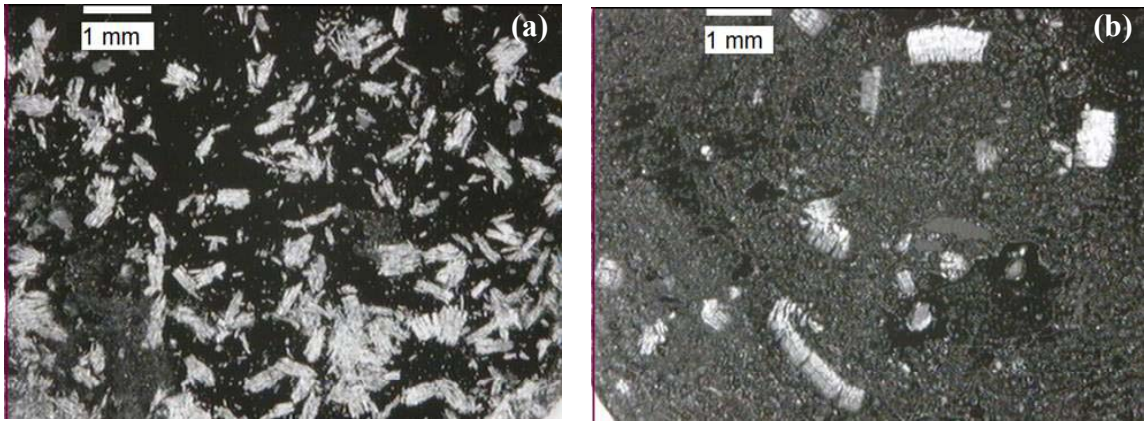

Figure 2.3 SEM micrograph of a highly magnified chip (a) and as-received surface (b).

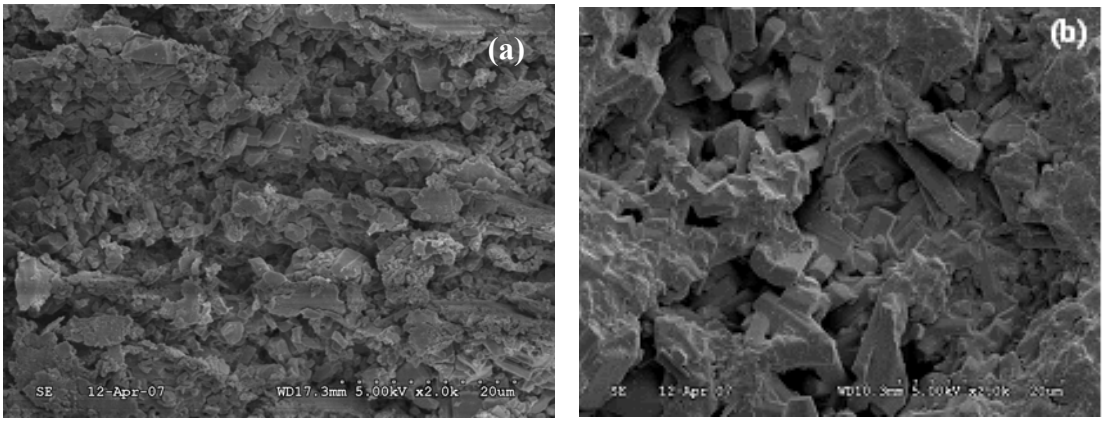

2.1.4.2 Cutting Force

In the experiments, the dynamometer directly measures the x, y and z direction forces, which correspond to tangential (cutting speed direction), radial (feed direction) and axial (vertical direction) force components. The cutting forces provide valuable insights on the effect of laser assistance on machinability. Figure 2.4 shows the typical examples of the dynamic cutting forces. Figure 2.4 (a) shows three cutting records. The spindle rotates 250 rpm. The tooth passes every 0.24 seconds. But the actual material removal time is only 0.0045 seconds per pass. Sampling rate is 2000 data/second. In order to observe the details of the cutting forces, the data between the actual material removal is removed, as shown in Figure 2.4 (b) and (c). The force is cyclic due to the intermittent nature of milling operation. It seems that there are two peaks in each cycle, with the first one at the entry being considerably larger than the one at the exit. This is probably due to the non-uniform temperature distribution across the width of the workpiece. The minimum force in each cycle occurs at the maximum temperature spot. It should be noted that the axial force is the largest of the three force components, which is attributed to the large negative rake chamfer of the cutting tool for the small feed and the depth of cut used in this study.

Figure 2.4 Cyclic cutting force in LAMill.

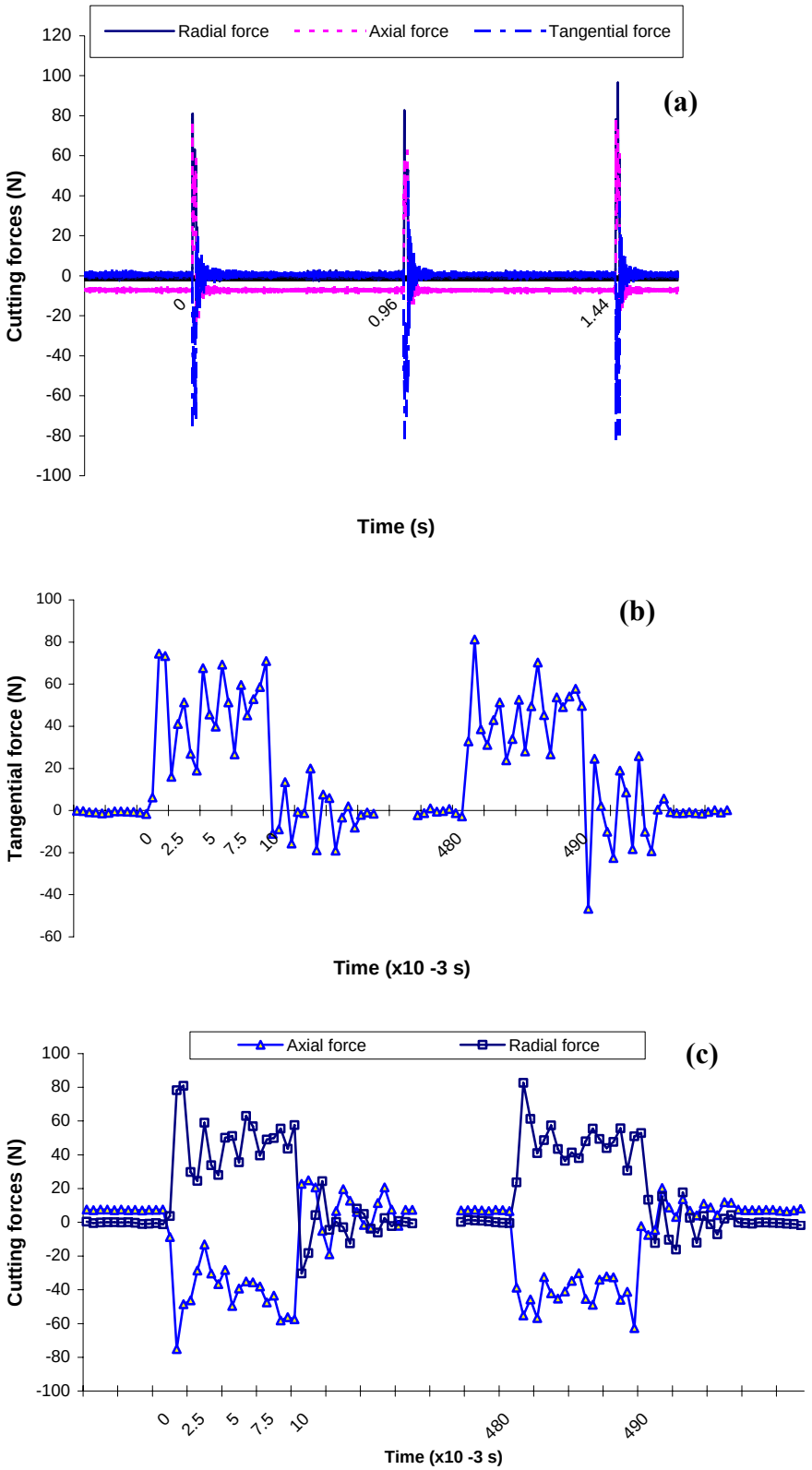

Figure 2.5 shows the variation of the average cutting force with workpiece temperature. It clearly demonstrates that laser heating is an effective method for reducing the cutting force. When the temperature at the measurement point increases from 838 °C to 1319 °C, all the three force components are decreased by approximately 50%. When the temperature increases further, the force continues to decrease but at a reduced rate.

Figure 2.5 Variation of average force with temperature

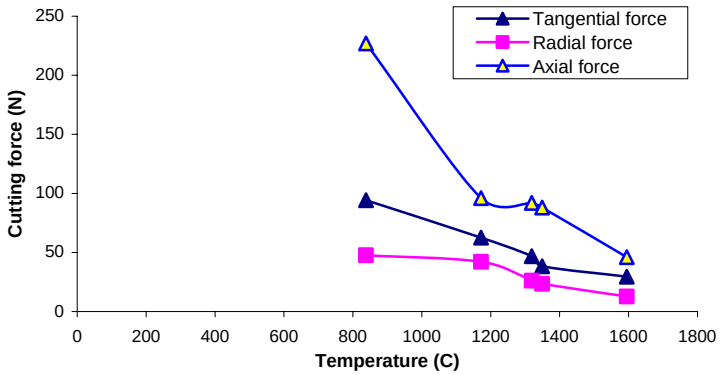

2.1.4.3 Tool Wear

Because LAMill is a very dynamic process with frequent impact of the cutter on the workpiece, hard and brittle cutting tools such as the PCBN insert used in this study are susceptible to failure by fracture. When cutting at low temperature (below the softening point of the glass phase material), edge chipping is the main mode of tool failure, as shown in Figure 2.6. When the workpiece temperature is high enough, tool life is mainly dependent on gradual wear. And for cutting Si_3N_4 ceramics, flank wear is dominant, as shown in Figure 2.7. Therefore, laser assistance improves the machinability of silicon nitride ceramic by avoiding brittle damage to the cutting tool.

Figure 2.6 Tool edge chipping at low temperature.

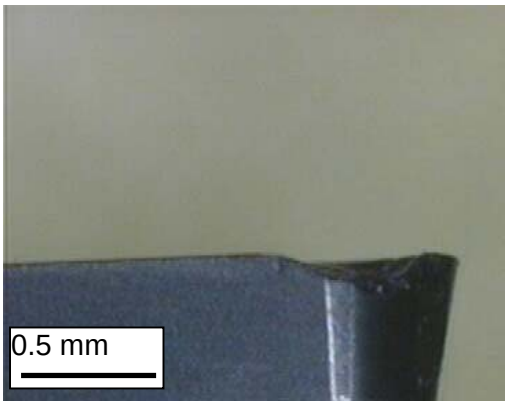

Figure 2.7 Gradual tool wear at high temperature

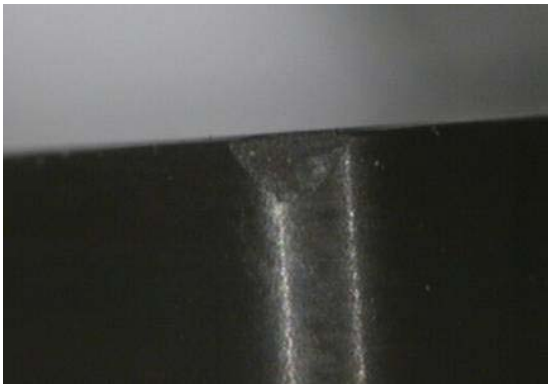

Figure 2.8 shows the progress of maximum flank wear at different workpiece temperature. When the workpiece temperature increases from 1350 °C to 1450 °C, the maximum flank wear is significantly decreased. But further increase of temperature to 1550 °C has less effect on reducing tool wear. This observation fits well with that of the cutting forces. As shown

in Figure 2.5, the cutting forces decrease significantly as temperature increases, but at a reduced rate when temperature is very high. When turning silicon nitride ceramics, Lei et al. (2001) also found that increasing workpiece temperature generally reduced tool wear. But when temperature was very high (above 1500 °C), tool wear slightly increased. This was ascribed to the softening of the insert when its temperature was very high. But in the milling experiments of this study, the temperature of the insert does not increase much even when the workpiece temperature is very high, due to the short tool-workpiece contact time in each tool rotation. Although tool wear is significantly reduced as temperature increases, the tool wear is still serious in LAMill of silicon nitride ceramics, as shown in Figures 2.7 and 2.8.

Figure 2.8 Progress of tool wear at different temperature

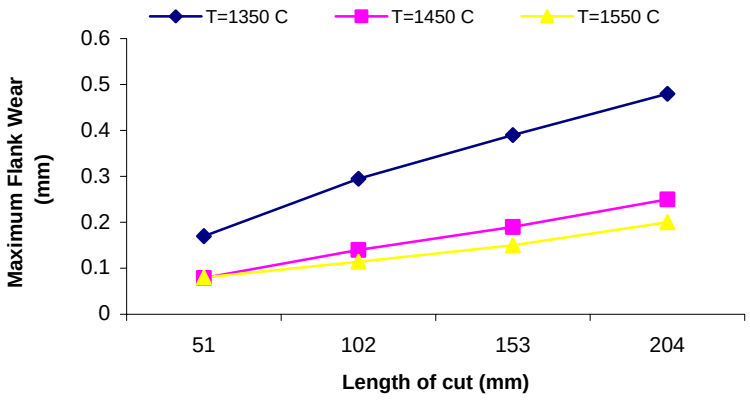

2.1.4.4 Surface Characteristics: Roughness and Microstructure

Figure 2.9 shows a comparison of LAMill-ed and ground surfaces. Laser assisted milling was done at the workpiece temperature of 1349 °C. The ground surface is as-received from the manufacturer. Both surfaces show visible process marks, although they are more pronounced on the ground surface. At a higher magnification, as shown in Figure 2.10, different characteristics are apparent for the two types of machined surfaces. The grinding marks are clearly seen at this magnification, while it is hardly to tell for the LAMill-ed surface. It appears that the LAMill-ed surface is more uniform with some loosely attached particles. These loose particles may be

formed by the displaced surface material under high temperature or even the 'hot fluidic' chips that re-solidify on the machined surface after they are cooled down. In contrast, the ground surface is not uniform, with some seemingly very smooth areas interrupted by irregular microfracture regions.

Figure 2.9 SEM micrograph of LAMill-ed surface (a) and ground surface (b)

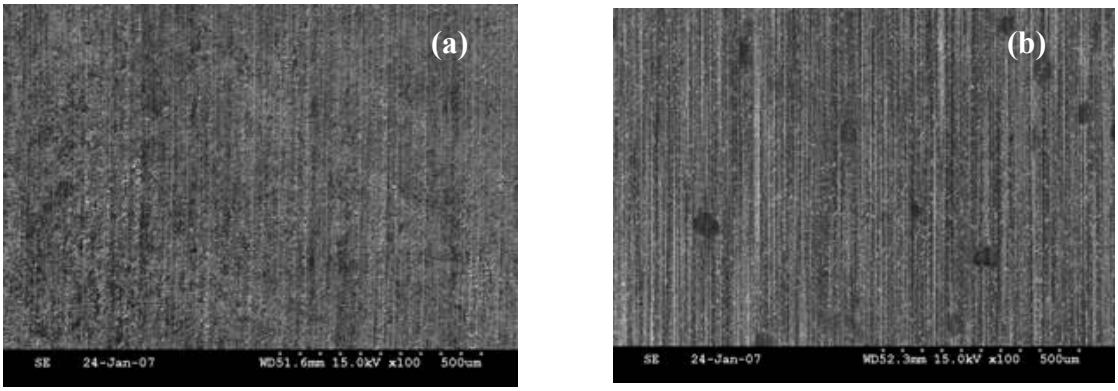

Figure 2.10 Surface microstructure of LAMill-ed surface (a) and ground surface (b)

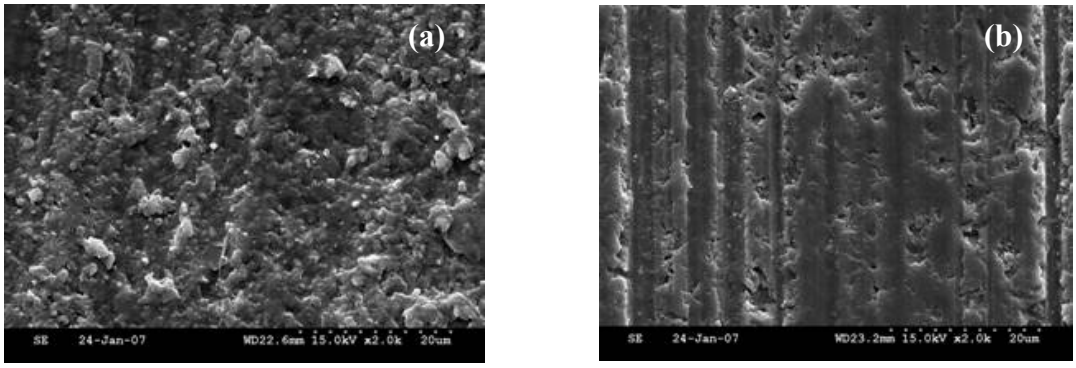

The different surface characteristics demonstrate the differences in material removal mechanisms for LAMill and grinding. In LAMill, material is first softened and then mainly removed by shear-induced flow under intergranular fractures. This mechanism results in fewer microfracture and damage zones on the machined surface. It is reasonable to believe that

microcracks below this surface layer may not exist after LAMill. But in grinding, material is removed mainly by brittle contact between diamond abrasives in the grinding wheel and the brittle workpiece, forming heavily damaged areas. Some abrasive grains merely smear over the surface, producing some smooth regions.

The surface roughness R_a of the LAMill-ed parts under different temperatures are measured using a Suftest-402 (Mitutoyo Corporation) surface profilometer. The as-received ground parts are also measured for comparison purpose. As seen in Table 2.2, the surface roughness R_a from laser assisted milling is about 0.3 to 0.4 μm when the temperature is above 1000 °C, while the surface roughness of the ground surface is about 0.4 to 0.5 μm. The results show that surface roughness is not very sensitive to the workpiece temperature when the temperature is higher than about 1200 °C in laser assisted milling.

Table 2.2 Surface Roughness

	LAMill-ed surface				Ground surface
Temperature °C	838	1172	1349	1595	RT
R_a (μm)	0.43	0.32	0.3	0.35	0.4
R_{max} (μm)	3.5	2.7	2.2	2.6	2.8

2.1.4.5 Edge Chipping

Edge chipping is a form of typical machining induced ceramic damage. Ng et al. (1996) and Cao (2001) described three kinds of edge chipping when milling glass ceramics: entry edge chipping, interior edge chipping and exit edge chipping. Entry edge chipping is mainly caused by the impact of the cutting tool on the workpiece when the tool initially contacts the workpiece. Interior edge chipping is due to the brittle nature of ceramic material and occurs along the cutting path. Exit edge chipping is formed due to the sudden release of the stress energy built in the machining process and is related to the loss of material support when the tool is leaving the workpiece. Due to the high hardness and brittleness of silicon nitride, macroscale edge chipping

is very common and hard to avoid in milling operation at room temperature. However, in laser assisted machining, the increased workpiece temperature was found to greatly help reduce edge chipping as shown in Figure 2.11 and 2.12. . In our milling experiments with laser assistance, there is no macroscale entry edge chipping and interior edge chipping observed when the temperature is higher than 1000 °C, as shown in Figure 2.12 and 2.15. The reduction in edge chipping is attributed to increased material ductility and reduced cutting force with temperature. But macroscale exit edge chipping could not be completely avoided even when the temperature is very high (above 1400 °C), though the size of exit edge chipping decreases quickly when the temperature increases, as shown in Figure 2.12 and 2.14.

Figure 2.11 Edge Chipping at T=838 °C

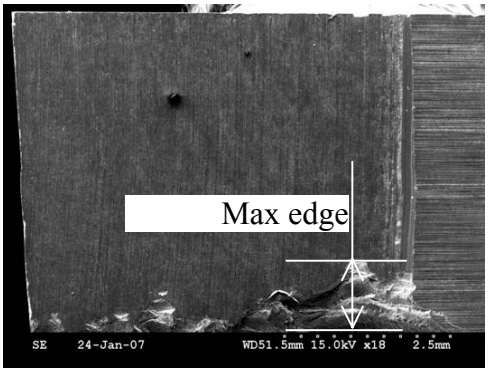

Figure 2.12 Edge Chipping at T=1349 °C

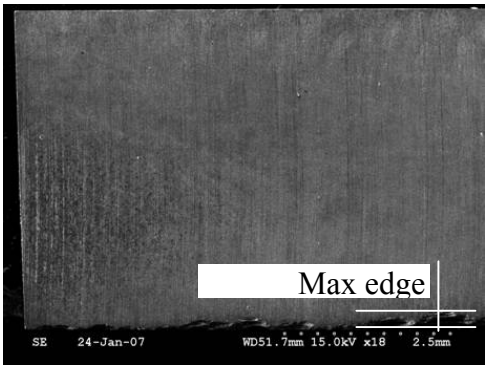

Edge chipping in brittle material is related to a quantity known as edge toughness, which is defined as the slope of the approximately linear relationship between the distance of indentation from the edge and the force required to create a flake in an indentation test (McCormick and Almond, 1990). Quinn and Mohan (2005) investigated the changes in edge toughness and chip geometry when chips were formed from forces that were not perpendicular. It was found that a greater force was required to produce a chip when the force was angled away from the edge. Cao (2001) demonstrated that the size of exit edge chipping was strongly related to the loading orientation and location in milling of glass ceramics. It was concluded that the exit edge chipping was mainly caused by loss of material support when the cutter was leaving the workpiece. Therefore, LAMill experiments were conducted to study the effect of exit angle on exit edge chipping. An exit angle is defined as the angle between the workpiece exit edge and the machining edge, as shown in Figure 2.13.

Figure 2.13 Definition of Exit Angle

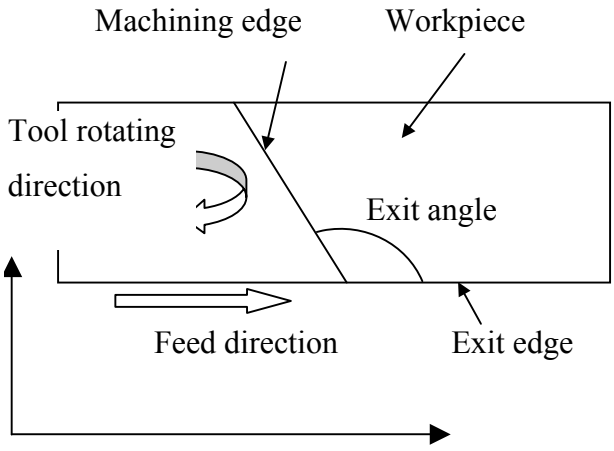

Figure 2.14 Temperature and Exit Edge Chipping

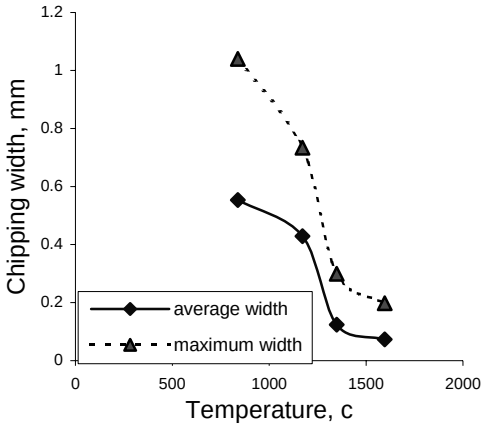

Figure 2.15 shows an example of the machined surface with an exit angle of 126º under a temperature of 1231°C. No visible macroscale edge chippings are observed, although a magnified picture shows some microscale exit edge chippings.

Figure 2.15 Machined surface at Different Magnifications, Exit Angle=126º, T=1231°C

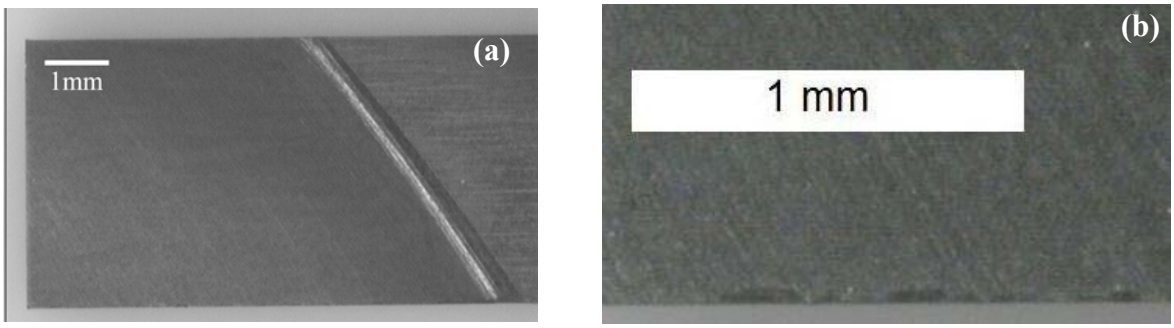

The effect of exit angle was examined under two different temperature levels. The low level temperature is 1156 °C ± 41 °C and the high level temperature is 1346 ± 9 °C. The variation of chipping width with exit angle is shown in Fig.16 for the low temperature and in Figure 2.17 for the high temperature condition. It is demonstrated that changing the exit angle away from perpendicular will reduce the exit chipping size significantly. When the exit angle is

decreased from 86° (approximately perpendicular) to 50°, the average chipping width reduces slightly from 0.43 mm to 0.40 mm for the low temperature, and from 0.12 mm to 0.082 mm for the high temperature. But changing exit angle to a blunt angle (larger than 90°) has much bigger effect on reducing the edge chipping. This result is reasonable because there is more supporting material ahead of the cutter than the case with exit angle smaller than 90°. The average chipping width reduces to 0.11 mm for the exit angle of 110° and further down to 0.034 mm for 126° (Figure 2.16). At the high temperature level, no macroscale exit edge chippings are observed under exit angle of 110° and 126°. As shown in Figure 2.17, exit edge chippings are very small with average chipping width of 0.063 mm for the exit angle of 110° and 0.012 mm for the exit angle of 126°.

Figure 2.16 Effect of Exit Angle on Chipping Size, T=1156 °C ± 41 °C

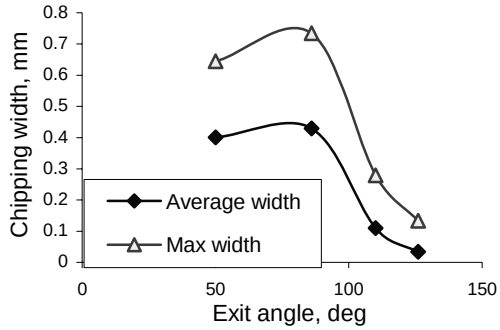

Figure 2.17 Effect of Exit Angle on Chipping Size, T=1346 °C ± 9 °C

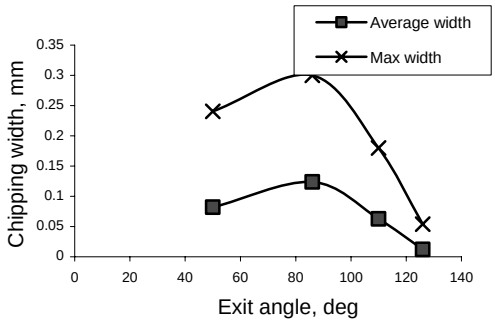

Changing the exit angle away from 90° will greatly decrease the tangential force Fy. As shown in Figure 2.18, Fy deceases from 62.8 N to 5.2 N and 3.0 N when the exit angle changes from 86° to 110° and 50°, respectively. When the angle increases to 126°, Fy becomes as small as 0.77 N. It was shown by Cao (2001) that the Y direction force plays a big role to exit chippings. Therefore, the reduction in Fy will greatly help reduce exit edge chipping. Although Fx increases when Fy decreases, the X direction force has small effect on exit edge chippings. Fz also contributes to exit edge chipping. When the exit angle changes from less than 90° to a blunt angle, Fz decreases slightly. This will also help reduce the size of exit edge chipping.

Figure 2.18 Effect of Exit Angle on Cutting Force

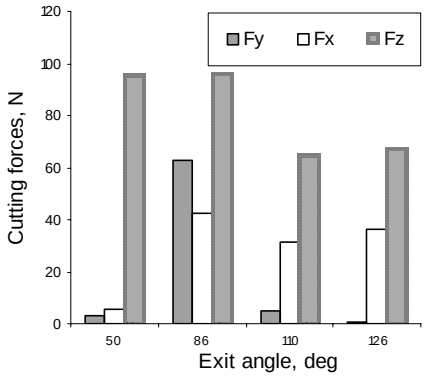

2.1.5 Conclusions

The conclusions from this study are summarized below.

(1) Laser assistance significantly enhances the machinability for silicon nitride ceramics, enabling the material to be cut by milling without breaking the cutting tip. Material removal in laser assisted milling shows plastic deformation characteristics and the size of machined chips increases as temperature increases.

(2) Cutting force decreases significantly as workpiece temperature increases. Tool wear is serious and highly dependent on the workpiece temperature.

(3) Very good surface finish is obtained in LAMill. The LAMill-ed surface shows consistent characteristics without large microcrack zones.

(4) Temperature and exit angle are the two main parameters that affect exit edge chipping. When temperature is higher than 1000 °C, no visible entry edge chipping is observed. And exit edge chipping decreases considerably as the temperature increases. Reduced edge chipping at high temperatures is a result of decreased cutting forces.

(5) Controlling the exit angle is an effective and economic way to eliminate the macroscale exit edge chipping. There are more supporting material ahead of the cutter when the exit angle is large so that less and smaller edge chippings are formed. A blunt exit angle will also help reduce the exit edge chipping by greatly reducing the Y direction cutting force and slightly reducing Z direction force that are directly related to exit edge chippings.

2.1.6 Acknowledgements

Financial support of this work by the National Science Foundation under Grant No. DMI-0134579 is gratefully acknowledged.

2.1.7 References

Cao, Y., 2001, “Failure Analysis of Exit Edges in Ceramic Machining Using Finite Element Analysis,” Engineering Failure Analysis, Vol. 8, pp. 325-338.

Jeon, Y., and Pfefferkorn, F. E., 2005, "Effect of Laser Preheating the Workpiece on Micro-End Milling of Metals," Proceedings of IMECE2005, 2005 ASME International Mechanical Engineering Congress and Exposition, 10p.

Klocke, F., and Bergs, T., 1997, "Laser-Assisted Turning of Advanced Ceramics," Proceedings of SPIE: Rapid Prototyping and Flexible Manufacturing, 3102, pp. 120-130.

König, W., and Zaboklicki, A. K., 1993, "Laser-Assisted Hot Machining of Ceramics and Composite Materials," International Conference on Machining of Advanced Materials, Gaithersburg, MD, NIST special Publication, Vol. 847, pp. 455-463.

Lei, S., Shin, Y. C., and Incropera, F. P., 2001, "Experimental Investigation of Thermo-Mechanical Characteristics in Laser Assisted Machining of Silicon Nitride Ceramics," ASME Journal of Manufacturing Science and Engineering, Vol. 123, pp. 639-646.

McCormick, N.J., Almond, E. A., 1990, “Edge Flaking of Brittle Materials,” Journal of Hard Materials, Vol. 1, No. 1, pp. 25-51.

Ng, S., Le, D., Tucker S., Zhang G., 1996, “Control of Machining Induced Edge Chipping on Glass Ceramics,” American Society of Mechanical Engineers, Manufacturing Engineering Division, MED, Vol. 4, International Symposium on Information Storage and Processing Systems, pp. 229-236.

Pfefferkorn, F. E., Incropera, F. P., and Shin, Y. C., 2005, "Heat Transfer Model of Semi-Transparent Ceramics Undergoing Laser-Assisted Machining," International Journal of Heat and Mass Transfer, Vol. 48, pp. 1999-2012.

Pfefferkorn, F. E., Shin, Y. C., Incropera, F. P., and Tian, Y., 2004, "Laser-Assisted Machining of Magnesia-Partially-Stabilized Zirconia," ASME Journal of Manufacturing Sciences and Engineering, Vol. 126, No. 1, pp. 42-51.

Quinn, J., and Mohan, R., 2005, “Geometry of Edge Chips Formed at Different Angles,” Ceramic Engineering and Science Proceedings, Vol. 26, No. 2, Mechanical Properties and Performance of Engineering Ceramics and Composites, A Collection of Papers Presented at the 29th International Conference on Advanced Ceramics and Composites, pp. 85-92.

Rebro, P. A., Pfefferkorn, F. E., Shin, Y. C., and Incropera, F. P., 2002, "Comparative Assessment of Laser-Assisted Machining for Various Ceramics," Transactions of NAMRI/SME, Vol. 30, pp. 153-160.

Rozzi, J. C., Incropera, F. P., and Shin, Y. C., 2000a, "Transient, Three-Dimensional Heat Transfer Model for the Laser Assisted Machining of Silicon Nitride: Ii-Assessment of Parametric Effects," International Journal of Heat and Mass Transfer, Vol. 43, pp. 1425-1437.

Rozzi, J. C., Pfefferkorn, F. E., Incropera, F. P., and Shin, Y. C., 2000b, "Transient, Three-Dimensional Heat Transfer Model for the Laser Assisted Machining of Silicon Nitride: I-Comparison of Predictions with Measured Surface Temperature Histories," International Journal of Heat and Mass Transfer, Vol. 43, pp. 1409-1424.

Shen, X., and Lei, S., 2005, "Distinct Element Simulation of Laser Assisted Machining of Silicon Nitride Ceramics," Proceedings of IMECE2005, 2005 ASME International Mechanical Engineering Congress and Exposition, 8p.

Shen, X., Liu, W. J., and Lei, S., 2005, "Three-Dimensional Thermal Analysis for Laser Assisted Milling of Silicon Nitride Ceramics Using FEA," Proceedings of IMECE2005, 2005 ASME International Mechanical Engineering Congress and Exposition, 8p.

Singh R. and Melkote, S., 2005, “Experimental Characterization of Laser-Assisted Mechanical Micromachining (LAMM) Process”, Proceedings of IMECE 2005, International Mechanical Engineering Congress and Exposition, Orlando, Florida, USA, pp. 957-964.

Tian, Y., 2006, Laser-assisted machining of silicon nitride with complex features, Ph.D. dissertation, Purdue University.

Tian, Y., and Shin, Y. C., 2006, "Thermal Modeling for Laser-Assisted Machining of Silicon Nitride Ceramics with Complex Features," ASME Journal of Manufacturing Science & Engineering, Vol. 128, pp. 425-434.

Tian, Y., and Shin, Y. C., In Press, "Thermal Modeling and Experimental Evaluation of Laser-Assisted Dressing of Superabrasive Grinding Wheels," Journal of Engineering Manufacture.

2.2 Mechanisms of Edge Chipping in Laser Assisted Milling of Silicon Nitride Ceramics

Published in:

International Journal of Machine Tools and Manufacture, Vol. 49, No. 3-4, 2009, pp.344-350.

Author's Names:

Budong Yang, Xinwei Shen, Shuting Lei

Author's Affiliation:

Department of Industrial and Manufacturing Systems Engineering, Kansas State University, 212 Durland Hall, Manhattan, KS 66506

2.2.1 Abstract

This section investigates the mechanisms of edge chipping at elevated temperature in laser assisted milling (LAMill) of silicon nitride ceramics. Experimental results show that the elevated temperature can significantly reduce workpiece edge chipping through softening and toughening mechanisms. When the temperature is above the softening point and below the brittle/ductile transition temperature, the mechanism of elevated temperature on reducing edge chipping is through softening to decrease the cutting forces. When the temperature is above the brittle/ductile transition temperature, the edge toughness of silicon nitride ceramics is significantly increased. Both softening and toughening mechanisms take effect to reduce workpiece edge chipping. It is shown that temperature range between 1200 to 1400°C has the most significant effect to reduce edge chipping in LAMill of silicon nitride ceramics.

Key Words:

Edge chipping, Laser assisted milling, Silicon nitride ceramic, Softening, Toughening, Edge toughness.

2.2.2 Introduction

Advanced structural ceramics are wear-resistant, corrosion-resistant and lightweight materials with very high temperature strength and have been increasingly used in automotive, aerospace, military, medical and other applications. Due to the distortion, contraction, limited formability and lack of dimensional control in net-shape processes for structural ceramics, machining is necessary to obtain the desired surface finish and dimensional tolerance. However, machining of ceramic can be very difficult due to its high hardness and brittleness. Various nontraditional machining procedures have been used in fabricating ceramic parts, including ultrasonic machining (Pei, et. al 1995), electrical-discharge machining (Petrofes and Gadalla, 1988) , laser machining (LM) (Islam and Campbell, 1993) and laser assisted machining (LAM) (Zaboklicki, 1993). In recent years, LAM has been shown to be a very promising method to decrease the cost, improve the efficiency and reduce the surface/subsurface defects. LAM offers important advantages over traditional machining such as reduced power per volume of machined part, higher material removal rate, decreased cutting force, reduced chatter, small residual stresses, reduction of tool wear, avoidance of tool breakage and crack-free machined surface (Zaboklicki, 1993; Lei, e al., 2001). Lei et al. (2006) conducted some fundamental investigations on laser assisted milling of silicon nitride ceramic. The authors examined the workpiece temperature, the surface integrity and tool wear. The effects of laser parameters (laser power, preheat time and laser beam diameter) and milling parameters (feed rate and cutting speed) were investigated. Yang et al. (2007) demonstrated the machinability and feasibility of milling silicon nitride ceramics under laser assistance. It was shown that material removal had more plastic characteristics when the temperature was high. The cutting forces and specific cutting energy decreased as workpiece temperature increased. No brittle damage to the cutting tool was observed and surface roughness of the machined surface was comparable to that of ground surface. However, edge chipping, a commonly observed phenomenon during the machining of ceramic material, could not be completely avoided even when the temperature was above 1400°C (Yang et al., 2007).

Edge chipping of ceramics is a sudden fracture-controlled macro-scale or micro-scale edge damage. Its presence on finished products not only affects dimensional and geometric accuracy, but also causes potential severe failure of the ceramic component due to the microcracks left on the machined surface. Edge chipping usually happens when cutting edge comes into contact with or separates from the workpiece. Ng et al. (1996) and Cao (2001) described three kinds of edge chipping when milling glass ceramics: entry edge chipping, interior edge chipping and exit edge chipping. Entry edge chipping is mainly caused by the impact of the cutting tool on the workpiece when the tool initially contacts the workpiece. Interior edge chipping is due to the brittle nature of ceramic material and occurs along the cutting path. Exit edge chipping is formed due to the sudden release of the stress energy built in the machining process and is related to the loss of material support when the tool is leaving the workpiece. Yang et al. (2007) demonstrated that the raised temperature in LAMill could eliminate macro-scale entry and interior edge chippings, but macro-scale exit edge chipping could still be observed by visual examination, though the size of exit edge chipping decreased significantly when temperature increased. This study will investigate the mechanisms of elevated temperature on edge chipping in LAMill of silicon nitride ceramics so that the edge damage could be better controled in an acceptable level while realizing possible maximum material removal rate.

2.2.3 Edge Toughness and Chipping Size

2.2.3.1 Definition of Edge Toughness

Edge chipping in processing ceramics is a significant limitation in the design, handling and use of ceramic components. Trying to understand how the phenomenon occurs has been the subject of research over several decades. McCormick and Almond (1986, 1990) studied the mechanics on a variety of materials with indentation method by loading the surface near an edge with a diamond indenter. It was found that there was an approximately linear relationship between the distance of indentation from the edge and the force required to create a flake. The slope of this relationship is defined as “edge toughness”, which provides information about the edges of materials rather than the bulk or surface characteristics. Plotting the load P, which is required to produce an edge flake, against the distance d between the center of the indent and the edge, reveals a linear relationship:

$$T_e = \Delta P / \Delta d \qquad (1)$$

where T_e is edge toughness.

It has found that edge toughness is related to critical strain energy release rate G_{Ic} or fracture toughness K_{Ic} (Mcormick, 1982; Quinn, et al., 2000; Morrell, 2005; Morrell and Gant, 2001). Though there is no general quantitative relationship between edge toughness and these properties, larger fracture toughness usually result in smaller edge chip size. This indicates that the more brittle the material is, the easier it is to form edge damage. Therefore, there are basically two ways to reduce the size of workpiece edge chipping in machining of ceramics: by improving the workpiece's edge toughness and by reducing the cutting force related to edge chipping formation without sacrificing material removal rate.

2.2.3.2 Edge Toughness of Silicon Nitride Ceramics

Many studies have been conducted to investigate the edge toughness of silicon nitride ceramics at room temperature (Gogotsi, 2006; Gogotsi, et al., 2005; Gogotsi and Mudrik, 2004). The measured edge toughness for typical silicon nitride ceramics at room temperature ranges from 400 to 580 N/mm. It has been shown that there is a monotonic relationship between edge toughness and fracture toughness at room temperature [McCormick, 1982; Gogotsi, et al., 2005; Scieszka, 2005).

The silicon nitride ceramic used in this study is Ceralloy® 147-31N, which is made by Ceradyne, Inc. Table 2.3 shows the main mechanical properties of the silicon nitride material. It is a gas pressure sintered reaction bonded Si_3N_4 with very good fracture toughness of 6.0 $MPa{\cdot}m^{1/2}$. This material is very close to the GPSSN investigated by Gogotsi, et al. (2005) with an edge toughness of 567 N/mm and fracture toughness of 5.36 $MPa{\cdot}m^{1/2}$. According to the monotonic relationship between edge toughness and fracture toughness, the edge toughness of the Ceralloy® 147-31N silicon nitride at room temperature could be above 580 N/mm. However, ceramics usually exhibit much lower fracture resistance in their practical applications than suggested from lab fracture toughness results. Under the extensive dynamic load of laser assisted milling, it is reasonable to expect a much lower fracture toughness and edge toughness.

Table 2.3 Mechanical properties of the Ceralloy® 147-31N silicon nitride at room temperature

Flexural Strength (MPa)	Elastic Modulus (GPa)	Hardness HV (0.3) kg/mm^2	Fracture Toughness (MPa·m$^{1/2}$)	Poisson's Ratio
700-800	310	1450	6.0	0.27

The mechanical behavior of silicon nitride at high temperature differs significantly with that at room temperature. The intergranular glassy phase may undergo a glass transition at around 1000 °C. Crystalization may start above this temperature and secondary liquid phases may form around 1300 °C. Finally, decomposition may occur at higher temperature. All these microstructure changes have effects on the elastic modulus, strength and fracture toughness of silicon nitride ceramics, therefore have effects on edge toughness.

Rouxel (2001) observed a rapid softening for silcion nitride ceramics when the temperature is above 1150°C, which is the glass transition temperature T_g. When temperature increases from room temperature up to the glass transition temperature T_g, the elastic modulus of silicon nitride ceramics decreases steadily at a slow rate. When temperature is above T_g, the elastic modulus is often seen a sharp drop and then decreases steadily at a slower rate with rising temperature. Strength usually has a similar relationship with temperature as elastic modulus does. However, some silicon nitride ceramics, such as the gas pressure sintered silicon nitride studied by Kohler et al. (1992), have a slight increase in strength around 1250°C. This increase has been related to a large variation in the inherent defect distribution of the material. Figure 2.19 shows the schematic diagram of the changes in fracture toughness, elastic modulus and strength with rising temperature.

There are two mechanisms affecting the fracture toughness of silicon nitride ceramics when temperature is above T_g. First, the softening of the intergranular phase enables slow crack growth at lower and lower loads, resulting in a significant decrease of fracture toughness. Second, as the secondary phase is softening, it becomes more and more difficult to initiate crack propagation from a preexisting flaw, because energy dissipation occurs through viscoelastic flow in the vicinity of the flaw. Grain boundary sliding processes lead to the formation and growth of microcracks in the stress field near the crack tip and to macroscopical crack branching. These processes provide an additional contribution to the energy dissipation and therefore tend to

increase K_{Ic}. The softening and toughening mechanisms work together to determine if the fracture toughness decreases or increases with temperature.

Figure 2.19 Schematic diagram of the Mechanical Properties and Temperature for Si_3N_4

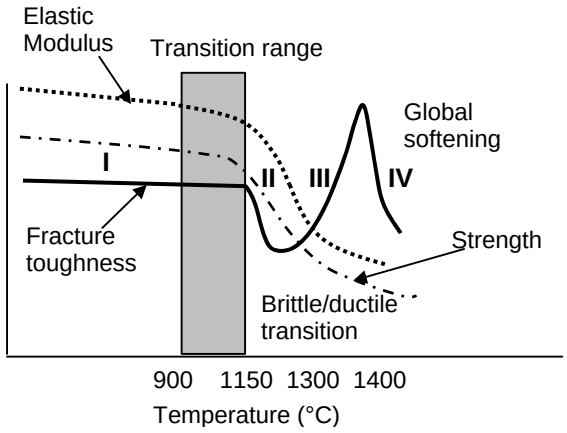

I: elastic range; II: rapid softening; III: semi-ductile regime; IV: enhanced ductile regime. (Modified based on Rouxel, 2001)

The relationship between the fracture toughness and temperature is shown in Figure 2.19. When temperature is lower than the glass transition temperature T_g (around 1150°C), linear elastic fracture mechanics relationship holds and the fracture toughness decreases slightly with temperature (stage I in Figure 2.19). When temperature is above T_g, fracture toughness drops

rapidly with the rapid softening of the secondary glassy phases (stage II). The softening mechanism dominates in this stage, resulting in a significant decrease of fracture toughness. However, an increase of the fracture toughness is generally observed in a temperature when brittle/ductile transition happens (stage III). At this stage, the toughening mechanism dominates and provides additional contribution to the energy dissipation to increase K_{Ic}. When temperature increases further to the viscous flow regime, global softening happens (stage IV). The softening of the intergranular phase overcomes the energy dissipative contribution of the toughening mechanism. K_{Ic} decreases with rising temperature.

2.2.3.3 Definition of Chipping Characteristics

Figure 2.20 shows a schematic diagram of chipping characteristics in an actual workpiece and the definition of chipping. The dotted line represents the original edge profile which is the original edge line before machining, ideally without edge defects. The curve represents the edge profile after laser assisted machining. The gaps between the dotted line (the original edge profile) and the curve (the edge profile after machining) are the edge chippings formed during machining. Please refer to Ohbuchi et al. (1995) for a similar definition of edge chipping in slot grinding.

Figure 2.20 Definition of Edge Chipping

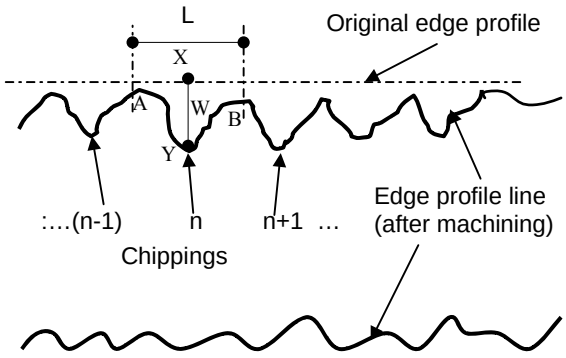

A chipping is defined as it starts at one peak point of the edge profile line and finishes at the following peak point of the edge profile line. As shown in Figure 2.20, for example, chipping 'n' starts at A and ends at B along the edge profile. The length A-B is defined as chipping length (L). The distance from the original edge line to the deepest point of a chipping profile line X-Y is defined as chipping width (W). And chipping area is defined as the area surrounded by the edge profile line and the original edge line. These values define the chipping characteristics of the machined surface. It is clear from the definition of chipping that the number of chipping, each chipping length and each chipping area are dependent on the definition of a chipping. But the total chipping area and maximum chipping width are independent of the chipping definition. Since total chipping area depends on the machining length, this study uses average chipping width and maximum chipping width to describe the chipping characteristics. Average chipping width is the total chipping area divided by the machining length.

2.2.4 Experimental Setup

2.2.4.1 Experimental System

The experimental system for LAMill of silicon nitride is illustrated in Figure 2.21.

Figure 2.21 Schematic of LAMill experimental system.

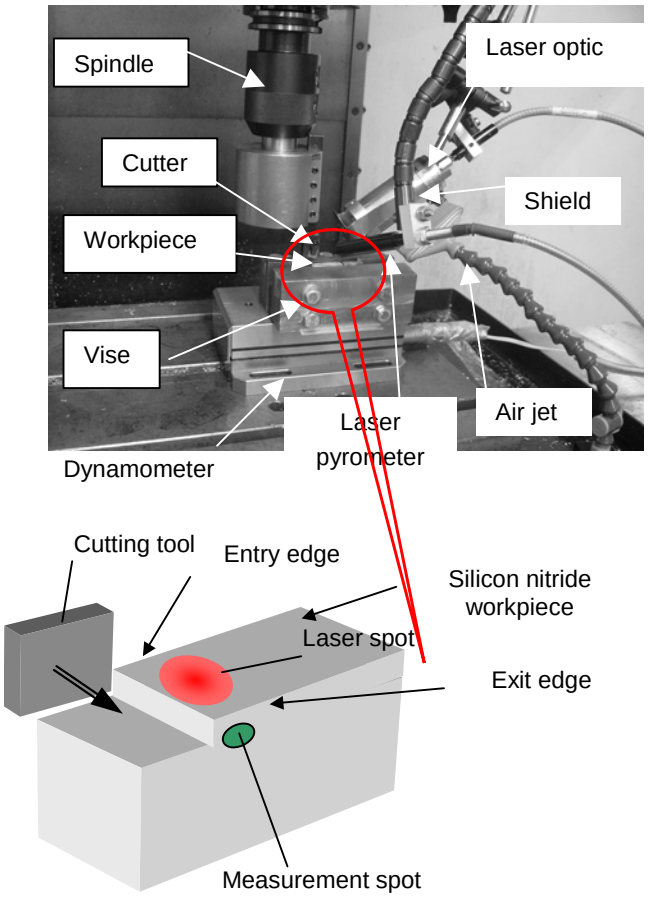

The milling operation is carried out on a CNC milling center. A diode laser system is used to generate a high power laser beam, which is delivered through the optical fiber and focused on the workpiece surface at the angle of 60 deg. The laser focusing end is fixed on the spindle and cooled by blowing air during milling to prevent the optics from being overheated. A laser pyrometer with a range of 450 - 1750 °C is used to concurrently measure the temperature of the cutting zone. The pyrometer is also fixed on the spindle. During milling, the cutting tool, the laser beam and the pyrometer do not move (the cutter rotates though) while the workpiece moves with the worktable. Therefore, the relative distances among the laser spot, the cutter and the measuring spot remain the same during each milling pass.

The Si_3N_4 workpiece is a beam type with dimensions of 4.3 x 5.3 x 48 mm. The workpiece is mounted on a Kistler dynamometer which is used to measure the global x, y, and z direction forces. The electrical charges from the dynamometer are converted to voltage signals by a Kistler charge amplifier. The cutting force and temperature data are recorded on a computer automatically during each cut. In order to minimize heat loss, the workpiece is padded with two plates of asbestos. A polycrystalline cubic boron nitride (PCBN) tipped insert is clamped in a self-made tool holder with a diameter of 76.2 mm.

2.2.4.2 Operating Parameters

It is very important in laser assisted machining to select operating parameters to achieve proper workpiece temperature and its distribution. The temperature and its distribution depend on two sets of operating parameters, i.e., the laser parameters and the machining conditions. The machining conditions are cutting speed (V), feed (f) and depth of cut (d). There are five parameters related to laser and pyrometer: laser power, laser beam diameter , laser-tool lead (distance between laser spot and tool edge), preheat time, and pyrometer-laser lead (distance between laser and pyrometer spots). The laser and machining parameters are chosen to achieve a nearly uniform temperature distribution from the surface to depth of cut and nearly constant temperature in the cutting zone throughout the duration of each LAMill test. Unless otherwise specified, the machining parameters are shown in Table 2.4. The machining parameters are selected based on some preliminary tests. It has been shown that the machining quality is acceptable and consistent under these machining conditions. The laser-tool lead is set to 2.5 mm and the pyrometer-laser lead is 2.5 mm. To achieve the desired temperature, laser power and laser beam diameter are changed and preheat time is adjusted accordingly, as shown in Table 2.4.

Table 2.4 Operating parameters

Machining Parameters			
Parameter	V (m/s)	f (mm/r)	d (mm)
Value	1	0.02	0.2
Laser Parameters			

Temperature °C	838	1017	1172	1319	1349	1595
Laser power (W)	250	260	270	360	370	390
Laser beam diameter (mm)	3	2.9	2.9	3	3	2.5
Preheat time (s)	15	16	17	17	17	19

2.2.5 Results and Discussion

2.2.5.1 Effect of Elevated Temperature on Edge Chipping

Edge chipping is a form of typical machining induced ceramic damage. Due to the high hardness and extremely brittleness of silicon nitride, serious macro-scale edge chipping is very common and hard to avoid in machining silicon nitride at room temperature. In fact, either the cutting tool or the workpiece will be damaged by brittle fracture when cutting silicon nitride at room temperature under the machining conditions of Table 2.4 (Lei, et al., 2006). However, it is shown that elevated temperature can significantly improve the machinability of silicon nitride ceramics. In order to observe the effect of elevated temperature on edge chipping, laser assisted milling experiments are conducted at 838 °C, 1017°C, 1172°C, 1319°C, 1349°C and 1595°C respectively. These temperatures are measured at the surface close to the laser spot and the average temperatures of the cutting zone are slightly lower than the measured temperatures.

Experimental results show that in laser assisted machining, the increased workpiece temperature could greatly reduce edge chipping. When silicon nitride is machined under its softening point (Figure 2.22a), there are some macroscale entry edge chippings. Figure 2.22b shows that there is no macroscale entry edge chipping and interior edge chipping observed when the temperature is higher than silicon nitride's softening temperature. And the size of exit edge chipping decreases significantly when temperature increases from 838 °C to 1349°C. Figure 2.23 shows the relationship of exit edge chipping width with temperatures. The exit edge chipping size decreases steadily with temperature up to 1000°C. When temperature is higher than the glassy transition temperature (1150°C), the chipping size decreases quickly with rising temperature and there is a dramatic drop of the chipping size around 1300°C. Then the decreasing rate of chipping size slows down when temperature increases further.

Please note that although the size of exit edge chipping decreases quickly when the temperature increases, macroscale exit edge chipping could not be completely avoided even when the temperature is very high (above 1400 °C).

Figure 2.22 Edge chipping at (a) T=838 °C, (b) T=1349°C

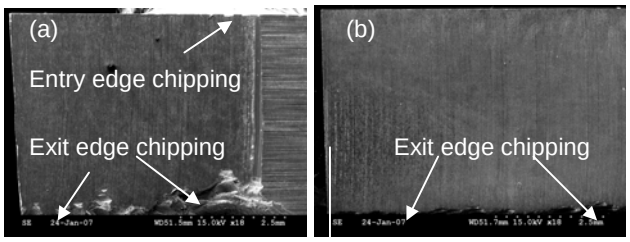

Figure 2.23 Temperature and Exit Edge Chipping

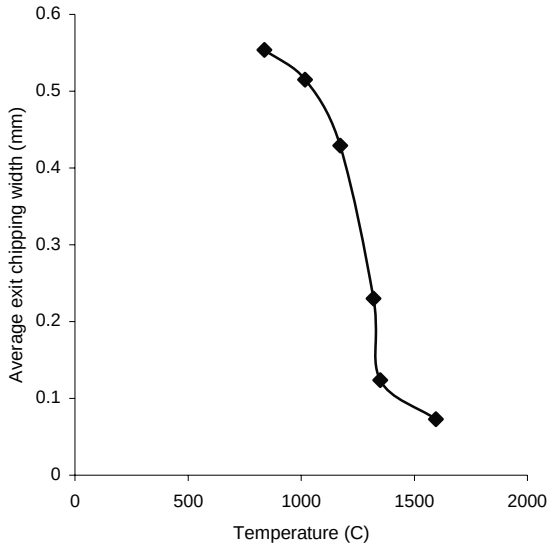

2.2.5.2 Mechanisms of Edge Chipping at Elevated Temperature

Many studies have shown that heating could change the mechanical behavior of silicon nitride ceramics from brittle to ductile (Pei et al., 1995; Petrofes and Gadalla, 1988; Islam and Campbell, 1993; König and Zaboklicki, 1993). As discussed in Section 2.2.3.2, high temperatures will induce microstructure changes of silicon nitride ceramics, which have effects on the hardness, elastic modulus, strength, fracture toughness and edge toughness. The changes of these properties affect edge chipping through two mechanisms: The first is to decrease the cutting force as the material is softened. According to equation (1), smaller forces will generate smaller chippings even if the edge toughness does not increase; The second is to improve the workpiece's edge toughness at certain temperature ranges. According to equation (1), chipping size will decrease under the same load if the edge toughness increases. In order to understand more on the mechanisms, the following will analyze the effect of temperature on the cutting force. The edge toughness at different temperatures will be calculated. The effects of softening and toughening mechanisms on edge chipping will be discussed at different temperature ranges.

2.2.5.2.1 Softening Mechanism – Cutting Force

In the experiments, the dynamometer directly measures the x, y and z direction forces, which are radial (feed direction), tangential (cutting speed direction) and axial forces. Table 2.5 clearly demonstrates that laser heating is an effective method to reduce cutting force. When the

temperature at the cutting zone increases from 838 °C to 1349 °C, the average tangential force Fy decreases by 50% and the average radial force Fz decreases by 45%. When the temperature increases further, the force continues to decrease but with a reduced rate.

Table 2.5 Cutting Forces at Different Temperatures

Temperature °C	Radial force Fx (N)	Tangential force Fy (N)	Axial force Fz (N)	Resultant force (N)
838	47.7	94.2	227.0	250.4
1017	45.6	87.3	198.7	221.8
1172	42.2	62.6	96.0	122.1
1319	26.2	46.9	92	106.5
1349	23.4	38.3	88.0	98.8
1595	12.7	29.5	46.0	56.1

Figure 2.24 Average Cutting Forces and Temperature

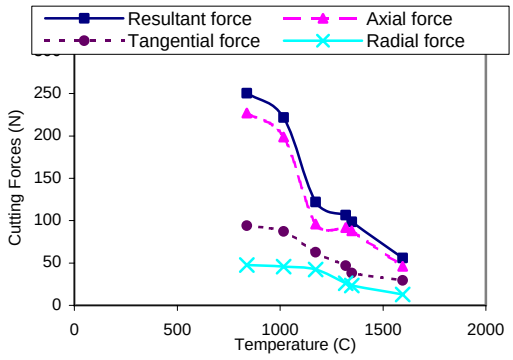

As shown in Figure 2.24, the relationship between cutting force and temperature is very similar with that of strength and temperature shown in Figure 2.19, indicating a close relation between cutting force and strength. Figure 2.24 and Table 2.5 show that when temperature

increases up to 1000°C, cutting force decreases steadily at a slow rate. When temperature is above the glassy transition temperature T_g, cutting force drops significantly at the temperature range between 1150 and 1200°C. But at the temperature range between 1200 to 1300 °C, cutting force decreases at a slower rate again. This could be related to the slight increase of strength in certain GPSSN around 1250 °C induced by the redistribution of the inherent defect of the material. When temperature is higher than 1350 °C, cutting force continues to decrease with rising temperature.

2.2.5.2.2 Toughening Mechanism – Edge Toughness

In indentation tests, the edge toughness is usually measured by a force perpendicular to the specimen surface. Quinn and Mohan (2005) investigated the changes in edge toughness when the forces are not perpendicular. It was found that larger force is required to produce a chip when the force is angled away from the edge. In the LAMill experiments of this study, the resultant force is angled toward the workpiece edge, which tends to lower the measured edge toughness. Edge toughness under different temperatures are calculated using equation (1). The load is the average resultant cutting force and flaking distance is the average edge chipping width. The calculated edge toughnesses are shown in Table 2.6.

The edge toughness at 838 °C is 452.2 N/mm. As discussed in Section 2.2.3.2, the GPSSN ceramics should have edge toughness around 580 N/mm at room temperature. However, under intensive and dynamic loads as in the laser assisted milling process, ceramics usually demonstrate much lower fracture and edge toughness than lab results. Also, the resultant cutting force which is angled toward the workpiece edge tends to lower the measured edge toughness than in indentation. In addition, the fracture and edge toughness of silicon nitride ceramics decrease steadily at a slow rate when temperature increases from room temperature to about 1000 °C. Therefore, the calculated edge toughness of 452.2 N/mm for the silicon nitride ceramic at 838 °C is very reasonable.

Figure 2.25 shows the relationship of edge toughness with temperature. The ‘S’ shape curve is very similar to the curve of fracture toughness shown in Figure 2.19. When temperature is lower than the transition range, edge toughness decreases slowly with rising temperature. When temperature increases to 1172°C, slightly above the glassy transition temperature, the edge toughness rapidly decreases to 284.5 N/mm, corresponding to the rapid softening of the

secondary glassy phases as shown in stage II of Figure 2.19. When temperature increases to 1319 °C, the edge toughness returns to the similar level before softening, indicating the start of the toughening mechanism. When temperature increases to 1349°C, edge toughness significantly increases to 798.2 N/mm, corresponding to the significant increase of the fracture toughness in stage III of Figure 2.19. There is no significant change in edge toughness when further increasing the temperature to 1595°C.

Table 2.6 Edge Toughness at Different Temperatures

Temperature (°C)	Average chipping width (mm)	Average resultant cutting force (N)	Edge Toughness (N/mm)
838	0.554	250.4	452.2
1017	0.515	221.8	430.6
1172	0.429	122.1	284.5
1319	0.230	106.5	463.1
1349	0.124	98. 8	798.2
1595	0.073	56.1	769.5

Figure 2.25 Edge Toughness and Temperature

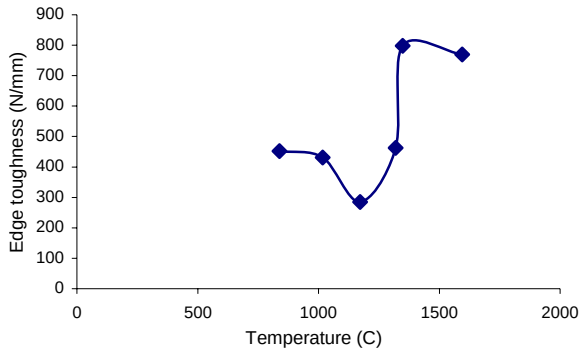

2.2.5.2.3 Coupled Effects of Softening and Toughening

Experimental results show that workpiece edge chipping is significantly reduced as temperature increases. Analysis of the cutting force and edge toughness demonstrates that there are two mechanisms responsible for the reduced edge chipping at elevated temperature. One is softening and the other is toughening. These two mechanisms take effect at different temperature ranges. In order to compare which mechanism dominates at which temperature range, the data of chipping width, cutting force and edge toughness are normalized by dividing the corresponding value at 838°C to include them in a same figure. Figure 2.26 shows the relationship of the normalized data with temperature.

Figure 2.26 Effects of Temperature

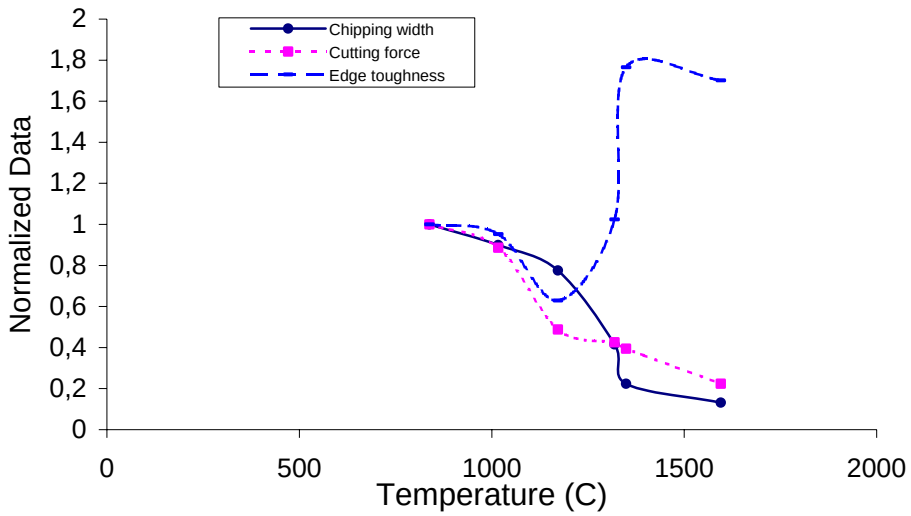

When temperature is lower than the glass transition temperature, edge chipping is reduced slowly through softening mechanism. But toughening mechanism has a slight negative effect on edge chipping since edge toughness decreases with temperature. Laser assisted machining of silicon nitride ceramics is not recommended at temperatures lower than the glass transition temperature due to the slow improvement on edge damage at this temperature range.

When the temperature is above the glass transition temperature and lower than the brittle to ductile transition (BDT) temperature, edge chipping continues to reduce at a slight rate. At this temperature range, both the cutting force and edge toughness decrease significantly. The decreased cutting force tends to reduce edge chipping while the decreased edge toughness tends to increase edge chipping. Since the positive effect of softening mechanism obviously overcomes the negative effect of toughening mechanism, the coupled effect is to reduce the edge chipping. Laser assisted machining is not recommended at this temperature range either since toughening mechanism does not take effect yet.

When the temperature is above the brittle to ductile transition and below the global softening temperature, edge chipping is significantly reduced through softening and toughening mechanisms. At this temperature range, both softening and toughening mechanisms have positive effects on edge chipping, while toughening has dominant effect. The edge toughness of

silicon nitride increases significantly and rapidly when temperature is above 1300°C. As shown in Table 2.6, the edge toughnesses increase from 463.1 N/mm to 798.2 N/mm when temperature increases from 1319 °C to 1349°C. This toughening mechanism significantly contributes to reduced edge chipping. At the same time, cutting force continues to decrease with temperature. Softening mechanism still helps to reduce edge chipping. This temperature range (above 1200°C) is the best choice for laser assisted machining in terms of reducing edge chipping. Especially when temperature is above 1300°C, edge toughness increases significantly with temperature. Toughening mechanism plays an important role to reduce edge chipping.

When the temperature is above the global softening point, the silicon nitride exhibits viscoplastic flow characteristic. Fracture toughness and edge toughness measurement becomes meaningless. Oxidation and microstructural change may happen for the whole structure. Rouxel [20] shows that a significant amount of eutectic liquid may form when temperature is above 1400°C and there is a smooth transition between the elastic behavior in the solid state and the viscous behavior in the liquid state when temperature increases from 1400°C to 1650°C. Experimental results in Table 2.6 shows that the calculated edge toughness almost doesn't change when temperature increases from 1349°C to 1595°C while the cutting force continues to decrease.

In summary, the temperature for laser assisted machining of silicon nitride ceramics should be higher than 1200°C to obtain good edge integrity. Temperature range between 1300 to 1400 °C has the most significant effect to reduce edge chipping since both the softening and toughening mechanisms work well at this temperature range. Further increasing the temperature could continue to improve the edge integrity, but at a reduced marginal return.

2.2.6 Conclusions

This study demonstrates that increased temperature in laser assisted machining can significantly reduce the workpiece edge chipping. When temperature is higher than 1000 °C, no macroscale entry edge chipping and interior edge chipping are observed. And the size of exit edge chipping decreases considerably as the temperature increases. The mechanisms of the elevated temperature on edge chipping include softening and toughening. When temperature increases, softening always helps to reduce edge chipping by reducing the cutting force, though the efficiency is different at different temperature range. But toughening mechanism will not take

effect until the temperature is well above the glassy phase transtion temperature. And the largest efficiency of toughening happens in a narrow temperature range between 1200 -1400°C. The coupled effects of softening and toughening shows that temperature range between 1200-1400°C has the most significant effect to reduce edge chipping in laser assisted machining.

2.2.7 Acknowledgement

Financial support of this work by the National Science Foundation under Grant No. DMI-0134579 is gratefully acknowledged.

2.2.8 References

Almond, E.A. and McCormick, N.J., 1986, "Constant geometry edge flaking of brittle materials", Nature, 321, 53-55.

Cao, Y., 2001, "Failure analysis of exit edges in ceramic machining using finite element analysis", Engineering Failure Analysis, Vol.8, 325-338.

Gogotsi, G.A., 2006, "Fracture resistance of ceramics: base diagram and R-line", Strength of Materials, Vol. 38, n. 3, 261-270.

Gogotsi, G.A.; Galenko, V.I. and Ozerskii, B.I., 2005, "Fracture resistance of ceramics: edge fracture method", Strength of Materials, Vol. 37, n.5, 499-505.

Gogotsi, G.A. and Mudrik, S.P., 2004, "Fracture resistance of ceramics upon edge chipping", Strength of Materials, Vol. 36, n. 5, 545-547.

Islam, M.U. and Campbell, G., 1993, "Laser machining of ceramics: a review", Materials and Manufacturing Processes, Vol. 8, n 6, 611-630.

König, W. and Zaboklicki, U., 1993, "Laser–assisted hot machining of ceramics and composite materials", Machining of Advanced Materials, NIST Special Publication 847, 455-463.

Kohler, N.; Ikuhara, Y.; Awaji, H. and K. Funatani, 1992, "High temperature fracture mechanism of gas-pressure sintered silicon nitride", Fracture Mechanics of Ceramics, Vol. 10, 367-377, edited by R.C. Bradt et al., Plenum Press, New York.

Lei, S.; Liu, W. and Deines, T., 2006, "A feasibility study on laser assisted milling of silicon nitride ceramic by integrating experimental study with FEA", Proceedings of 2006 NSF Design, Service, and Manufacturing Grantees and Research Conference, St. Louis, MO., USA.

Lei, S.; Shin, Y.C. and Incropera, F.P., 2001, "Experimental investigation of thermal-mechanical characteristics in laser-assisted machining of silicon nitride ceramics", Journal of Manufacturing Science and Engineering, Vol. 123, 639-646.

McCormick, N.J., 1982, "Edge flaking as a measure of material performance", Metals and Materials, Vol. 8, n3, 154.

McCormick, N.J. and Almond, E.A., 1990, "Edge flaking of brittle materials", Journal of Hard Materials, Vol.1, n1, 25-51.

Morrell, R., 2005, "Edge flaking – similarity between quasistatic indentation and impact mechanisms for brittle materials", Key Engineering Materials, Vol. 290, 14-22.

Morrell, R. and Gant, A.J., 2001, "Edge chipping of hard materials", International Journal of Refractory Metals & Hard Materials, Vol. 19, 293-301.

Ng, S.; Le, D.; Tucker, S. and Zhang, G., 1996, "Control of machining induced edge chipping on glass ceramics", American Society of Mechanical Engineers, Manufacturing Engineering Division, MED, v 4, International Symposium on Information Storage and Processing Systems, 229-236.

Ohbuchi, Y.; Matsuo, T. and Sakat, M., 1995, "Chipping in high-precision slot grinding of Mn-Zn ferrite", CIRP Annals - Manufacturing Technology, Vol. 44, n 1, 273-277.

Pei, Z.J., Khanna, N. and Ferreira, P.M., 1995, "Rotary ultrasonic machining of structural ceramics - a review", Ceramic Engineering and Science Proceedings, Vol. 16, n. 1, 259-278.

Petrofes, N. F. and Gadalla, A. M., 1988, "Electrical Discharge Machining of Advanced Ceramics", American Ceramic Society Bulletin, Vol. 67, n. 6, 1048-1052.

Quinn, J. and Mohan, R., 2005, "Geometry of edge chips formed at different angles", Ceramic Engineering and Science Proceedings, Vol 26, n 2, Mechanical Properties and Performance of Engineering Ceramics and Composites, A Collection of Papers Presented at the 29th International Conference on Advanced Ceramics and Composites, 85-92.

Quinn, J.; Su, L.; Flanders, L. and Lloyd, I., 2000, "Edge toughness and material properties related to the machining of dental ceramics", Machining Science and Technology, Vol. 4, n. 2, 291-304.

Rouxel, T., 2001, "High temperature mechanical behavior of silicon nitride ceramics", Journal of the Ceramic Society of Japan, Vol.109, n. 6, 89-97.

Scieszka, S.F., 2005, "Edge failure as a means of concurrently estimating the abrasion and edge fracture resistance of hard-metals", Tribology International, Vol.38, 834-842.

Yang, B.; Deines, T.; Geist, C. and Lei, S., 2007, "An experimental study of laser assisted milling of silicon nitride ceramic", Transactions of the North American Manufacturing Research Institution of SME, Vol. 35, 473-480.

CHAPTER 3 - Distinct Element Modeling of Machining Silicon Nitride Ceramics

Although extensive experimental studies have been conducted to understand the material removal mechanisms in machining of ceramics, there are still many questions regarding the micro-mechanisms of material removal based on the available experimental observations. This chapter will use distinct element method (DEM) to simulate the micro-mechanical behavior of machining silicon nitride ceramics. DEM models materials as arbitrarily sized particles bonded together. When the bonds break, cracks are formed or extended, which provides a direct method to treat the cracks during machining. The limitation of DEM is that it doesn't model plastic deformation. According to the experimental observations, there are some plastic deformation characteristics in LAM of silicon nitride ceramics. However, the material removal is mainly realized by brittle fractures both in conventional and LAM of silicon nitride ceramics. And the mechanical behavior of ceramics is controlled by the propagation of small cracks, including median cracks, lateral cracks and radial cracks. Therefore, DEM is a very promising method to model the material removal process in machining of silicon nitride ceramics since the plastic deformation in LAM, if any, is not a major material removal mechanism.

In order to successfully model the material removal of machining silicon nitride ceramics, creating a specimen that behaves like the real material is the first and very important step. Section 3.1 will first investigate the relationships between microparameters at particle level and macroproperties of the specimens that are modeled by bonded particles. Section 3.2 will use DEM to simulate the material removal process in conventional and laser assisted machining (LAM) of silicon nitride ceramics.

3.1 A Study on the Effects of Microparameters on Macroproperties for Specimens Created by Bonded Particles

Published in:

Engineering Computations: International Journal for Computer-Aided Engineering and Software, Vol. 23, No. 6, 2006, pp.607-631.

Author's Names:

Budong Yang, Yue Jiao and Shuting Lei

Author's Affiliation:

Department of Industrial and Manufacturing Systems Engineering, Kansas State University, Manhattan, KS 66506

3.1.1 Abstract

This section uses distinct element simulation with PFC2D (Itasca, 2002) to investigate the relationships between microparameters at particle level and macroproperties of the specimens that are modeled by bonded particles. Specifically, the effects of particle size, particle size ratio, particle contact modulus, contact stiffness ratio, friction coefficient, bond normal and shear strength on the properties of the specimens are investigated. It is shown that the Young's modulus of elasticity of the specimens is mainly determined by contact modulus and affected by the contact stiffness ratio and particle size. The Poisson's ratio of the specimens is mainly determined by contact stiffness ratio and slightly affected by particle size when particle size is large. The compressive strength of the specimens is mainly determined by bond normal strength or bond shear strength and greatly affected by friction coefficient. Quantitative relationships

between particle level parameters and mechanical properties of the bonded particle specimens are obtained.

Keywords: Distinct element method, Parallel-bonded particle model, Microparameters, Macroproperties, Numerical simulation.

3.1.2 Introduction

Since Cundall (1971) first proposed discrete element method (DEM) for geomechanics applications, the discrete element method has proven to be a very powerful and versatile numerical method to simulate the mechanical behavior of granular materials. Williams et al. (1985) further presented the theoretical basis for the discrete element method, which is capable of analyzing multiple, interacting, deformable, discontinuous or fractured bodies undergoing large motions. Subsequently, the interest in the use of the technique for a number of research and engineering applications increased rapidly (Dobry and Ng, 1992) and more sophisticated numerical models based on DEMs have been developed and used to solve a wide range of engineering problems. Cundall (1971) and Hocking (1978) used polygon-shaped particle based DEMs to analyze the mechanical behavior of blocky rock masses in mining engineering. Hocking (1992, 1993) applied DEMs to arctic engineering problems to determine the forces of ice on offshore structures and ships. Mustoe et al. (1992) developed a DEM for the coupled nonlinear analysis of deep ocean pipes and risers. Thornton (1992) applied DEM to solve engineering problems involving particle collisions. DePoorter et al. (1993) adapted DEM to analyze processing induced defects in advanced ceramics. O'Connor et al. (1997) used DEM to model the mechanics of sand production in oil recovery processes. Owen and Vaz (1999) combined finite and discrete element method to analyze the material failure in high-speed machining under adiabatic strain localization conditions. Kafui and Thornton (2000) presented numerical simulations of a spherical, crystalline agglomerate impacting a wall. The effects of bond strength and impact velocity on the wall force, kinetic energy of the agglomerate and the proportion of bonds broken were analyzed. Preece et al. (2001) simulated the rock blast with a three-dimensional DEM modeling.

DEMs with deferent particle shapes, such as superquadric DEM and ellipsoid DEM, have been developed to investigate the effects of particle shape and to analyze the problems involving continuous surface geometry (Rothenburg and Bathurst, 1991; Williams and Pentland, 1992;

Mustoe and Depoorter, 1993; Ting et al., 1993; Ng, 1994; Sawada and Pradham, 1994; Williams et al., 1995; Williams and O'Connor, 1995; Lin and Ng, 1997; Miyata et al., 2000; Mustoe et al., 2000; Mustoe and Miyata, 2001). Another way to investigate the effect of particle shape is using cluster-based DEMs, a simple adaptation of the original circular disk DEMs (Yamane et al., 1998; Yang and Lei, 2004; Itasca, 2002).

DEM modeling has become a powerful way to simulate granular material flows. There are many findings about granular flows and modeling of ball mills. (Campbell, 1990; Mishra and Rajamani, 1992, 1993; Cleary, 1998, 2000, 2001a&b; Mustoe and Miyata, 2001; Mishra and Thornton, 2002; Cleary and Laurent, 2002; Cleary et al., 2003). Mustoe and Miyata (2001) developed two DEMs for analyzing the material flow for systems of general-shaped bodies. One employed superquadric functions to define the shape of 2D particles and the other used ellipsoidal functions to model 3D particles. The authors demonstrated the applicability of the superquadric and ellipsoidal DEMs for the analysis of material flow problems. Cleary (2001b) extended previous ball mill modeling to a 10 m diameter mill and compared the simulation results with high-speed photographs of an experimental mill. Mishra and Thornton (2002) developed an elastic-perfectly plastic model in a DEM framework to simulate the motion and interaction of ball mills. The authors illustrated this contact model by simulating a 0.545 m diameter ball mill. These studies demonstrated that DEMs could produce accurate predictions for such industrial particle flow processes.

Oelfke et al. (1994) described an updated Lagrangian approach to extend the rigid block discrete element formulation by incorporating elastic block deformability. This formulation was implemented in the program developed by the U.S. Bureau of Mines for ground control problems in underground mines. Thorton and Zhang (2003) analyzed the direct shear test by numerical simulations using the discrete element method. Results were presented to show how the average shear to normal stress ratio acting on the shear band compares with the force data at the boundaries. Many studies successfully combined DEM with finite element method to analyze engineering problems (Munjiza et al., 1995, 1999a&b, 2004; Mohammadi et al., 1998; Munjiza and Andrews, 2000; Owen and Feng, 2001; Owen et al., 2002; Komodroms and Williams, 2002a&b; Han et al., 2002; Bangash and Munjiza, 2003). Some authors extended DEMs to 3D analysis (Lin and Ng, 1995, 1997; Preece et al., 2001; Thornton and Kafui, 2002; Sheng et al., 2002; Munjiza et al., 2003).

Discrete element methods have evolved to become a family of numerical simulation methods for simulating the dynamic and pseudostatic motions of a system of interacting bodies. The above-mentioned studies are only a small part of the available literatures. Most of the studies used computer simulations to verify the theoretical analysis. Many authors developed their own codes for DEM simulation. Others used commercial software to solve engineering problems. Recently, one of the most widely used DEM based commercial software is particle flow code (Itasca, 2002, 2003). The research-oriented distinct element codes in both two and three dimensions were developed by Itasca Consulting Group to meet the increased needs in research and engineering applications. Now PFC2D (Itasca, 2002) has been used in a wide range of engineering applications such as the simulation of rock cutting and indentation (Huang, 1999; Lei and Kaitkay, 2002; Kaitkay, 2002), underground rock support (Tannant and Wang, 2002) and laser assisted machining of ceramics (Lei, 2003; Yang and Lei, 2004). These studies showed that PFC2D appears to be an effective way to simulate the behaviors of brittle materials. However, an important aspect is still not fully understood, i.e., the relationship between parameters at the particle level, referred as microproperties hereafter, and properties of the specimens, referred hereafter as macroproperties. Huang (1999) made considerable efforts in investigating the scaling laws – relationships between microparameters and macroproperties of PFC2D specimens. For clarification, a PFC2D specimen is defined in this section as a bonded particle model of a material generated in PFC2D using parallel bonds. Potyondy and Cundall (2004) showed that a parallel-bonded model of Lac du Bonnet granite could reproduce many features of rock behavior including elasticity, fracturing, post-peak softening and strength increase with confinement. The authors also investigated the effects of particle size on macroproperties of parallel-bonded PFC2D specimens. However, because of the large number of microparameters involved in the specimen generation process, the relationship between microparameters and macroproperties of PFC2D specimens has not been fully studied (Huang, 1999; Lei, 2003). This section attempts to study the effects of microparameters on macroproperties of parallel-bonded PFC2D specimens and quantify their relationships. The macroproperties investigated are Young's modulus of elasticity, Poisson's ratio and compressive strength. First, the studies in micromechanical behaviors of DEM specimens are reviewed and insights from the literature are summarized. Then the microparameters in PFC2D specimen

generation procedure are discussed. Finally, numerical simulation results are analyzed and some quantitative correlations between the microparameters and the macroproperties are presented.

3.1.3 Literature Review on Theoretical Analysis of Microparameter-Macroproperty Relationships for Granular Assemblies

In a DEM model, the mechanical properties of a specimen depend on the microparameters defined at the particle level. Many people investigated the effective Young's modulus and Poisson's ratio for some special contact models. Some early studies, such as those by Duffy and Mindlin (1957), Deresiewicz (1958) and Walton (1978), studied the effective moduli of regular packing of spheres using Hertz-Mindlin contact model. These studies predicted that the effective elastic moduli are a function of the confining pressure. The results obtained in regular packing are very useful, but the material is not elastically isotropic. And the values of the effective elastic moduli were only considered under a few discrete values of porosity. Brandt (1955) considered random packing, but only studied the effective bulk modulus. The author used a Hertz-Mindlin contact model with random packing of spherical particles of different radii to model porous, granular rocks. It was demonstrated that the effective bulk modulus of an elastically isotropic, homogeneous porous rock is a function of the confining pressure, porosity and liquid saturation. Digby (1981) calculated the effective bulk and shear moduli of a porous granular rock modeled by a random packing of identical solid spherical particles, which were initially bonded together. Each particle was elastically isotropic. Neighboring particles were initially firmly bonded across small, flat, circular regions of the same average radius. The particle radius was small compared with the dimension of the specimen. Each particle had the same average number of contacts. The results showed that, under a Hertz-Mindlin contact law, the elastic moduli depend on the contact stiffness between particles, the average number of contacts, particle radius, and contact radius.

Some authors showed that, for random packing, the stress-strain relationship, and thus the effective modulus, could be derived based on a microstructural continuum approach (Walton, 1987; Bathurst and Rothenburg, 1988; Chang and Misra, 1989, 1990). Chang and Misra (1990) demonstrated that the elasticity tensor relating the stress and strain could take various forms depending on the symmetry of the mechanical properties of the granular material. And the material symmetry is closely related to the packing structure of the granular material. Using the

microstructural continuum method, Chang and Misra (1990) studied the relationship between the symmetry of mechanical properties and the packing structure for random granular packing. The packing structure was characterized by the distribution density functions that were represented by spherical harmonics expansion. For random packing of equal spheres with a linear contact law, the Young's modulus and Poisson's ratio were derived. The derived stiffness constants were shown to be functions of the particle size, specimen porosity, coordination number (the number of contacts per particle), interparticle contact stiffness, and parameters describing the distribution density function.

Theoretical analyses found in the literature have provided insights into the relationships between microparameters and macroproperties. First, it is shown that the macroproperties are mainly determined by the particle level parameters. The parameters related to the effective modulus and Poisson's ratio are:

- interparticle contact stiffness
- ratio of normal contact stiffness to tangential stiffness
- particle size
- porosity
- coordination number
- parameters describing the particle size distribution
- contact radius

Furthermore, the literature has shown that computer simulation is a powerful way to investigate the micromechanical behavior of granular assemblies. Most of the studies used computer simulations to verify the theoretical results. The simulations were conducted under the same contact models as the ones used in theoretical analyses. All of the numerical experiments fit well with the corresponding theoretical results. In fact, numerical experiments have become increasingly the preferred tool to investigate in detail the micromechanical behavior of materials. Just as Dobry and Ng (1992) pointed out: "From the viewpoint of the macroscopic stress-strain response of a material, and even of the modeling of actual engineering problems, numerical simulations are starting to challenge more traditional analytical and experimental methods".

Additionally, the models defined in PFC2D are far more complex than those that have been theoretically studied in the literature. Most of the results in the literatures were based on certain simplifications. Although some studies considered random packing, most of them only

considered identical particles. For those that did investigate different particle sizes, normally only two sizes, which were close to each other, were considered. Thus, the particles in the specimens were not truly randomly distributed. Some authors investigated specimens with particles bonded together, but the bonds were assumed to be permanent. However, in a PFC2D model, the bonds between particles can break and new contacts can form. The specimens are random packings with randomly distributed particles of different sizes. The bond strength is also randomly distributed. These models are much closer to real brittle materials, whose mechanical properties display significant variations due to the inherent microstructural inhomogeneities. However, for such models, it is too difficult to obtain a theoretical relationship between particle level parameters and mechanical properties of the specimens.

Numerical simulation provides an alternative way to investigate the micromechanical behavior of PFC2D specimens. Some insights in the micromechanical behavior of the specimen can be inferred from simulation results, and empirical quantitative relationships can be derived. Some work in this area has been reported in the literature. Dobry and NG (1992) developed a program CONBAL-2 based on TRUBAL written by Strack and Cundall to study the cyclic response of sand at both small and large strains. They proposed an empirical correlation for the shear modulus of the specimen and obtained the coefficients with the simulation data. The results captured the main features of actual uniform quartz sand response under cyclic loading and illustrated the potential of numerical simulation to serve as a general tool in the study of granular specimen behavior. Using numerical simulations, Huang (1999) studied the relationships between microparameters and macroproperties of contact-bonded PFC2D specimens. In this section, parallel-bonded specimens will be studied, and more microparameters will be investigated. We will discuss Huang's work further in Section 3.1.5.

3.1.4 Microparameters and Macroproperties of PFC2D Specimens

3.1.4.1 Microparameters of Parallel-Bonded PFC2D Specimens

PFC2D (Itasca, 2002) models the movement and interaction of circular particles by the distinct element method in two dimensions, which is a direct approach for simulating inelastic deformation and fracture of a material modeled as bonded particles. It allows finite displacements and rotations of discrete bodies, including complete detachment, and recognizes new contacts automatically as the calculation progresses.

In PFC2D, the interaction of the particles is treated as a dynamic process with states of equilibrium developing whenever the internal forces balance. It is assumed that velocities and accelerations of every particle are constant within each time-step. The time step is assumed to be so small that, during a single time step, disturbances cannot propagate from any particle further than its immediate neighbors. At the beginning of each time step, all the contacts are updated from the particle and wall positions. The force-displacement law is then applied to each contact to update the contact force based on the relative motion at the contact using the contact constitutive model. Then, the law of motion is applied to each particle to update its velocity and position based on the force and moment acting on the particle. The calculation cycle alternates between the application of the law of motion to the particles and the force-displacement law at the contacts.

The micromechanical behavior of a PFC2D specimen is defined at the particle level. How to generate a well connected, densely packed assembly, which behaves like the real material is the key to a successful simulation. In this section, the PFC2D specimens are generated using the specimen generation procedure described in the PFC2D manual. There are four steps: (1) generating a compact initial assembly, (2) installing specified isotropic stress, (3) eliminating floaters, and (4) finalizing specimen. For the detailed procedure, please refer to the manual of PFC2D (Itasca, 2002) or Potyondy and Cundall (2004). A set of microparameters are involved in the specimen generation. For a PFC2D specimen, there are two groups of microparameters. One consists of geometric and physical parameters which determine the dimension of the specimen, particle size and particle numbers. The other group contains constitutive parameters to define the contacts and bonds. There are three constitutive models to define contact behavior: a stiffness model, a slip model and a bonding model. For the Hertz and Mindlin contact model, various efforts have been reported in the literature to understand the stress-strain relationship of a regular assembly of discs (2D) or spheres (3D). As discussed in Section 3.1.2, the Young's modulus of a particle assembly is shown to be a function of the local normal and tangential stiffnesses and the Poisson's ratio is a function of the ratio of normal contact stiffness to tangential stiffness k_n / k_s. But little work has been done to investigate the effect of the microparameters on the strength (Huang 1999).

In this study, we used parallel bonds. There are three microparameters for particle-particle contact: the Young's modulus at each particle-particle contact, E_c, the ratio of particle normal to shear stiffness, k_n / k_s, and particle friction coefficient, μ. A parallel bond is defined by five parameters: normal and shear stiffness, $\bar{k}_n$ and $\bar{k}_s$, normal and shear strength, σ_b and τ_b, and bond radius, $\bar{R}$. The bond radius is set by defining $\bar{\lambda}$ such that $\bar{R}$ equal to $\bar{\lambda}$ times the smaller particle radius of the two particles in contact. As shown in Table 3.1, when we create a parallel-bonded PFC2D specimen, we input microparameters E_c and $\overline{E_c}$, not k_n and $\bar{k}_n$. For PFC2D, the quantitative relations between the stiffness and modulus of the contact are $k_n = 2tE_c$, where $t = 1$, and $k_s = \dfrac{k_n}{(k_n / k_s)}$. Values of the normal and shear stiffness of each parallel bond can be determined by $\bar{k}_n = \dfrac{\overline{E}_c}{R^{(A)} + R^{(B)}}$, where $R^{(A)}$ and $R^{(B)}$ are the particle radii, and $\bar{k}_s = \dfrac{\bar{k}_n}{(\bar{k}_n / \bar{k}_s)}$. For details please refer to Potyondy and Cundall (2004) or the manual of PFC2D (Itasca, 2002).

Table 3.1 Parameters for Specimen Generation

Group	Parameters	Symbol	Reference Set 1**	Reference Set 2***
Geometric and Physical Parameters	Specimen height (mm)	L	20	20
	Specimen width (mm)	W	10	10
	Minimum particle size (mm)	$R_{\min}$	0.135	0.135
	Particle size ratio,	$R_{\max} / R_{\min}$ *	2.0	2.0
	Particle density (kg/m^3)	ρ	3200	2650
	Particle contact modulus (GPa)	E_c	220	38
	Particle stiffness ratio	k_n / k_s	1.275	2.0
	Particle friction coefficient	μ	0.4	0.577

Constitutive Parameters	Parallel-bond radius multiplier	$\bar{\lambda}$	1	1
	Parallel-bond modulus (GPa)	$\overline{E_c}$	220	38
	Parallel-bond stiffness ratio	$\bar{k}_n / \bar{k}_s$	1.275	2.0
	Parallel-bond normal strength, mean (MPa)	$\sigma_{b,m}$	1600	46
	Parallel-bond normal strength, std. dev. (MPa)	$\sigma_{b,std}$	400	11.5
	Parallel-bond shear strength, mean (MPa)	$\tau_{b,m}$	3200	92
	Parallel-bond shear strength, std. dev. (MPa)	$\tau_{b,std}$	800	23

* $R_{\max}$ is the maximum particle size.

** Parameters of Reference Set 1 are used to model silicon nitride ceramics.

*** Parameters of Reference Set 2 are used to model Carthage limestone.

The overall modulus at a parallel-bonded contact is the sum of E_c and $\overline{E_c}$. We can estimate the macroscopic modulus of a parallel-bonded PFC2D specimen using the relation $E = \frac{E_c}{\xi} + \frac{\overline{E_c}}{\bar{\xi}}$, in which ξ and $\bar{\xi}$ are the ratios of micromodulus to macromodulus contribution for the particle-particle contacts and the parallel bonds, respectively, and E is the macroscopic modulus. If we always set $E_c = \overline{E_c}$ as in this section, then E is a function of E_c or $\overline{E_c}$.

The most important microparameters required to characterize a parallel-bonded PFC2D specimen are shown in Table 3.1. The parameters of Reference Set 1 and Reference Set 2 are selected to match silicon nitride ceramics (Si3N4) and Carthage limestone, respectively. When we investigate the effects of certain parameters, we use these values as reference, i.e., only the investigated parameters are changed but other parameters are kept the same as the reference values.

3.1.4.2 Macroproperties of Parallel-Bonded PFC2D Specimens

Since the behavior of the PFC2D specimen is defined only at the particle level through particle-particle contact models, a numerical biaxial test was conducted for each specimen to investigate the macroproperties. The procedure described in the PFC2D manual (Itasca, 2002) and Potyondy & Cundall (2004) was used to conduct the biaxial test. During the test, the specimen was loaded by moving the top and bottom platens at a specified velocity. The loading velocity must be low enough to ensure the specimen remains in quasi-static condition throughout the test, such that no inertial effects occur. In this section, the loading velocity of 0.05 m/s and a heavily damped (damping coefficient equal to 0.7) specimen were used to ensure a quasi-static status, which are confirmed by demonstrating that reducing the platen velocities does not change the measured macroproperties. During the test, the velocities of the lateral walls are controlled by a servo mechanism that maintains a specified confining stress (0.1 MPa). The normal stiffnesses of the lateral walls are set equal to a fraction (0.001) of the average particle normal stiffness to simulate a soft confinement. The normal stiffnesses of the top and bottom walls are set equal to the average particle normal stiffness.

The stress and strain are monitored during the simulation. The direct stresses are measured by dividing the average of the total force acting on opposing walls by the appropriate specimen dimension. The axial strain is measured by monitoring the motion of four particles lying at the centers of the four specimen edges. Use of such gauge particles removes the error introduced by ball-wall overlap when using the distances between opposing walls to compute strain. During the biaxial test, the deviatoric stress is calculated and the maximum value is recorded. For a bonded PFC2D specimen, this value will increase to some maximum and then decrease as the specimen fails, and the test is terminated when the deviatoric stress is smaller than 0.8 of its maximum value. After the biaxial test is completed, the stress-strain curve is obtained and the following properties are extracted: Young's modulus of elasticity, Poisson's ratio, and the compressive strength. The compressive strength is taken as the peak stress on a plot of axial stress versus axial strain. The elastic constants are calculated by the following procedure, using the stress and strain values between the start point and mid-point of the stress-strain curve. First, the Poisson's ratio and Young's modulus corresponding to a state of plane stress are computed by: $\nu' = -\frac{\Delta\varepsilon_x}{\Delta\varepsilon_y}$ and $E' = \frac{\Delta\sigma_y}{\Delta\varepsilon_y}$; then the elastic constants corresponding to a state of

plane strain are obtained via $\nu = -\dfrac{\nu'}{1+\nu'}$ and $E = E'(1-\nu^2)$. We use E' and ν', not E and ν, to match the properties of the real materials in this section.

3.1.5 Theoretical Relationships Between Microparameters and Macroproperties

Huang (1999) investigated the relationships between micro-scale parameters and macro-scale properties of contact-bonded PFC2D specimens by numerical simulations. It was assumed that prior to any bond failure, the set of parameters involved in the response of a contact-bonded PFC2D specimen are $\{k_n, k_s, R, n, \rho, L, V\}$, and that after a breakage of the contact bond, the controlling set of parameters become $\{k_n, k_s, \tau_{b,m}, \sigma_{b,m}, \mu, R, n, \rho, L, V\}$, where V is the loading speed, R is average particle size and the other parameters are the same as those defined in Table 3.1. The porosity n was chosen as a convenient measure of the particle size distribution. According to Buckingham π theorem, four independent dimensionless parameters govern the elastic response of the specimen $\left\{ k_s \big/ k_n, n, R \big/ L, V \big/ \sqrt{k_n / \rho} \right\}$. And the failure of the specimen is governed by $\left\{ \dfrac{k_n R}{\sigma_{b,m}}, \dfrac{\tau_{b,m}}{\sigma_{b,m}}, \mu, \dfrac{k_s}{k_n}, n, \dfrac{R}{L}, \dfrac{V}{\sqrt{k_n / \rho}} \right\}$. Because the numerical simulations were performed under quasi-static loading, $V \big/ \sqrt{k_n / \rho}$ could be dropped from the list. Huang (1999) further assumed that particle size R/L was so small that its effects could be ignored. Thus, the following relationships could be established.

$$E = k_n \Phi_E \left(\frac{k_s}{k_n}, n \right) \tag{1}$$

$$\nu = \Phi_\nu \left(\frac{k_s}{k_n}, n \right) \tag{2}$$

$$\sigma_c = \sigma_{b,m} \Phi_c \left(\frac{k_n R}{\sigma_{b,m}}, \frac{\tau_{b,m}}{\sigma_{b,m}}, \mu, \frac{k_s}{k_n}, n \right) \tag{3}$$

However, the porosity n may not be a good index to represent the particle size distribution. In fact, for a granular assembly, the porosity is closely related to the coordination

number, which is defined as the number of contact points per particle. Oda et al. (1982) and Shahinpoor (1983) presented the relationship between the average coordination number and the porosity of the packing. It was shown that the relationship between porosity and the coordination number was independent of particle size distribution. Moreover, in PFC2D, the porosity n generated for a randomly and closely packed two-dimensional specimen with circular particles (actually cylinders with unit length) and randomly distributed particle size is approximately 16%. This porosity is independent of particle size. Thus, it seems reasonable to drop porosity n from the above functions and use another parameter to measure particle size distribution. In fact, PFC2D specimens are randomly packed particles with randomly distributed particle sizes in the specified range of $[R_{\min}, R_{\max}]$, where $R_{\min}$ and $R_{\max}$ are the minimum and maximum particle radius, respectively. To analyze the effect of particle size distribution on the behavior of a PFC2D specimen, we add the particle size ratio of $R_{\max} / R_{\min}$ into the set of parameters and investigate the effects of $R_{\max} / R_{\min}$ on the macroproperties of the specimen.

Another issue concerns the effect of particle size on the behavior of PFC2D specimens. Even though it can be argued that the effects of particle size will diminish when the particle size becomes small, the effects of particle size deserve investigation. Based on our study, when particle size is relatively large ($L / R < 80$), the behavior of the specimens will be greatly affected by the particle size. Usually particle size cannot be chosen too small because of the computational limitations. Furthermore, when cracks are considered, which are represented by breakage of particle bonds, particle size will affect the crack propagation. Specifically to say, when a bond breaks, the crack grows one particle size. To form a same size crack, more bonds need to be broken in specimens with small particle size. Potyondy and Cundall (2004) showed that the notch-formation process was sensitive to the particle size and there were more cracks formed in specimen with smaller particles, meaning more bonds were broken. In the simulation of laser assisted machining of silicon nitride ceramics using PFC2D, Lei (2003) noted that the width of the force spikes appeared to be related to the range of the particle size. Kaitkay (2002) discussed the effects of minimum particle size on the cutting force for rock cutting and observed that the variation in cutting forces was as high as 30%. These researchers showed that particle size appeared to have effects on the behaviors of PFC2D specimens.

For a parallel-bonded PFC2D specimen, there are more microparameters involved in the controlling set. The parallel-bond modulus $\overline{E}_c$ and parallel-bond stiffness ratio $\overline{k}_n / \overline{k}_s$ are two important microparameters that would affect the behavior of PFC2D specimens. In order to simplify the equation, we keep E_c equal to $\overline{E}_c$ and k_n / k_s equal to $\overline{k}_n / \overline{k}_s$ for all specimens. To do so, we can treat the parameters E_c and $\overline{E}_c$ as one parameter, k_n / k_s and $\overline{k}_n / \overline{k}_s$ as one. In practice, many authors used same values for these two pairs of parameters to generate PFC2D specimens (Potyondy and Cundall, 2004; Lei, 2003; Yang and Lei, 2004; Kaitkay, 2002). Potyondy and Cundall (2004) set E_c equal to $\overline{E}_c$, and k_n / k_s equal to $\overline{k}_n / \overline{k}_s$ when they created parallel-bonded specimens to simulate rock behaviors. These specimens reproduced most of the features of rock behavior. Yang and Lei (2004) also set the same values for these two group parameters to simulate machining of silicon nitride ceramics. The simulation results showed that parallel-bonded PFC2D specimens with E_c equal to $\overline{E}_c$, and k_n / k_s equal to $\overline{k}_n / \overline{k}_s$ could match the properties of silicon nitride quite well and thus described the material removal mechanism in silicon nitride machining. Other authors (Lei, 2003; Lei and Kaitkay, 2002; Kaitkay, 2002) also used same values for these two pairs of parameters when creating parallel-bonded PFC2D specimens. In this section, we only consider the case of $E_c = \overline{E_c}$ and $k_n / k_s = \overline{k}_n / \overline{k}_s$. Hence only E and k_n / k_s are included in the equations we propose later.

According to the specimen generation procedure described in PFC2D, the input microparameter for a parallel-bonded specimen is particle contact modulus E_c, not particle contact stiffness k_n, therefore, we use E_c as the scaling parameter for Young's modulus instead of k_n. In fact, k_n is directly determined by the input parameter E_c as described in Section 3.1.3. Because the input microparameter in PFC2D model is k_n / k_s, we change the parameter k_s / k_n in equations (1) – (3) to k_n / k_s.

Thus, we propose the following correlations that are modified based on Equations (1) to (3), which include the parameters L / R and $R_{\max} / R_{\min}$ in the function and eliminate the porosity n.

$$E = E_c \Phi_E \left(\frac{k_n}{k_s}, \frac{L}{R}, \frac{R_{\max}}{R_{\min}} \right) \tag{4}$$

$$\nu = \Phi_{\nu}\left(\frac{k_n}{k_s}, \frac{L}{R}, \frac{R_{\max}}{R_{\min}}\right) \tag{5}$$

$$\sigma_c = \sigma_{b,m}\Phi_c\left(\frac{E_c}{\sigma_{b,m}}, \frac{\tau_{b,m}}{\sigma_{b,m}}, \mu, \frac{k_n}{k_s}, \frac{L}{R}, \frac{R_{\max}}{R_{\min}}\right) \tag{6}$$

3.1.6 Effects of Individual Microparameters on Macroproperties

Now we investigate the effects of each individual parameter in Equations (4) to (6) on the macroproperties. If the parameter turns out to have little effects on the macroproperty, it will be dropped out of the function. The parameters with obvious effects will be further investigated to study their interdependencies. Because the microparameters involved in Young's modulus and Poisson's ratio are the same, but are quite different from those in compressive strength, we will first discuss the effects of the parameters on Young's modulus and Poisson's ratio together and then the effects on compressive strength.

3.1.6.1 Effects of Individual Microparameters on Young's Modulus and Poisson's Ratio

When we investigate the effects of individual microparameters, all those microparameters except the investigated one are chosen to be the same as those in Reference Set 1. Then the investigated parameter is changed and the effects on the macroproperties are studied.

3.1.6.1.1 The Effects of Particle Size L/R

Theoretical analysis has shown that particle size affects the micromechanical behavior of a specimen. As we have discussed, both Lei (2003) and Kaitkay (2002) observed the effect of particle size on machining process. But the authors did not discuss the effect of particle size on mechanical properties of the specimens. Huang (1999) used the ratio L/R as a measure of the degree of discretization and discussed its effects on sample preparation. It was shown that the effect of the discretization on the macro-scale material strength could be ignored when the ratio of L/R was in the chosen range. The author tested four ratios of L/R = 120, 140, 160 and 180 with the same average radius R =1.25 mm and particle size distribution of R_{dev}/R=0.2, where R_{dev} is the deviation of the maximum radius from the mean radius R. In order to consider the statistical effect, each specimen was tested 10 times. The results revealed that the mean uniaxial strengths were not greatly affected within the chosen range of L/R. Potyondy and Cundall

(2004) investigated the effects of particle size on macroproperties of parallel-bonded PFC2D specimens when modeling Lac du Bonnet granite. The results showed that the Poisson's ratio appeared to be independent of particle size and Young's modulus increased slightly (less than 5%) as particle size decreased. Compressive strength also appeared to be independent of the chosen particle size. The mean values differed by less than 8% and exhibited no clear increasing or decreasing trend when particle size decreased.

However, the effects of L/R on the macroproperties of a PFC2D specimen are not fully understood. Huang (1999) investigated the effect of a narrow range of L/R (120-180) on compressive strength for contact-bonded specimens. Potyondy and Cundall (2004) studied a large range of L/R (44-352) for parallel-bonded specimens which model crystalline rocks. In this research, using parallel-bonded specimens, the effects of a wide range of L/R (20-260) are investigated and quite different materials are studied. Besides compressive strength, Young's modulus and Poisson's ratio are also considered.

To observe the effects of random particle distributions, selected specimens were tested 20 times by changing the seed for the random number generator. The L/R of these selected specimens are chosen to be 40, 60, 80, 100, and 217. Then the standard deviations of the macroproperties are calculated, which are represented in the figures by the error bars on the mean values. Other specimens are tested only once and the results are shown by the black dots in the figures. The effects of L/R on the Young's modulus and Poisson's ratio of the specimens are shown in Figure 3.1 and 3.2.

Figure 3.1 Effect of L/R on Young's Modulus of Elasticity

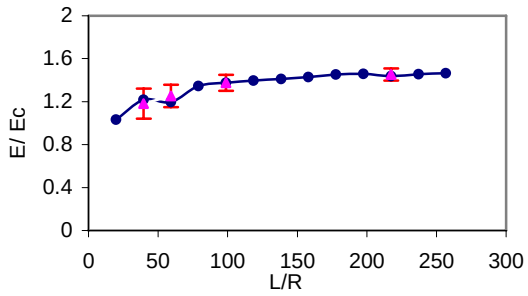

Figure 3.2 Effect of L/R on Poisson's Ratio

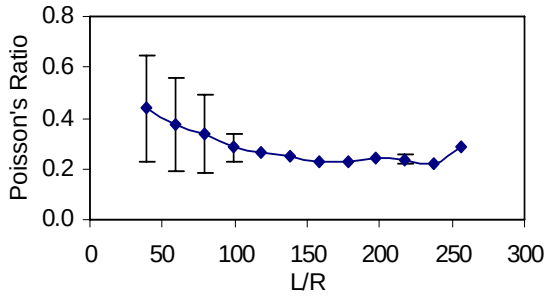

As L/R increases, the Young's modulus tends to increase. For small particle size (L/R>130), the Young's modulus varies little for different particle sizes. But for large particle sizes (L/R<80), the Young's modulus changes significantly. As L/R increases, the variances of Young's modulus decreases (see the four error bars for the selected specimens), which means that the effect of the random distribution of particles on Young's modulus is small for small particle sizes. Overall, the relationship between L/R and the Young's modulus can be approximated by a logarithmic curve. After regression analysis, the relationship can be approximated by $E/Ec = 0.17\ln(L/R) + 0.57$, with R^2=0.935.

As L/R increases, the Poisson's ratio tends to decrease as shown in Figure 3.2. When L/R is large enough (such as ≥ 100), the Poisson's ratio appears to be independent of particle size. However, evidenced by the error bars, the variations for L/R ≤ 80 are so large that the coefficient of variation (ratio of standard deviation to mean) are close to 50%. Therefore, we argue that it is not advisable to use those data to form a relation between Poisson's ratio and L/R. Instead, it is suggested that a large L/R be used when creating specimens using PFC2D.

As shown by the error bars in Figure 3.1 or Figure 3.2 for the selected specimens, the random distribution of particles has a similar effect on both Poisson's ratio and Young's modulus. As particle size increases, the effect of the random distribution of particles increases. So, particle size has very significant effects on the Young's modulus and Poisson's ratio. That means even for specimens with the same microparameters, the Young's modulus and Poisson's ratio can be quite different. In order to treat this variation, when we consider the combined effects of the parameters, each specimen is tested for 10 times and the average values are used to analyze the relationship between microparameters and macroproperties.

3.1.6.1.2 The Effects of Particle Ratio

When the ratio of maximum to minimum particle size varies, the average particle size and the particle size distribution will also change. In order to eliminate the effects of particle size, the dimension of the specimen L is also changed to keep the relative particle size L/R the same. Four selected particle ratios of 2, 2.4, 4.2 and 6.2 are tested 20 times to observe the effect of the random distribution of particles. The effects of the randomness (variances of the results) are shown by the error bars in Figs. 3.3 and 3.4. Other specimens are tested only once as shown by the black dots in the figures. The effects of particle ratio are shown in Figures 3.3 and 3.4.

Particle ratio has no obvious effects on the Young's modulus and Poisson's ratio of the specimens, although large fluctuations are noticed for Poisson's ratio. Even for a large particle ratio, the particle distribution will not increase the variation of Young's modulus and Poisson's ratio. It seems that the particle ratio can be dropped out of Equations (4) and (5).

Figure 3.3 Effect of Particle Ratio on Young's Modulus of Elasticity

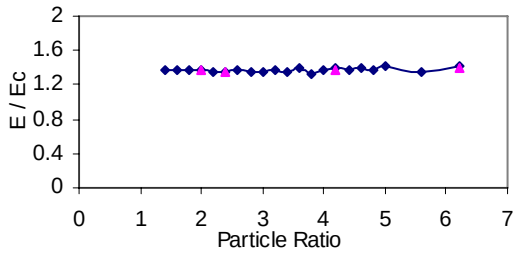

Figure 3.4 Effect of Particle Ratio on Poisson's Ratio

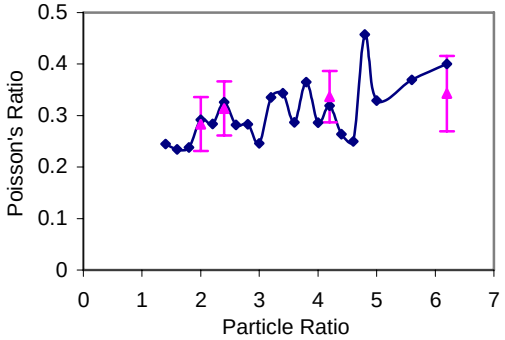

3.1.6.1.3 The Effects of Particle Contact Modulus

As shown in Figure 3.5, the Young's modulus is linearly related to particle contact modulus E_c, similar to the theoretical prediction for randomly packed specimens with identical particle sizes (Chang and Misra, 1990). The relationship between E_c and Young's modulus can be fitted by an equation $E = 0.60E_c + 165.12$ with R^2=0.983.

Particle contact modulus E_c (therefore particle contact stiffness k_n) seems to have little effect on Poisson's ratio, as shown in Figure 3.6. The fluctuations of Poisson's ratio for different E_c are caused by the particle distribution of the specimens. This result is also predicted by the theoretic analysis for randomly packings with identical particle sizes (Walton, 1987, Chang and Misra, 1990).

Figure 3.5 Effect of E_c on Young's Modulus of Elasticity

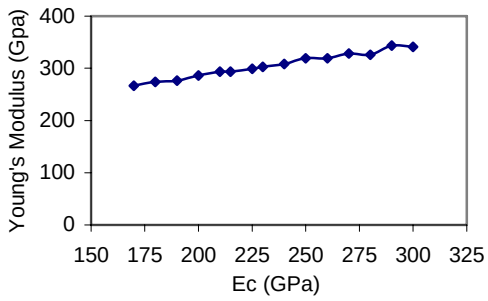

Figure 3.6 Effect of E_c on Poisson's Ratio

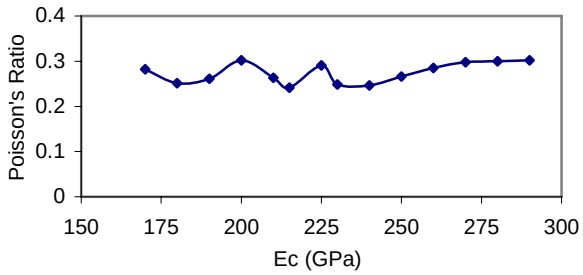

3.1.6.1.3 The Effects of k_n / k_s

Figure 3.7 and 3.8 show that the effects of k_n / k_s on Young's modulus and Poisson's ratio are very obvious. As k_n / k_s increases, the scaled Young's modulus of a parallel-bonded PFC2D specimen decreases. However, when k_n / k_s is large enough (>4), the scaled Young's modulus is mainly determined by E_c. The effect of k_n / k_s on Young's modulus can be described by $E/E_c = -0.30 \ln k_n/k_s + 1.42$ with R^2=0.989. The Poisson's ratio increases as k_n / k_s increases, although it is not as smooth as the scaled Young's modulus. The relationship between Poisson's ratio and k_n / k_s can be approximated by $\nu = 0.122 \ln k_n/k_s + 0.22$ with R^2=0.869.

Figure 3.7 Effect of k_n / k_s on Young's Modulus of Elasticity

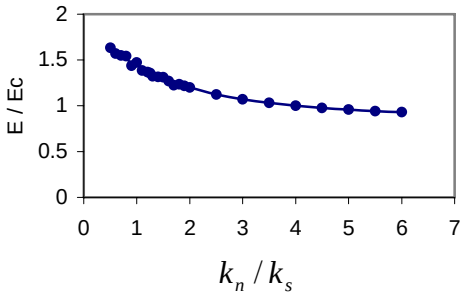

Figure 3.8 Effect of k_n / k_s on Poisson's Ratio

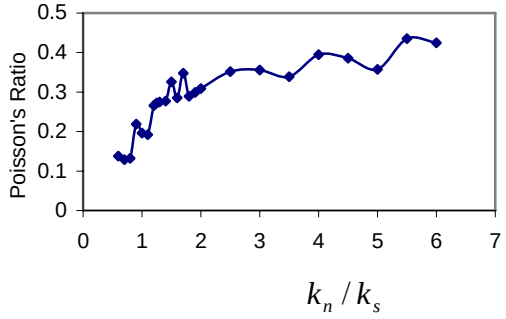

Now, we can see that the Young's modulus of a parallel-bonded PFC2D specimen is mainly determined by the particle contact modulus E_c and affected by the relative particle size L/R and the stiffness ratio k_n/k_s. The relationship between Young's modulus and E_c is linear. The effects of L/R and k_n/k_s are logarithmic. The Poisson's ratio of a parallel-bonded PFC2D specimen is mainly determined by k_n/k_s for sufficiently large values of L/R as recommended in Section 3.1.5.1.1. Particle size ratio has no significant effects on Young's modulus and Poisson's ratio. Therefore, according to the simulation results, the Young's modulus and Poisson's ratio can be expressed in the following correlations:

$$E = E_c \Phi_E \left(\frac{k_n}{k_s}, \frac{L}{R} \right) \tag{7}$$

$$\nu = \Phi_\nu \left(\frac{k_n}{k_s} \right) \tag{8}$$

3.1.6.2 Effects of Individual Microparameters on Compressive Strength

Now we consider the effects of the individual parameters on the compressive strength. According to Equation (6), the parameters that should be investigated include relative particle size L/R, particle size ratio $R_{\max}/R_{\min}$, particle friction coefficient μ, particle contact modulus E_c, contact stiffness ratio k_n/k_s, and bond strength ratio $\tau_{b,m}/\sigma_{b,m}$. The effects of these parameters on compressive strength are shown in Figures 3.9 to 3.14.

Figure 3.9 Effect of L/R on Compressive Strength

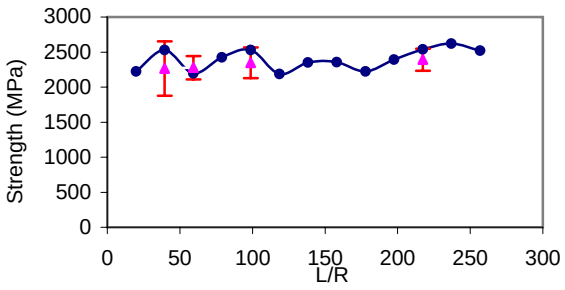

Figure 3.10 Effect of Particle Ratio on Compressive Strength

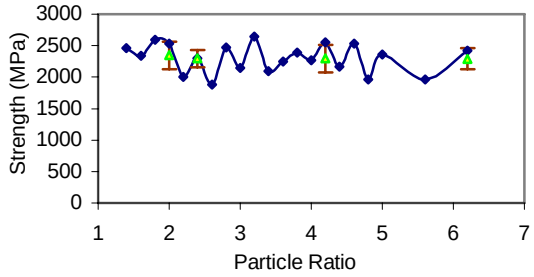

Figure 3.11 Effect of E_c on Compressive Strength

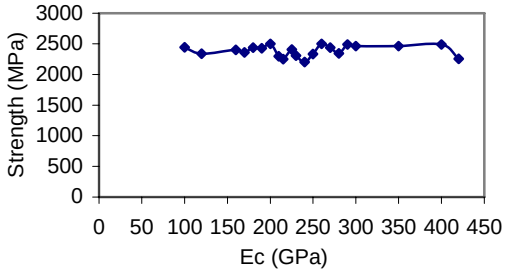

Figure 3.12 Effect of k_n / k_s on Compressive Strength

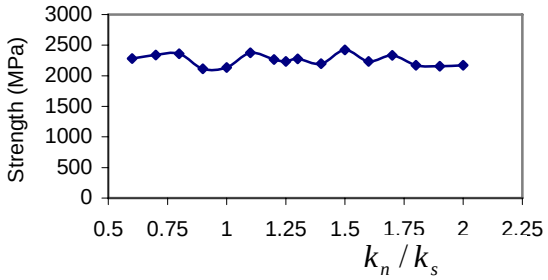

Figure 3.13 Effect of $\tau_{b,m}/\sigma_{b,m}$ on Compressive Strength

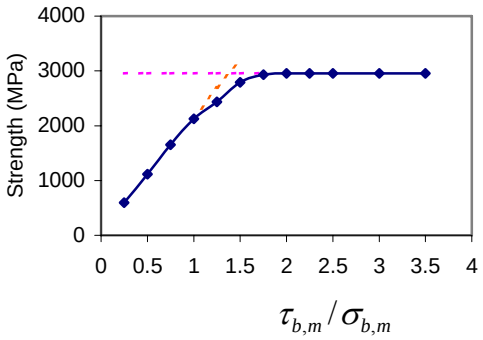

Figure 3.14 Effect of Friction Coefficient on Compressive Strength

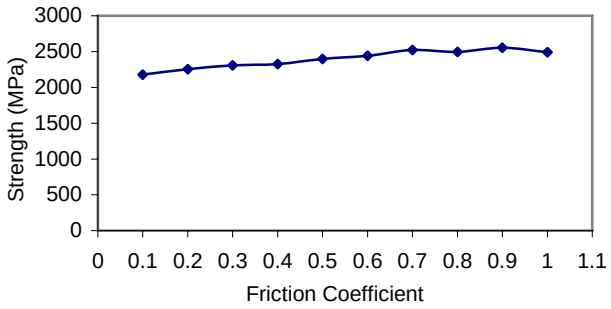

It is shown in Figure 3.9 that particle size L/R has no significant effect on the compressive strength. L/R varies from 20 to more than 250, but the compressive strength changes very little. The variation of compressive strength in Figure 3.9 is caused mainly by the random particle distribution in the specimens. And as L/R increases, the effect of randomness seems to decrease. As shown by the error bars in Figure 3.9, when L/R increases, the strength variation decreases.

Figures 3.10, 3.11 and 3.12 show that particle ratio $R_{\max}/R_{\min}$, contact modulus E_c and contact stiffness ratio k_n/k_s also have little effects on the compressive strength. Thus, it is reasonable to argue that the dependency of compressive strength on these parameters is weak. Similar results were reached by Huang (1999).

Figure 3.13 and 3.14 show that compressive strength is mainly determined by bond strength $\sigma_{b,m}$ or $\tau_{b,m}$ and affected by friction coefficient μ. The effect of friction coefficient μ on compressive strength can be fitted by a logarithmic relationship: $\sigma_b = 164.51 \ln \mu + 2527.20$ with R^2=0.926. However, the relationship between the compressive strength of the specimen and the bond strength between the particles is more complex. When $\tau_{b,m} / \sigma_{b,m}$ is small (less than 1), the compressive strength is mainly determined by bond shear strength $\tau_{b,m}$, which means that compressive strength increases linearly with the bond shear strength but is independent of $\sigma_{b,m}$. In this case, because the bond shear strength is smaller than the bond normal strength, most of the bonds break in shear. So, when $\tau_{b,m} / \sigma_{b,m}$<1, compressive strength should be scaled on shear bond strength. When 1<$\tau_{b,m} / \sigma_{b,m}$<2, both normal and shear failures occur at the particle bonds. As bond shear strength $\tau_{b,m}$ increases, the compressive strength also increases, but not as fast. Still, compressive strength can be scaled on bond shear strength in this situation. When $\tau_{b,m} / \sigma_{b,m}$ >2, the compressive strength is mainly determined by bond normal strength $\sigma_{b,m}$. In the micro-scale level, the bonds tend to fail in tension. Thus, the scaling parameter for compressive strength should be chosen as bond normal strength $\sigma_{b,m}$.

Thus, Equation (6) can be reduced to:

$$\sigma_c = \begin{cases} \tau_{b,m} \Phi_c \left(\dfrac{\tau_{b,m}}{\sigma_{b,m}}, \mu \right) & 0 < \dfrac{\tau_{b,m}}{\sigma_{b,m}} < 2 \\ \sigma_{b,m} \Phi_c \left(\dfrac{\tau_{b,m}}{\sigma_{b,m}}, \mu \right) & \dfrac{\tau_{b,m}}{\sigma_{b,m}} > 2 \end{cases} \tag{9}$$

3.1.7 Combined Effects of Microparameters on Macroproperties

Equations (7) and (8) show that Young's modulus and Poisson's ratio are functions of particle contact stiffness ratio and particle size. Equation (9) shows that bond shear to normal strength ratio $\tau_{b,m} / \sigma_{b,m}$ and particle friction coefficient μ greatly affect the compressive

strength. Next, we change these microparameters simultaneously and investigate their combined effects on the macroproperties.

In order to obtain a more general relationship so that it can be applied to a large range of different materials, two different materials are used as examples. One is Carthage limestone with relatively low Young's modulus and low strength. The other is silicon nitride (Si3N4) ceramics with relatively high Young's modulus and high strength. Except for the parameters whose effects are investigated, the microparameters of the specimens for Carthage limestone are set as those in Reference Set 2 and those for Si3N4 are chosen from Reference Set 1.

3.1.7.1 Combined Effects of k_n / k_s and L / R on Young's Modulus and Poisson's Ratio

The value of k_n / k_s and L / R are changed at the same time to observe the combined effects of these two parameters on Young's modulus and Poisson's ratio.

Figure 3.15 Combined Effects of k_n / k_s and L / R on Young's Modulus of Carthage Limestone

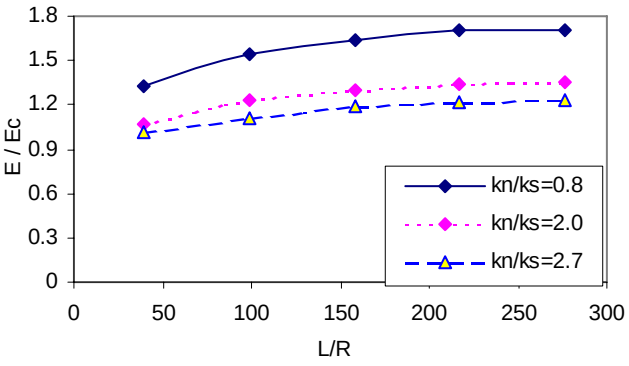

Figure 3.16 Combined Effects of k_n / k_s and L / R on Young's Modulus of Si_3N_4

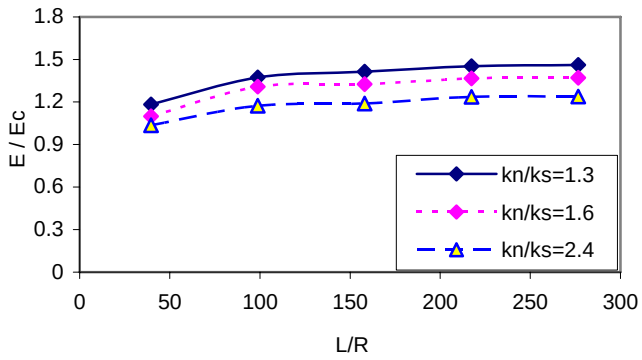

As shown in Figures 3.15 and 3.16, the results of the combined effects of k_n / k_s and L / R on the properties are very similar for these two types of specimens. Both k_n / k_s and L / R have very stable effects on Yong's modulus. It seems that the effects of k_n / k_s and L / R on Young's modulus are independent of each other. The following correlations are obtained for rock and ceramics specimens, respectively, based on the results:

$$E/E_c = 0.74 + 0.16 \ln L/R - 0.35 \ln k_n/k_s \quad \text{with } R^2 = 0.983. \tag{10}$$

$$E/E_c = 0.82 + 0.13 \ln L/R - 0.33 \ln k_n/k_s \quad \text{with } R^2 = 0.955. \tag{11}$$

It can be seen that the coefficients of the two equations are very close. Therefore, for these two materials, a general relationship can be obtained by averaging the corresponding coefficients in the two Equations.

$$E/E_c = 0.78 + 0.14 \ln L/R - 0.34 \ln k_n/k_s \tag{12}$$

As shown in Figures 3.17 and 3.18, when L / R is large enough (such as L/R ≥ 100), the particle size seems to have no significant effects on Poisson's ratio for both materials. Here the data for L/R < 100 are not plotted because the large variations associated with the values as observed in Section 3.1.5.1.1. It should be noted that, for rock specimens, the Poisson's ratio was found to be more predictable when L / R is smaller than 100, i.e., the variations are smaller for rock specimens than for ceramic specimens. And the mean values for rock specimen seem to be independent of L/R even when L/R is small. Potyondy and Cundall (2004) also reached this result for rock specimens. At this moment, it is not clear why the effect of L / R on Poisson's ratio of parallel-bonded PFC2D ceramic specimens is different from that of rock specimens when L/R is small. One way to avoid this problem though is to select a large enough value of L / R. If L / R is selected to be larger than 100, the Poisson's ratio seems to be independent of L / R for these two materials. Therefore, Poisson's ratios of parallel-bonded PFC2D specimens for different materials can be related to k_n / k_s. And this relationship can be expressed as:

$$\nu = 0.14 + 0.20 \ln k_n / k_s \qquad (13)$$

Figure 3.17 Combined Effects of k_n / k_s and L / R on Poisson's Ratio of Carthage limestone

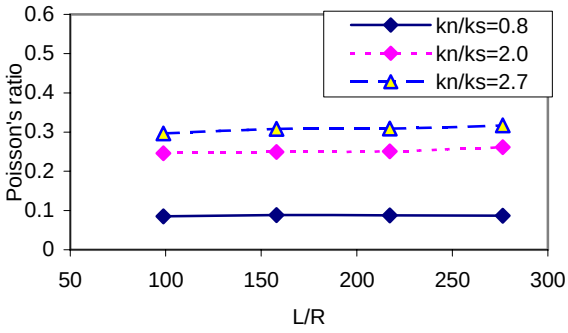

Figure 3.18 Combined Effects of k_n / k_s and L / R on Poisson's Ratio of Si_3N_4

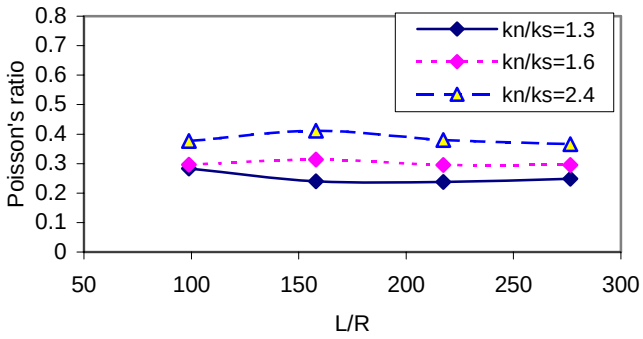

3.1.7.2 Combined Effects of $\tau_{b,m} / \sigma_{b,m}$ and μ on Compressive Strength

According to Equation (9), the parameters that need to be investigated are $\tau_{b,m} / \sigma_{b,m}$ and μ. For $0 < \tau_{b,m} / \sigma_{b,m} < 2$, the compressive strength of the specimen is mainly dependent on $\tau_{b,m}$. For $\tau_{b,m} / \sigma_{b,m} > 2$, the compressive strength of the specimen is mainly dependent on $\sigma_{b,m}$. First we change $\tau_{b,m}$ but keep $\sigma_{b,m}$ the same to observe the combined effects of $\tau_{b,m} / \sigma_{b,m}$ and μ on

compressive strength for 0< $\tau_{b,m}/\sigma_{b,m}$ <2. Then $\sigma_{b,m}$ is changed but $\tau_{b,m}$ is kept the same to observe the combined effects of $\tau_{b,m}/\sigma_{b,m}$ and μ for $\tau_{b,m}/\sigma_{b,m}$ >2. The results are shown in Figures 3.19 and 3.20.

Figure 3.19 Combined Effects of $\tau_{b,m}/\sigma_{b,m}$ and μ on compressive strength

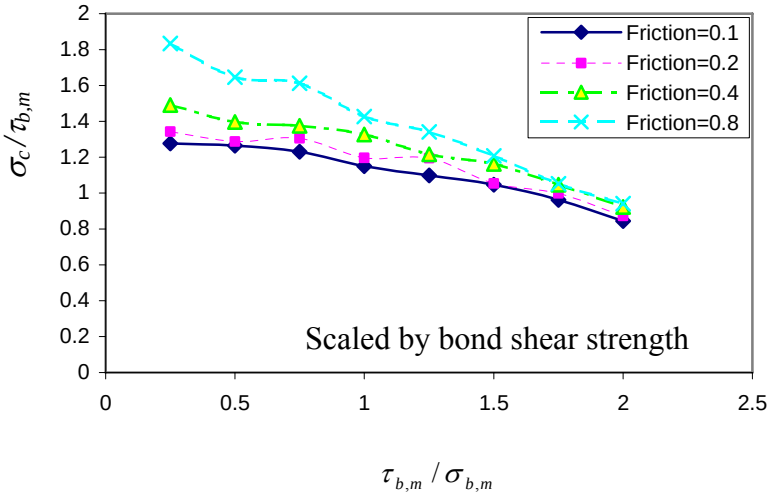

Figure 3.19 shows that the scaled compressive strength $\sigma_c/\tau_{b,m}$ decreases as $\tau_{b,m}/\sigma_{b,m}$ increases. When $\tau_{b,m}/\sigma_{b,m}$ is small, the effect of μ on the scaled compressive strength is obvious: when μ increases, the scaled compressive strength increases. However, when $\tau_{b,m}/\sigma_{b,m}$ becomes large, the effect of μ interacts with the effect of $\tau_{b,m}/\sigma_{b,m}$, which means that $\tau_{b,m}/\sigma_{b,m}$ and μ have interdependency on the compressive strength.

When the compressive strength is related to the parameters $\tau_{b,m}/\sigma_{b,m}$ and μ, the interaction is considered by introducing a nonlinear term in the equation. The relationship is given as follows.

$$\sigma_c/\tau_{b,m} = 2.11 + 0.38\ln\mu - 0.63\frac{\tau_{b,m}}{\sigma_{b,m}} - 0.22\frac{\tau_{b,m}}{\sigma_{b,m}}\ln\mu \quad \text{with } R^2=0.959 \qquad (14)$$

For $\tau_{b,m}/\sigma_{b,m}$>2, the compressive strength mainly depends on bond normal strength $\sigma_{b,m}$. The scaled parameter can be chosen to be $\sigma_{b,m}$. In order to observe the effect of $\sigma_{b,m}$ on compressive strength, $\sigma_{b,m}$ is changed while $\tau_{b,m}$ keeps the same. It is shown that scaled compressive strength $\sigma_c/\sigma_{b,m}$ keeps the same when $\tau_{b,m}/\sigma_{b,m}$>2. But for different particle friction efficient μ, the values of $\sigma_c/\sigma_{b,m}$ are slightly different. However, for a large range of friction coefficient (0.1~0.8), $\sigma_c/\sigma_{b,m}$ only changes from 1.69 to 1.88, or by approximately 11%.

Figure 3.20 Combined Effects of $\tau_{b,m}/\sigma_{b,m}$ and μ on Compressive Strength

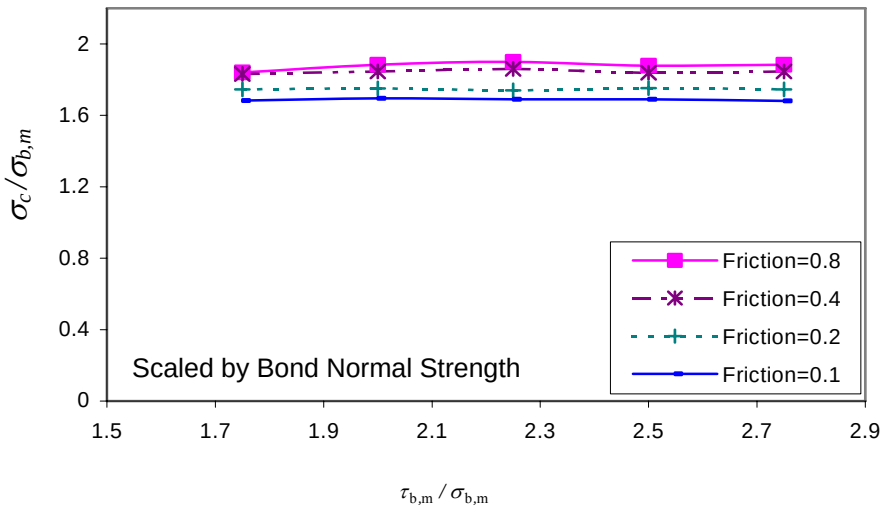

Thus, $\tau_{b,m}/\sigma_{b,m}$ can be eliminated from Equation (9) for $\tau_{b,m}/\sigma_{b,m}$>2. And the compressive strength becomes:

$$\sigma_c/\sigma_{b,m}=1.69\sim1.88. \qquad (15)$$

So, Equation (9) can be reduced to Equation (14) for 0<$\tau_{b,m}/\sigma_{b,m}$<2, and Equation (15) for $\tau_{b,m}/\sigma_{b,m}$>2.

3.1.8 Conclusions

The macroproperties of a specimen modeled by bonded particles are found to be directly or indirectly determined by the microparameters defined at the particle level. The stress-strain relationships of parallel-bonded PFC2D specimens, described by the Young's modulus, is mainly determined by particle contact modulus and affected by particle stiffness ratio and slightly affected by particle size. Equations (10), (11) or (12) can be used for scaling the Young's modulus. The Poisson's ratio is mainly determined by particle stiffness ratio k_n / k_s and slightly affected by particle size. But when particle size is very small, the Poisson's ratio appears to be independent of particle size. Equation (13) can be used to estimate the Poisson's ratio when particle size is selected to be small enough (such as L/R >100). The compressive strength can be scaled by bond shear strength for $\tau_{b,m} / \sigma_{b,m}$ <2 using Equation (14), or estimated by bond normal strength for $\tau_{b,m} / \sigma_{b,m}$ >2 using Equation (15). However, these quantitative relationships between microparameters and macroproperties for parallel-bonded PFC2D specimens are empirical in nature. Some modifications may be needed to model a specific material. In this study, the random distribution of particles is noted to have significant effects on macroproperties of the parallel-bonded PFC2D specimens, but those effects are not considered in the empirical equations. Furthermore, the random distribution of particle bond strength will also affect the value of macroproperties. In fact, for brittle materials, the mechanical properties do have large variations. This is why PFC2D is attractive for simulating brittle materials. The effects of the particle distribution and bond strength distribution of a PFC2D specimen are very important aspects that deserve further investigation. In future work, statistical theory will be used to study the relationships between microparameters and macroproperties of a PFC2D specimen.

3.1.9 Acknowledgements

Financial support of this work by the National Science Foundation under Grant No. DMI-0134579 is gratefully acknowledged.

3.1.10 References

Bangash, T. and Munjiza, A., 2003, "Experimental validation of a computationally efficient beam for combined finite-discrete element modeling of structures in distress", Computational Mechanics, v 30, n 5-6, p.366-373.

Bathurst, R. J. and Rothenburg, L., 1988, “Micromechanical aspects of isotropic granular assemblies with linear contact interactions”, Journal of Applied Mechanics, ASME, v 55 n 1, p.17-23.

Brandt, H., 1955, “A study of the speed of sound in porous granular media”, Journal of Applied Mechanics, ASME, v 22, p.479-486.

Campbell, C.S., 1990, “Rapid granular flows”, Annual Review of Fluid Mechanics, v 22, p.57-92.

Chang, C. S. and Misra, A., 1989, “Theoretical and experimental study of regular packing of granules”, Journal of Engineering Mechanics, ASCE, v 115 n 4, p.704-720.

Chang, C. S. and Misra, A., 1990, “Packing structure and mechanical properties of granulates”, Journal of Engineering Mechanics, v 116 n 5, p.1077-1093.

Cleary, P.W., 1998, “Predicting charge motion, power draw, segregation and wear in ball mills using discrete element methods”, Minerals Engineering, v 11, n 11, p.1061-1080.

Cleary, P.W., 2000, “DEM simulation of industrial particle flows: case studies of dragline excavators, mixing in tumblers and centrifugal mills”, Powder Technology, v 109, n 1, p.83-104.

Cleary, P.W., 2001a, “Modeling comminution devices using DEM”, International Journal for Numerical and Analytical Methods in Geomechanics, v 25, n 1, p.83-105.

Cleary, P.W., 2001b, “Charge behavior and power consumption in ball mills: Sensitivity to mill operating conditions, liner geometry and charge composition”, International Journal of Mineral Processing, v 63, n 2, p.79-114.

Cleary, P.W. and Laurent, B.F.C., 2002, “Comparative study of DEM and experimental results of flow patterns in a ploughshare mixer”, Geotechnical Special Publication, n 117, p.380-385.

Cleary, P.W.; Morrisson, R. and Morrell, S., 2003, “Comparison of DEM and experiment for a scale model SAG mill”, International Journal of Mineral Processing, v 68, n 1-4, p.129-165.

Cundall, P.A., 1971, “A computer model for simulating progressive, large scale movements in block rock systems”, Proceedings of the International Symposium on Rock Mechanics, Nancy II, Art.8.

DePoorter, G.L.; Mustoe, G.G.W. and Greening, D.R., 1993, “Discrete element method (D.E.M.) analysis of the origin of processing induced flaws in advanced ceramics”, Powders & Grains 93, p.445.

Deresiewica, H., 1958, “Stress-strain relations for a simple model of a granular medium”, Journal of Applied Mechanics, ASME, v 25 n 3, p.402-406.

Digby, P. J., 1981, “The effective elastic moduli of porous granular rocks”, Journal of Applied Mechanics, v 48, p.803-808.

Dobry, R. and Ng, Tang-Tat., 1992, “Discrete modeling of stress-strain behaviour of granular media at small and large strains”, Engineering Computations, v 9, p.129-143.

Duffy, J. and Mindlin, R. D., 1957, “Stress-strain relations and vibrations of granular media”, Journal of Applied Mechanics, ASME, v 24 n 4, p.585-593.

Han, K.; Owen, D.R.J. and Peric, D., 2002, “Combined finite/discrete element and explicit/implicit simulations of peen forming process”, Engineering Computations, v 19, n 1-2, p.92-118.

Hocking, G., 1978, “Analysis of toppling-sliding mechanisms for rock slopes.” Proceeding of 19th U.S. Rock Mechanics Symposium, Balkema, Rotterdam, The Netherlands.

Hocking, G., 1992, “The discrete element method of analysis of fragmentations of discontinua”, Engineering Computations, v 9, p.145-155.

Hocking, G., 1993, “Collision impact of a ship with multi-year sea ice”, Proceeding of 2nd International Conference on Discrete Element Methods, MIT Press, Cambridge, Massachusetts, p.369-378.

Huang, H. Y., 1999, Discrete element modeling of tool-rock interaction, Ph.D. Thesis, University of Minnesota, Minneapolis, Minnesota, USA.

Itasca Consulting Group, Inc., 2002, PFC2D (Particle Flow Code in 2 Dimension), Version 2.0. Minneapolis, Minnesota: ICG.

Itasca Consulting Group, Inc., 2003, PFC3D (Particle Flow Code in 3 Dimension), Version 3.0. Minneapolis, Minnesota: ICG.

Kafui, K.D. and Thornton, C., 2000, “Numerical simulations of impact breakage of a spherical crystalline agglomerate”, Powder Technology, v 109, n 1, p.113-132.

Kaitkay, P., 2002, Modeling of rock cutting using distinct element method, Master Thesis, Kansas State University, Manhattan, Kansas, USA.

Komodromos, P.I. and Williams, J.R., 2002a, “On the simulation of deformable bodies using combined discrete and finite element methods”, Geotechnical Special Publication, n 117, p.138-144.

Komodromos, P.I. and Williams, J.R., 2002b, “Utilization of Java and database technology in the development of a combined discrete and finite element multibody dynamics simulator”, Geotechnical Special Publication, n 117, p.118-124.

Lei, S., 2003, “Distinct element modeling of laser assisted machining of silicon nitride ceramics”, in Reddy, R.G. (Ed.), NSF Design, Service and Manufacturing Grantees and Research Conference Proceedings, p.1270-1281.

Lei, S. and Kaitkay, P., 2002, “Micromechanical modeling of rock cutting under pressure boundary conditions using distinct element methods”, Transactions of the North American Manufacturing Research Institution of SME, v 30, p.207-214.

Lin, X. and Ng, T.-T., 1995, “Contact detection algorithms for three dimensional ellipsoids in discrete element modeling”, International Journal for Numerical and Analytical Methods in Geomechanics, v 19, n 9, p.653.

Lin, X. and Ng, T.-T., 1997, “A three-dimensional discrete element model using arrays of ellipsoids”, Géotechnique, v 47, p.319-329.

Mishra, B.K. and Rajamani, R.K., 1992, “Discrete element method for the simulation of ball mills”, Applied Mathematical Modelling, v 16, n 11, p.598-604.

Mishra, B.K. and Rajamani, R.K., 1993, “Numerical simulation of charge motion in ball mills. lifter bar effect”, Minerals & Metallurgical Processing, v 10, n 2, p.86-90.

Mishra, B.K. and Thornton, C., 2002, “An improved contact model for ball mill simulation by the discrete element method”, Advanced Powder Technology, v 13, n 1, p. 25-41.

Miyata, M.; Nakagawa, M. and Mustoe, G.G.W., 2000, “Design considerations of rubble rock foundations based on a discrete superquadric particle simulation method”, Proceeding of 2nd International Conference on Engineering Computational Technology, B.H.V. Topping, ed., Civil-Comp Press, Edinburgh, U.K., p.213-218.

Mohammadi, S.; Owen, D.R.J. and Peric, D., 1998, “Combined finite/discrete element algorithm for delamination analysis of composite”, Finite Elements in Analysis and Design, v 28, n.4, p.321-336.

Munjiza, A. and Andrews, K.R.F., 2000, “Penalty function method for combined finite-discrete element systems comprising large number of separate bodies”, International Journal for Numerical Methods in Engineering, v 49, n 11, p.1377-1396.

Munjiza, A.; Andrews, K.R.F. and White, J.K., 1999a, “Combined single and smeared crack model in combined finite-discrete element analysis”, International Journal for Numerical Methods in Engineering, v 44, n 1, p.41-57.

Munjiza, A.; Bangash, T. and John, N.W.M., 2004, “The combined finite-discrete element method for structural failure and collapse”, Engineering Fracture Mechanics, v 71, n 4-6, p.469-483.

Munjiza, A.; Latham, J.P. and Andrews, K.R.F., 1999b, “Challenges of a coupled combined finite-discrete element approach to explosive induced rock fragmentation”, FRAGBLAST-International Journal for Blasting and Fragmentation, v 3, n 3, p.237-250.

Munjiza, A.; Latham, J.P. and John, N.W.M., 2003, “3D dynamics of discrete element systems comprising irregular discrete elements-Integration solution for finite rotations in 3D”, International Journal for Numerical Methods in Engineering, v 56, n 1, p.35-55.

Munjiza, A.; Owen, D.R.J. and Bicanic, N., 1995, “Combined finite-discrete element method in transient dynamics of fracturing solids”, Engineering Computations, v 12, n 2, p.145-174.

Mustoe, G.G.W. and DePoorter, G., 1993, “A numerical model for the mechanical behavior of particulate media containing non-circular shaped particles”, Powders and Grains 93, p.421-427.

Mustoe, G.G.W.; Heuelmater, H.P. and Chung, J.S., 1992, “Dynamic coupled bending-axial analysis of two-dimensional deep-ocean pipes by the discrete element method”, The Proceedings of the 2nd (1992) International Offshore and Polar Engineering Conference, p.504.

Mustoe, G.G.W. and Miyata, M., 2001, “Material flow analysis of noncircular-shaped granular media using discrete element methods”, Journal of Engineering Mechanics, v 127, n 10, p.1017-1026.

Mustoe, G.G.W.; Miyata, M. and Nakagawa, M., 2000, “Discrete element methods for mechanical analysis of systems of general shaped bodies”, Proceeding of 5th International Conference on Computational Structure Technology, B.H.V. Topping, ed., Civil-Comp Press, Edinburgh, U.K., p.219-224.

Ng, T.-T., 1994, “Numerical simulations of granular soil using elliptical particles”, Computers and Geotechnics, v 16, n 2, p.153-169.

O'Connor, R.M.; Torczynski, J.R.; Preece, D.S.; Klosek, J.T. and Williams, J.R., 1997, “Discrete element modeling of sand production”, International Journal of Rock Mechanics and Mining Sciences, v 34, n 3-4, p.373

Oda, M., Nemat-Nasser, S. and Meharabadi, M. M., 1982, “A statistical study of fabric in a random assembly of spherical granules”, International Journal for Numerical and Analytical Methods in Geomechanics, v 6 n 1, p.77-94.

Oelfke, S.M.; Mustoe, G.G.W. and Kripakov, N.P., 1994, “Application of the discrete element method toward simulation of ground control problems in underground mines”, Proceedings of the 8th International Conference on Computer Methods and Advances in Geomechanics, v 3, p.1865.

Owen, D.R.J. and Feng, Y.T., 2001, “Parallelised finite/discrete element simulation of multi-fracturing solids and discrete systems”, Engineering Computations, v 18, n 3-4, p.557-576.

Owen, D.R.J.; Feng, Y.T.; Cottrel, M.G. and Yu, J., 2002, “Discrete/Finite element modeling of industrial applications with multi-fracturing and particulate phenomena”, Geotechnical Special Publication, n 117, p.11-16.

Owen, D.R.J. and Vaz, M. Jr., 1999, “Computational techniques applied to high-speed machining under adiabatic strain localization conditions”, Computer Methods in Applied Mechanics and Engineering, v 171, n 3, p.445-461.

Potyondy, D.O. and Cundall, P.A., 2004, “A bonded-particle model for rock”, International Journal of Rock Mechanics and Mining Sciences, v 41, n 8, pp.1329 – 1364.

Preece, D.S.; Jensen, R.A. and Chung, S.H., 2001, “Development and application of a 3-D rock blast computer modeling capability using discrete elements - DMCBLAST_3D”, Proceedings of the Annual Conference on Explosives and Blasting Technique, v 1, p.11-18.

Rothenburg, L. and Bathurst, R.J., 1991, “Numerical simulation of idealized granular assemblies with plane elliptical particles”, Computers and Geotechnics, v 11, n 4, p.315-329.

Sawada, S. and Pradham, T.B.S., 1994, “Analysis of anisotropy and particle shape by distinct element method”, Computer Methods and Advantages in Geomechanics, Siriwardane and Zaman, eds., Balkema, Rotterdam, The Netherlands, p.665-670.

Shahinpoor, M., 1983, Advances in the mechanics and the flow of granular materials. Gulf Publishing Company, Houston, Texas, USA.

Sheng, Y.; Lawrence, C.J.; Briscoe, B.J. and Thornton, C., 2002, "3D DEM simulations of powder compaction", Geotechnical Special Publication, n 117, p.305-310.

Tannant, D. D. and Wang, C. G., 2002, "Thin rock support liners modeled with particle flow code", Geotechnical Special Publication, n 117, p.346-352.

Thornton, C., 1992, "Applications of DEM to process engineering problems", Engineering Computations, v 9, n 2, p.289-297.

Thornton, C. and Kafui, D., 2002, "3D DEM simulations of gas-solid fluidised beds", Geotechnical Special Publication, n 117, p.178-182.

Thornton, C. and Zhang, L., 2003, "Numerical simulations of the direct shear test", Chemical Engineering and Technology, v 26, n 2, p.153-156.

Ting, J.M.; Khwaja, M.; Meachum, L.R. and Rowell, J.D., 1993, "An ellipse-based discrete element model for granular materials", International Journal for Numerical and Analytical Methods in Geomechanics, v 17, n 9 p.603-623.

Walton, K., 1978, "The oblique compression of two elastic spheres", Journal of the Mechanics and Physics of Solids, v 26, p.139-150.

Walton, K., 1987, "The effective elastic moduli of a random packing of spheres", Journal of the Mechanics and Physics of Solids, v 35 n 2, p.213-226.

Williams, J. R.; Hocking, G. and Mustoe, G. G. W., 1985, "Theoretical basis of the discrete element method", A. A. Balkema, p.897-906.

Williams, J.R. and O'Connor, R., 1995, "Linear complexity intersection algorithm for discrete element simulation of arbitrary geometries", Engineering Computations, v 12, n 2, p.185-201.

Williams, J.R. and Pentland, A.P., 1992, "Superquadrics and modal dynamics for discrete elements in interactive design", Engineering Computations, v 9, n 2, p.115-127.

Williams, J.R.; Rege, N.; O'Connor, R. and Amaratunga, K., 1995, "Dynamic wave propagation in particulate materials with different particle shapes using a discrete element method", Proceedings of Engineering Mechanics, v 1, p.493-496.

Yang, B. D. and Lei, S., 2004, "Distinct element simulation of conventional and laser assisted machining of silicon nitride ceramics: material removal mechanism," in Kovacevic, R.

(Ed.), 2004 NSF Design, Service and Manufacturing Grantees and Research Conference Proceedings.

Yamane, K.; Nakagawa, M.; Altobelli, S.A.; Tanaka, T. and Tsuji, Y., 1998, “Steady particulate flows in a horizontal rotating cylinder”, Physics of Fluids, v 10, n 6, p.1419-1427.

3.2 Distinct Element Modeling of the Material Removal Process in Conventional and Laser Assisted Machining of Silicon Nitride Ceramics

Published in:
International Journal of Manufacturing Research, Vol. 4, No.1, 2009, pp.74-94,.

Author's Names:
Budong Yang, Xinwei Shen and Shuting Lei

Author's Affiliation:
Department of Industrial and Manufacturing Systems Engineering, Kansas State University, Manhattan, KS 66506

3.2.1 Abstract

This section applies distinct element method (DEM) to simulate the material removal process in conventional and laser assisted machining (LAM) of silicon nitride ceramics. The simulation results demonstrate that DEM can reproduce the conceptual material removal model summarized from experimental observation, including the initiation and propagation of cracks, chip formation process and material removal mechanisms. Simulation results show that material removal is mainly realized by propagation of lateral cracks in both conventional machining and laser assisted machining of silicon nitride. Crushing-type material removal is an important mechanism in conventional machining but not in LAM. The lateral cracks in LAM are easier to propagate to form larger machined chips than in conventional machining. LAM creates less and smaller median cracks, therefore has less surface/subsurface machined damage than conventional machining.

Keywords: Distinct element method, particle flow code, material removal process, laser assisted machining, conventional machining, silicon nitride ceramics

3.2.2 Introduction

Advanced ceramics are wear-resistant, corrosion-resistant and lightweight materials with very high strength, which have been increasingly used in automotive, aerospace, military, medical and other applications. Due to the distortion, contraction, limited formability and lack of dimensional control in net-shape processes for structural ceramics, machining is necessary to obtain the desired surface finish and dimensional tolerance. Various traditional and non-traditional machining technologies, such as grinding and laser assisted machining (LAM), have been developed and applied in precision machining of advanced ceramics. Although many experimental studies have been conducted to understand the material removal mechanisms in machining of ceramics, there are still many questions regarding the micromechanisms of material removal based on the available experimental observations.

Different hypotheses are developed to explain the material removal mechanisms in machining ceramics. Komanduri (1996) discussed the hypothesis of "ductile" grinding of ceramics over the hypothesis of "gentle" grinding. According to "ductile" grinding hypothesis, all materials, regardless of their hardness and brittleness, will undergo a transition from brittle to ductile machining when the depth of cut is smaller than a critical depth of cut. It is assumed that the energy required for plastic deformation is smaller than the energy required to propagate the cracks. Plastic deformation is the predominant material removal mechanism in "ductile" grinding of ceramics. However, there is little plastic deformation in "gentle" grinding hypothesis. According to this hypothesis, the mode of deformation (plastic or brittle) depends on the state of stress, not on the magnitude of the stress. It is hard to explain why the mode of deformation will change merely by decreasing the depth of cut. The superior surface obtained at small depth of cut is due to the light load but not necessary due to plastic deformation. Microcracks are formed but may not propagate to form larger cracks under small loads. This example shows that it is hard to accurately understand the micromechanisms of machining ceramics merely from experimental observations. There is a need to develop a micro-mechanical model of the material removal process for machining ceramics.

Numerical simulation is an alternative way to investigate the micromechanisms of machining ceramics. It has been shown that the material removal in conventional machining of ceramics is dominated by brittle fractures, and the mechanical behavior of ceramics is controlled by the propagation of small cracks, including median cracks, lateral cracks and radial cracks. In order to simulate the material removal mechanisms of ceramic machining, how to treat crack formation and propagation is therefore very important and always a challenge. Finite element method (FEM) has been used to study chip formation and surface damage in machining of ceramics (Ueda et al. 1991; Zhang et al., 2000; Cao, 2001; Chiu et al. 2001; Kumbera at al. 2001). But FEM faces difficulty in dealing with a large number of cracks and treating interactions among broken elements when they come into contact again. Distinct element method (DEM) provides an alternative way by treating materials as arbitrarily sized particles bonded together. When the bonds break, cracks are formed or extended. DEM has proven to be a promising method to simulate rock cutting. Huang (1999) applied DEM to rock cutting and demonstrated that DEM could reproduce the experimental observation of a failure mode transition from brittle to ductile failure depending on a critical depth of cut. Lei and Kaitkay (2002) and Kaitkay (2002) used DEM to model rock cutting and demonstrated that the cutting forces in the simulation agrees well with the experimental results. Tannant and Wang (2002, 2004) applied DEM to thin liners of underground rock support to simulate the liner support mechanisms. Potyondy and Cundall (2004) demonstrated that DEM simulation could reproduce most of the mechanical properties of Lac du Bonnet granite. Extensive studies have shown that DEM is capable to simulate the mechanical behavior of brittle materials.

This study uses particle flow code (PFC), a distinct element method (DEM), to model the material removal process in conventional and laser assisted machining of silicon nitride ceramics. Qualitative comparisons between the simulation results and the experimental observations are conducted to demonstrate that DEM can reproduce many experimental observations of conventional and laser assisted machining of silicon nitride ceramics. Two important improvements are made in this study: (i) to use clusters of circular particles to model silicon nitride ceramics, and (ii) to select a realistic material damping coefficient for dynamic machining simulation. In the following, DEM modelling of the mechanical behavior of silicon nitride ceramics will be first introduced. Then the crack formation and propagation mechanism and chip formation in DEM simulations will be compared to the experimental observations.

Finally the characteristics of LAM will be analyzed by comparing LAM with conventional machining of silicon nitride ceramics.

3.2.3 Modeling the Mechanical Behavior of Silicon Nitride Ceramics

3.2.3.1 Particle Flow Code (PFC)

PFC2D is a two-dimensional particle flow code that models the movement and interaction of circular particles by the distinct element method (DEM), which allows finite displacements and rotations of discrete bodies, including complete detachment, and recognizes new contacts automatically as the calculation progresses. PFC2D is a simplified implementation of the DEM because of the restriction to rigid circular particles, while the general DEM can handle deformable polygonal-shaped particles. The constitutive model defined at the contact governs the interaction between any two circular particles. The constitutive model consists of a stiffness model, a slip model and a bonding model, which controls the deformation, separation, and movement of the particles. PFC2D is able to model a solid by bonding every particle to its neighbors and compacting the particles within four walls. The resulting assembly can be regarded as a "solid" that not only possesses elastic properties, but also is capable of "fracturing" when bonds between these particles break. PFC2D contains extensive logic to facilitate the modelling of solids as closely packed assemblies of bonded particles.

PFC2D simulates the mechanical behavior of a collection of non-uniform-sized circular particles bonded together at their contact points. The rigid particles interact only at the soft contacts, which possess finite normal and shear stiffness. The mechanical behavior of this system is described by the movement of each particle and the force and moment acting at each contact. Newton's laws of motion are the fundamental relation between particle motion and the resultant forces and moments. The contact forces and displacements of the particles are found by tracing the movements of the individual particles. The calculations performed in PFC2D alternate between the application of Newton's second law to the particles and a force-displacement law at the contacts.

In PFC2D, the interaction between particles is a dynamic process and states of equilibrium develop whenever the internal forces between particles balance. A time-stepping algorithm represents the dynamic behavior numerically. It is assumed that velocities and

accelerations of every particle are constant within each time-step. That is, the time step is assumed to be so small that, during a single time step, disturbances cannot propagate from any particle further than its immediate neighbors. Then, at all times, the forces acting on any particle are determined exclusively by its interaction with the particles in contact. Because the speed at which a disturbance can propagate is a function of the physical properties of the discrete system, the time step can be chosen to satisfy the above constraint.

Since PFC2D models a material as a collection of separate particles bonded together, creating a well connected, densely packed assembly, which behaves like the real material, is the first and important step in a successful numerical simulation. The specimen generation procedure in PFC2D follows the following five steps (for details please refer to Potyondy and Cundall, 2004): (1) Compact initial assembly; (2) Install specific isotropic stress; (3) Reduce number of "floating" particles; (4) Install parallel bonds; (5) Relax the specimen. The specimen produced by this procedure is well connected with low locked-in forces. The packing and the locked-in forces are arbitrary and isotropic at the macroscale.

3.2.3.2 Damping Coefficient in PFC Specimen

The interaction of particles in the DEM is treated as a dynamic process. To dissipate kinetic energy, local non-viscous damping is used in PFC2D model by specifying a damping coefficient. The damping coefficient was found to have great effects in the behavior of PFC2D specimens. Hazzard and Young (2000) used a damping coefficient of 0.015 to analyze crack nucleation and propagation in rocks and found that the energy released by crack may have significant influence on the rock behavior. The authors also showed that the effect of decreased damping coefficient from 0.7 to 0.015 was to decrease the unconfined compressive strength by up to 15%. The failure seemed to be more severe with much more rapid crack growth when failure was approached at small damping, while the cracking appeared to be more uniform in the highly damped model. Machining of ceramics is a dynamic process characterized by crack formation and propagation. In order to model this dynamic process and capture the crack formation and propagation mechanism, a realistic damping coefficient needs to be determined for modelling silicon nitride ceramics.

A common measure of energy loss in ceramics is internal friction. Pezzotti et al. (1996) investigated the internal friction of high purity silicon nitride ceramics and the effects of temperature on it. The results show that the damping coefficient increases when temperature

increases. However, the actual damping coefficient in a cutting process full of stress relief fractures would be much higher than the values in these studies. As mentioned above, the material removal of silicon nitride ceramics is a highly dynamic process that is full of initiation and propagation of brittle fractures in the material. The cracks formed during the machining process will greatly change the energy dissipation ability of the specimen. Adams et al. (1973) observed that damages in materials could increase the damping coefficient. Sims et al. (1977) found that damping was sensitive to the damage indicated by the stress wave emissions. Mantena et al. (1986) found that transverse cracks in glass beams induced by static loading significantly increase damping, and that the size and location of the damage zone could be correlated with the changes in damping. Roebben and Van (2000) found that internal friction increases linearly with stress amplitude. The energy dissipation will be large at the tip of cracks where stress concentration leads to high values of stress.

Therefore, from the viewpoint of numerical simulation, it is not easy to determine the realistic damping coefficient for machining ceramics. The cracks generated in machining would continuously change the local damping coefficient. Especially in laser assisted machining, the high temperature will increase the damping coefficient. Based on the values found in the literature (Pezzotti et al. 1996; Roebben et al., 2000; 2002; Pezzotti et al., 2003; Yang et al., 1994a, b), the damping coefficients under different temperatures in machining of silicon nitride are estimated to be 0.012 for 25 ˚C, 0.016 for 1000 ˚C and 0.03 for 1400 ˚C, respectively.

3.2.3.3 Effect of Clusters in PFC Specimen

The single circular particle in PFC2D specimens is a coarse approximation to the real material, especially for silicon nitride with b grain structure that has rod like grains. Several studies (Huang, 1999; Kaitkay, 2002; Potyondy and Cundall, 1999) noted that a single circular particle model had difficulties in reproducing some properties of a material, such as the ratio of compressive and tensile strength of a material. In order to improve the ability of PFC2D specimen to model silicon nitride ceramics, clusters are used in this study. A cluster is defined as a set of particles that are bonded to one another. When using PFC specimen to model Lac du Bonnet granite, Potyondy and Cundall (2004) pointed out that using clusters that more closely resemble the real grain shape in granite could improve the ability of PFC specimens to match the properties of the real materials, such as increasing the slope of the strength envelope and lowering the crack-damage stress.

Using clusters to form irregular grain shapes in PFC specimens can also overcome the problem of easy particle rotation. Circular particles are unrealistically easy to rotate after the bonds are broken and this behavior will affect the behavior of the specimen. Kaitkay (2002) studied the effects of particle rotation and found that particle rotation affects the cutting force significantly. Moreover, unrealistic particle rotation can change the damage mechanism of PFC2D specimens. When particle rotation is not allowed, failure takes place mostly as brittle fracture with bonds breaking in normal as well as shear mode. When particle rotation is allowed, the bonds fail mainly in tension. In the DEM studies of machining brittle materials by Kaitkay (2002), particle rotation is one of the reasons that contribute to the smaller cutting forces in simulation when compared to the experimental results.

In this study, unbroken clusters are created to model the grains in silicon nitride. The bond strength within a cluster is set to a very high value (1×1030 GPa) to avoid breakage within a cluster.

3.2.3.4 Macroproperties of PFC Specimen

3.2.3.4.1 Choosing Microparameters

There are two groups of microparameters to define the macroproperties of a PFC specimen. One is the geometric and physical parameters which determine the dimensions, particle size and particle numbers of the specimen. The other group is constitutive parameters to define the microproperties of the particles and the contacts and bonds. The most important microparameters involved in a PFC specimen are shown in Table 3.2. The cluster is used to model the grains of silicon nitride ceramics. Ideally, the number of balls is chosen to make the size of clusters close to the real grain size. To do so, the average particle size should be very small, thus the calculation time will be increased significantly. In this study, the average particle size is set to 0.045 mm and the number of balls in a cluster is chosen to 3, which is a trade off between accuracy and calculation time. A detailed description of the various microparameters can be found in the PFC manual (Itasca 1999).

Table 3.2 Microparameters for Specimens

Group	Microparameters	25˚C	1000 ˚C	1400 ˚C
Geometric and Physical Parameters	Specimen height (mm)	10	10	10
	Specimen width (mm)	5	5	5
	Minimum particle size (mm)	0.03	0.03	0.03
	Particle size ratio,	2.0	2.0	2.0
	Particle density (kg/m^3)	3200	3200	3200
	Number of balls in cluster	3	3	3
Constitutive Parameters	Particle contact stiffness (GPa)	225	220	60
	Particle stiffness ratio	1.5	1.5	1.5
	Particle friction coefficient	0.4	0.4	0.4
	Particle damping coefficient	0.012	0.016	0.03
	Bond normal strength, mean (MPa)	1150	1100	420
	Bond normal strength, std. dev. (MPa)	230	220	84
	Bond shear strength, mean (MPa)	2300	1100	210
	Bond shear strength, std. dev. (MPa)	460	220	42
	Bond normal strength within cluster (Pa)	1×10^{30}	1×10^{30}	1×10^{30}
	Bond shear strength within cluster (Pa)	1×10^{30}	1×10^{30}	1×10^{30}

3.2.3.4.2 Numerical Material Testing

Since the behavior of a PFC specimen is determined by the microparameters defined at the particle level, numerical compression and bending tests are conducted to match the macroproperties of the specimen to those of silicon nitride. The search for the proper microparameters to match the macroproperties is an iterative process. Although some guidelines and relationships between microparameters and macroproperties exist (Huang, 1999; Itasca, 1999; Yang et al., 2006), several iterations are needed to reach a satisfactory result. Initial microparameters are chosen based on the realistic macroproperties of the material to match. Yang et al. (2006) investigated the relationships between microparameters at particle level and macroproperties of the specimens and established some guidelines to determine the microparameters.

Figure 3.21 Compression Test Configuration

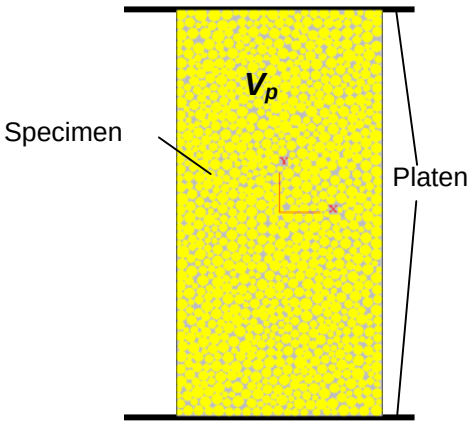

Figure 3.22 Configuration for Four-point Bending Test

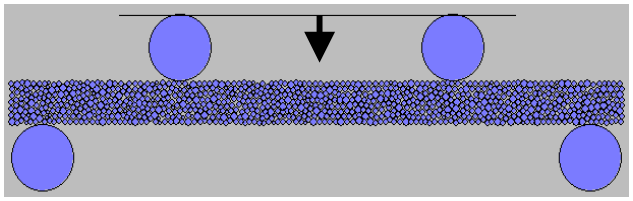

Compression test is used to obtain the stress-strain relationship and to extract the Young's modulus of elasticity, Poisson's ratio and the compressive strength. The compression test is schematically shown in Figure 3.21. The specimen is loaded by moving the top platen at a specified velocity, Vp, while the lower platen is fixed. The stress and strain are monitored during the simulation. For details please refer to the PFC manual or Potyondy and Cundall (2004).

Four-point bending test is used to find the flexural strength of the specimen. Figure 3.22 shows the setup for the bending test. The test configuration is based on ASTM standard (C 1161-94). The specimen is of 4.0 mm wide and 45 mm long. It is supported with a span of 40 mm and

loaded with a span of 20 mm. The load versus displacement at the center of the specimen is monitored during the test. The peak load is used to calculate the flexural strength for the specimen.

3.2.3.4.3 Specimens for Silicon Nitride Ceramics

In this study, two types of specimens are needed for conventional machining and LAM respectively. Based on the results of Lei et al. (2001), the temperature field for the workpiece of LAM can be assumed such that the temperature decreases linearly from 1400 ˚C on the top surface to 1000 ˚C at the bottom. There is no temperature gradient in the horizontal direction. To simplify the problem, this temperature distribution is reflected in the corresponding variations in the mechanical properties (including damping coefficient) in the workpiece. The heat generated in the cutting process is not considered due to its small effect compared to laser heating. In order to generate a specimen for LAM, the properties of the PFC specimens at different temperatures should be matched with those of silicon nitride ceramics.

Numerical compressive and bending tests are conducted to match the properties of silicon nitride ceramic. The values of the selected microparameters and the resulting macroproperties of the PFC specimens are shown in Table 3.2 and 3.3, respectively.

Table 3.3 Properties of PFC Specimens and Silicon Nitride Ceramics

Temperature	Properties	Silicon Nitride	PFC Specimen
25˚C	Young's modulus of elasticity (GPa)	311	316
	Poisson's ratio	0.26	0.25
	Flexural strength (MPa)	720	733
1000 ˚C	Young's modulus of elasticity (GPa)	311	312
	Poisson's ratio	0.26	0.25
	Flexural strength (MPa)	620	610
1400 ˚C	Young's modulus of elasticity (GPa)	89	84
	Poisson's ratio	0.26	0.24
	Flexural strength (MPa)	160	155

3.2.4 Simulation Results and Discussions

Simulations are conducted for conventional and laser assisted machining of silicon nitride ceramics. Figure 5 shows the setup to model the orthogonal machining. The top wall of the specimen is deleted to allow chip formation. The two sides and the bottom of the specimen are constrained with walls to represent the surrounding materials. The cutting tool is advanced at a fixed cutting speed. The cutting tool is modeled as a rigid body by using wall elements. In both conventional and LAM, simulations are conducted under rake angle of 0 and –15 degree. There is no cutting edge radius in simulations. The simulation results of conventional machining are compared with the experimental observations found in the literatures. It is shown that DEM simulation can reproduce most of the experimental observations of the material removal processes for conventional machining of ceramics. Then, DEM simulation results for LAM of silicon nitride ceramic are verified by experimental observations. Finally, material removal processes are compared between conventional and LAM of silicon nitride ceramics. It is shown that DEM simulation could capture the characteristics of LAM.

3.2.4.1 Material Removal Mechanisms in Conventional Machining

3.2.4.1.1 Experimental Observations in Conventional Machining of Ceramics

Many studies have been conducted to understand the material removal mechanisms in conventional machining of ceramics. One commonly used technique to investigate the cracks formed in ceramic machining is sliding indentation experiment (Chandrasekar and Farris, 1997). In an indentation experiment, the indenter induces a plastic deformation zone around the contact point. If the load is larger than a critical value, median cracks will form and grow in a stable way. It is believed that median cracks that propagate perpendicular to the machining direction are responsible for the cracks formed on the machined surface. The lateral cracks, which run parallel to the machined surface, play a dominant role in the chip formation process. The radial cracks emanating from the edge of the contact impression will form surface ring cracks. Crushing of particles in the scratch groove along with median cracks are observed under high loads.

Microscopic observations have shown that material removal during abrasive machining of ceramics is caused by the following mechanisms: lateral cracks breaking open to the surface;

gross fracture due to grain pull-out; median/radial cracks intersecting with each other; plastic micro-cutting through the formation of chips as in single-point turning of metal (Chandrasekar and Farris, 1997). The applied loads on the ceramic surface determine the dominant mechanism. Typically, when the applied loads are small, plastic micro-cutting or indentation mechanism (with upward displacement of material around the indent) is found to be dominant. When the applied loads are large, material removal by brittle fracture is dominant, including lateral cracks breaking onto the surface, grain pullout or a crushing-type of material removal.

The loads in most situations of machining of ceramics are relatively large. Therefore, the mechanical behavior of ceramics is controlled by the propagation of small, sharp cracks and the material removal is dominated by brittle fractures. Ueda et al. (1983, 1991) found that most cracks are formed ahead of the cutting tool and grow forward and slightly downward as the cutting tool advances. Some cracks remain on the machined surface as residual cracks. Other cracks propagate upward to the free surface and lead to chip fragments. Jahanmir et al. (1993a, b) pointed out that the majority of fractures in ground silicon nitride ceramics were initiated from near-surface or surface flaws and the fracture mode was highly intergranular. The depth of median cracks on the ground surface increase with increased depth of cut. Zhang et al. (1988) noticed that the crack penetration depth was approximately proportional to the depth of cut. Oden and Ericsson (1996) observed that the cracked interface was opened parallel to the machined surface but closed perpendicular to it.

Many observations have confirmed the above-mentioned types of cracks including median cracks, lateral cracks and radial cracks. Obvious median cracks and radial cracks were observed in the surface of machined or scratched ceramics (Marshall et al. 1983; Xu and Jahanmir, 1995, Xu et al. 1995). Ueda et al. (1991) observed obvious lateral cracks. Maksoud et al. (1999) investigated surface and subsurface cracks of ground ceramics. Both lateral and median cracks were observed on the machined ceramic surface. It was found that median and lateral cracks were initiated in the sub-surface layers very close to the ground surface and lateral cracks were confined under a thin layer. Typically, the lateral cracks were longer and often larger than median cracks. Figures 3.23 and 3.24 show the typical median and lateral cracks observed in experiments.

Figure 3.23 A Section View of Subsurface Grinding Damage

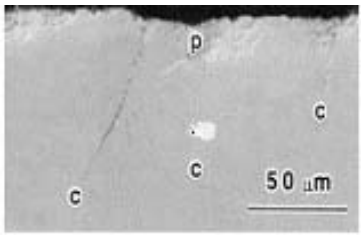

The median cracks are designated by "c", and the plastic zones are designated by "p" (Xu et al., 1996)

Figure 3.24 Crack Propagation in Machining of ZrO2

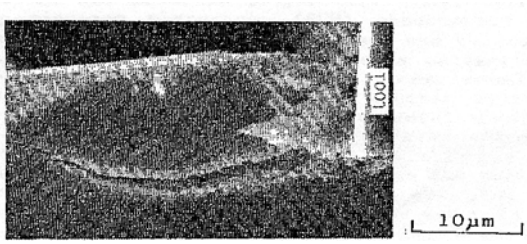

(Ueda et al., 1991)

Based on their experimental results, Zhang et al. (1993) presented a conceptual model to describe the material removal process in five stages: (1) dynamic loading; (2) crack initiation; (3) crack propagation; (4) chip formation; and (5) formation of surface and subsurface damage. This model emphasizes the relationship between macroscopic and microscopic fracture behavior. Zhang et al. (1993) defined two types of chips: machined chip and fractured chip. A machined chip starts from workpiece contact with the cutting tool and then cracks form when the chip moves over the rake face, and finally separates from the machined workpiece due to fracture. A fractured chip is defined as a chip fragment formed without direct contact to, or flow over, the tool rake face. These two types of chips are formed by brittle fracture, which indicates that the chip formation during machining is a macro-scale fracture process. Intergranular cracks may develop within a fractured chip. Almost all of the intergranular cracks initiate at intersections of the grain boundaries. The chip size formed during machining was found to vary significantly. Since both "machined chips" and "fractured chips" defined in Zhang et al. (1993) are created by

brittle fractures, this study will use “machined fracture chip” and “squeezed fracture chip” to designate these two kinds of chips.

The following are the main experimental observations summarized from the literature:

(1) Material removal is dominant by brittle fractures caused by lateral cracks, crushing or grain pullout. Plastic micro-cutting is possible when depth of cut is small, which would form thin ribbon-like chips.

(2) Fracture mode is both inter- and trans-granular. Most cracks are initiated in the sub-surface layer very close to the cutting tool and would grow forward and slightly downward as the cutting tool advances. Median, lateral and radial cracks are observed in many studies. Median cracks are mainly responsible for the cracks remaining on the machined surface. Lateral cracks play a dominant role in chip formation. The depth of median cracks increases with increased depth of cut. Typically, lateral cracks are larger than median cracks.

(3) Chip formation during machining is a macro-scale fracture process. There are mainly two types of chips, i.e., machined fracture chip and squeezed fracture chip. The chip size formed during machining varies significantly. Fractured chips may capture small cracks.

3.2.4.1.2 DEM Simulation Results for Conventional Machining

The simulation results for conventional machining of silicon nitride ceramics are illustrated in Figures 3.25 and 3.26. A typical fractured chip is shown in Figure 3.27. The gray points in the figures are the particles. The short black line segments represent broken bonds. They are microcracks. The specimens’ length is 10mm and the height is 5 mm.

Figure 3.25 Conventional Machining, Length of cut=0.3 mm, t=1 mm, α= 0 deg, V=0.5 m/s

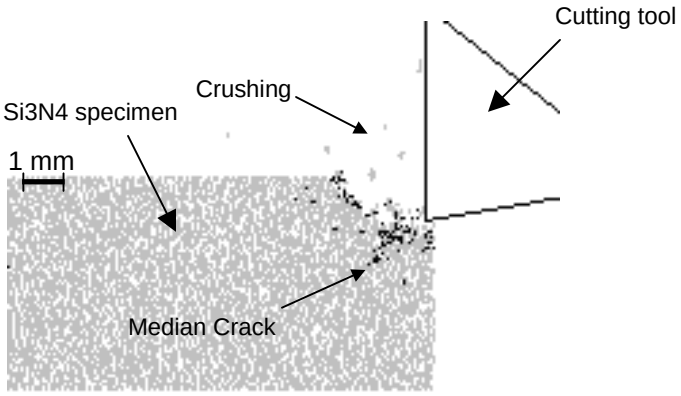

Figure 3.26 Conventional Machining, t=0.5 mm, α= -15 deg, V=0.5 m/s

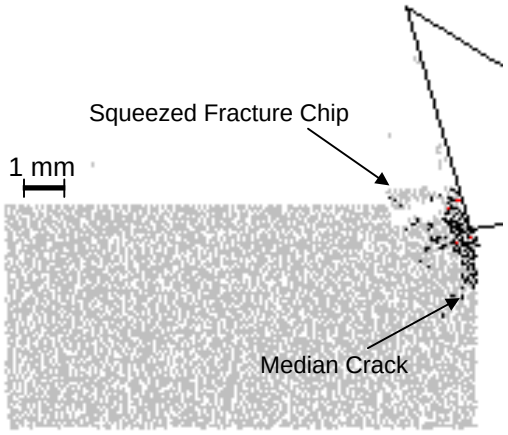

(a): Length of cut=0.4 mm.

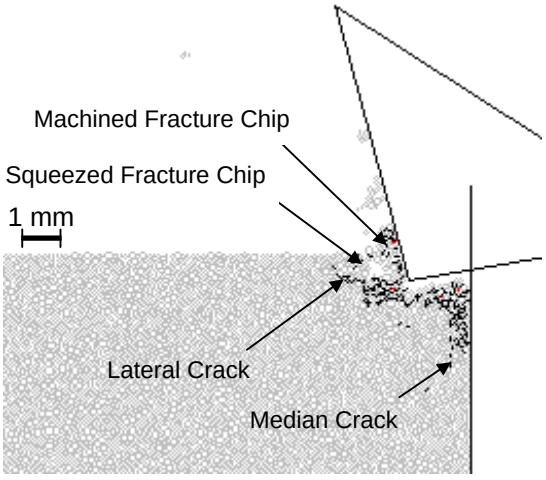

(b): Length of cut=1.2 mm.

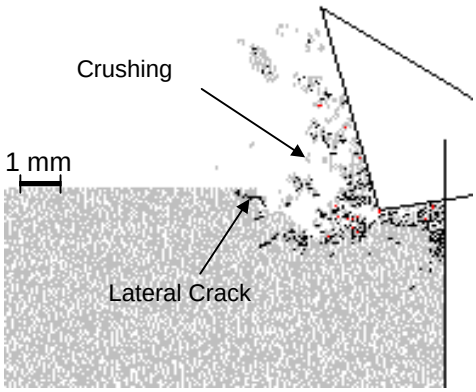

(c): Length of cut=1.6 mm

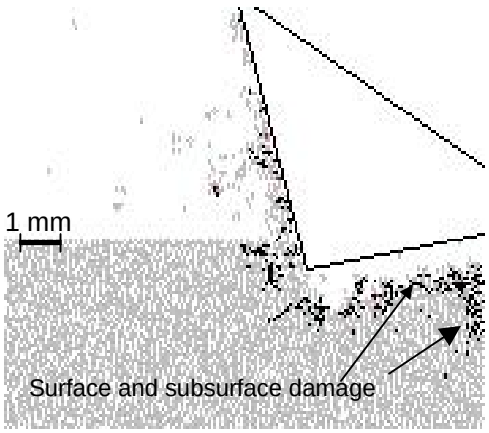

(d) Length of cut=3.2 mm.

Figure 3.27 Cracks in a Fractured Chip

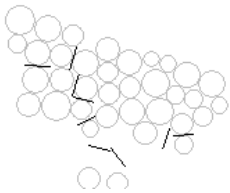

The simulation results can reproduce most of the experimental observations in conventional machining of ceramics found in the literature as summarized in Section 3.2.4.1.1. The main results from the simulations are summarized in the following:

(1) The material removal is mainly realized by brittle fractures. The brittle fractures are either caused by lateral cracks (Figures 3.26a,b) or by crushing-type material removal mechanism (Figure 3.25 and 3.26c).

(2) Most cracks are initiated close to the cutting tool. Some cracks propagate forward to form lateral cracks, as shown in Figures 3.26b, c. Some cracks develop slightly downward to form median cracks, as shown in Figures 3.26a, b. There are some microcracks formed further away from the cutting tool, either ahead or downward.

(3) Both the median and lateral cracks are very similar to the cracks observed in experiments, as illustrated by comparing the median cracks in Figure 3.26b with Figure 3.23 and comparing the lateral crack in Figure 3.26b with Figure 3.24. Median cracks will remain in the machined surface and become the main defects.

(4) As shown in Figure 3.26, the crack initiation and propagation, the chip formation and the formation of surface and subsurface damage are very similar to the conceptual model proposed by Zhang et al. (1993), which is based on experimental observations. Both machined fracture chips and squeezed fracture chips are observed in the simulation process as shown in Figure 3.26b. Lateral cracks are mainly responsible for the chip formation. Crushing type material removal is illustrated in Figures 3.25 and 3.26c.

(5) The chip size varies significantly depending on the chip formation mechanism, i.e., formed by the propagation of lateral cracks or by the crushing type material removal. Lateral cracks usually lead to relatively large chips.

(6) Chip formation caused by lateral cracks is mainly a macro-scale fracture process. The microcracks nucleate to form either lateral cracks or median cracks. When the lateral cracks propagate towards the surface, chips are formed.

(7) As shown in Figure 3.27, fractured chips may capture intergranular cracks. Zhang et al. (1993) observed similar results in experiments.

The simulation results demonstrate that distinct element modelling is a promising method to model the material removal mechanisms of conventional machining of silicon nitride ceramics. It is shown that DEM can reproduce many experimental observations and the

conceptual material removal model summarized from experiments. Material removal mechanisms in conventional machining of silicon nitride are characterized by brittle fractures caused by either lateral cracks or crushing.

3.2.4.2 Material Removal Mechanisms in Laser Assisted Machining

3.2.4.2.1 Experimental observations in LAM of silicon nitride ceramics

Although LAM of ceramics has been shown to produce less subsurface cracks compared to conventional machining, its material removal mechanisms are still not fully understood. In an experimental investigation, Lei et al. (2001) pointed out that material is removed both thermally and mechanically during the LAM of silicon nitride ceramics. The authors postulated three material removal mechanisms in LAM. First, the workpiece surface may experience oxidation, melting, and vaporization because of the high temperature of LAM. Second, material is removed by plastic deformation in the shear zone because of the viscous flow of a glassy grain-boundary phase and reorientation of Si3N4 grains. Third, the initiation, nucleation and propagation of intergranular microcracks may form macrocracks and result in segmented chips. Usually, the material removed by the thermal process is small compared to that by the cutting process. There are fewer subsurface cracks observed in LAM of silicon nitride than conventional machining (Lei et al. 2001).

In order to further understand the material removal mechanisms in LAM of ceramics, extensive laser assisted machining experiments have been conducted. The Si3N4 workpiece has dimensions of 4.3x5.3x48 mm. A polycrystalline cubic boron nitride (PCBN) tipped insert is clamped in a self-made tool holder. The insert has a cutting edge width of 0.1 mm with a chamfer of 30°. The rake angle in LAM experiments is about -10°. A diode laser system is used to generate a high power laser beam, which is delivered through the optical fiber and focused on the workpiece surface at the angle of about 60 deg. Laser spot has a diameter of about 3 mm. Laser power is 250 W and 390 W for 838 °C and 1595 °C respectively. Laser power is adjusted to realize different temperature. Please refer to Yang et al (2007) for the detailed experimental set up. Experimental results show that laser heating is an effective method to reduce the cutting force in machining silicon nitride ceramics. When the temperature at the measurement point increases from 838 °C to 1319 °C, the tangential force (cutting force) decreases by 50% and the radial force (Feed force) decreases by 45%. Correspondingly, the specific cutting energy is less

than 20 percent that of conventional machining. The decreased cutting forces (cutting energy) indicate that the material is softened under high temperature and plastic deformation or viscoplastical deformation of the glassy phase may present in LAM.

Sample chips are collected and examined using an optical microscope. Chip segments produced by LAM under 1480 °C and 1595 °C are shown in Figure 3.28. There are no long continuous chips (like those in metal cutting) in LAM. It shows that the material removal in LAM is mainly realized by brittle fracture. But some chips appear to be semi-continuous with various lengths. The larger chips at 1595 °C indicate that more plastic deformation occurs at higher temperature. Figure 3.29a shows a typical chip microstructure that consists of mostly amorphous lumps of material. Some broken Si3N4 grains are visible. For comparison purpose, the surface microstructure of an as-received workpiece is shown in Figure 3.29b. The interlocking Si3N4 grains with amorphous boundary phase can be seen. Figure 3.30 shows a semi-continuous chip captured some internal cracks.

Figure 3.28 Chips of LAM at: (a)1480 °C and (b)1595 °C

Figure 3.29 SEM micrograph: (a) a chip of LAM; (b) as-received surface

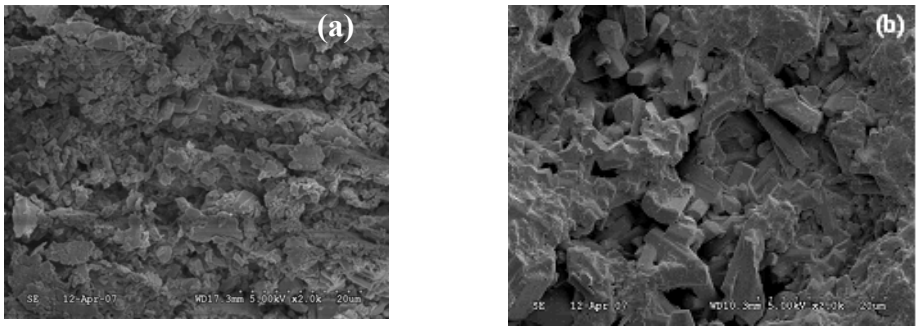

Figure 3.30 A Semi-continuous Chip

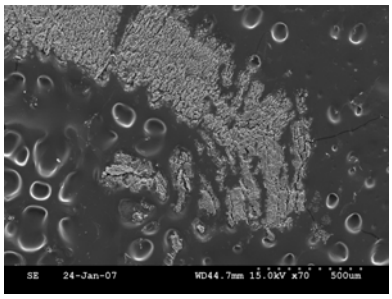

The plastic behavior of silicon nitride ceramics at high temperature can be ascribed to the viscoplastic deformation of the glassy phase. When the temperature is above the glass transition temperature, the viscosity of the glassy grain-boundary phase material decreases, which results in chip formation by viscoplastic deformation of the second phase. Specifically, silicon nitride grains initially slide and rotate within softened glassy phase under the advancement of the cutting tool, and the glassy phase flows around Si3N4 grains, resulting in plastic deformation. When cracks initiate and propagate to the boundary, chips are formed and separated. Therefore, two physical mechanisms can be related to material removal by the cutting tool: (1) plastic deformation in the shear zone by viscous flow of the glassy grain-boundary phase and (2) coalescence and propagation of intergranular microcracks to form chip segment.

Figure 3.31 shows a comparison of LAM-ed and ground surfaces. LAM was done at the workpiece temperature of 1349 °C. The ground surface is as-received from the manufacturer. Both surfaces show visible process marks, although they are more pronounced on the ground surface. The surface roughness Ra from laser assisted machining is about 0.3-0.35 μm when the temperature is above 1150 °C, while the surface roughness of the ground surface is about 0.4 μm. For a detailed discussion on the surface roughness, please refer to Yang et al. (2007). Though the surface roughness in LAM is comparable to that of grinding, the material removal mechanisms are quite different in these two processes. At a higher magnification, as shown in Figure 3.32, different characteristics are apparent for the two types of machined surfaces. The grinding marks are clearly seen at this magnification, while it is hard to tell for the LAM-ed surface. It appears that the LAM-ed surface is more uniform with some loosely attached particles. These loose particles may be formed by the displaced surface material under high temperature or maybe the ‘hot fluidic’ chips that re-solidify on the machined surface after they

are cooled down. In contrast, the ground surface is not uniform, with some seemingly very smooth areas interrupted by irregular microfracture regions.

Figure 3.31 SEM Micrographs of (a) LAMill-ed surface and (b) ground surface

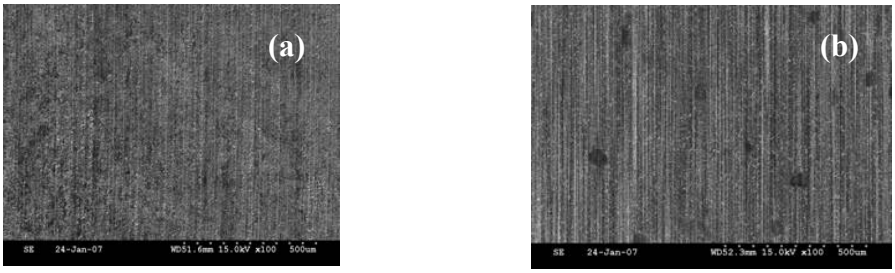

Figure 3.32 Surface Microstructure of (a) LAMill-ed surface and (b)ground surface

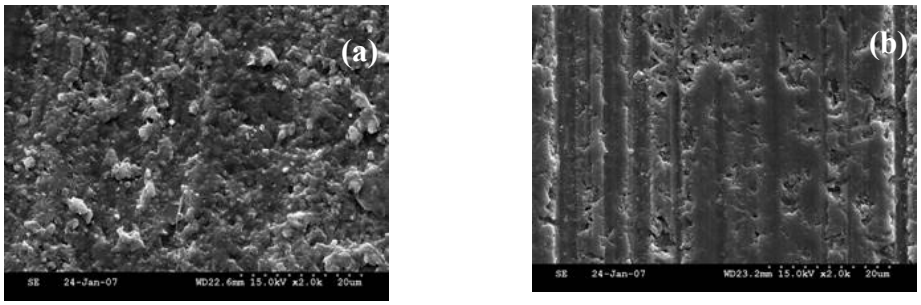

The different surface characteristics demonstrate the differences in material removal mechanisms for LAM and grinding. In LAM, material is first softened and then mainly removed by shear-induced flow under intergranular fractures. This mechanism results in fewer microfracture and damage zones on the machined surface. But in grinding, material is removed mainly by brittle contact between diamond abrasives in the grinding wheel and the brittle workpiece, forming heavily scratched areas. Some abrasive grains smear over the surface, producing some smooth regions.

The material removal process in LAM can be summarized as following:

(1) Material removal in LAM appears to be achieved mainly by brittle fractures.

(2) LAM of ceramics demonstrates more plastic or viscoplastical deformation than conventional machining.

(3) LAM produces fewer surface cracks than conventional machining.

(4) LAM creates larger chips than conventional machining.

3.2.4.2.2 DEM Simulation Results for LAM

The simulation results for LAM of silicon nitride ceramics are illustrated in Figures 3.33, 3.34 and 3.35.

Figure 3.33 Simulation Results for LAM, t=1 mm, α=0 deg, V=0.5 m/s

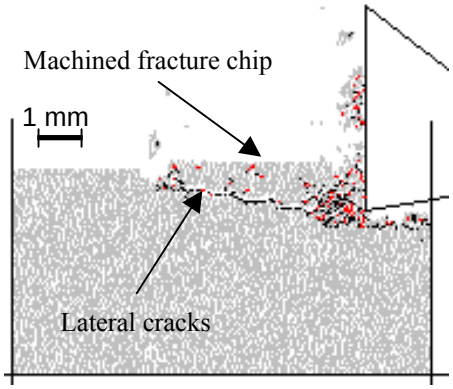

Length of cut=1.6 mm.

Figure 3.34 Simulation Results for LAM, t=0.5 mm α= -15 deg, V=0.5 m/s

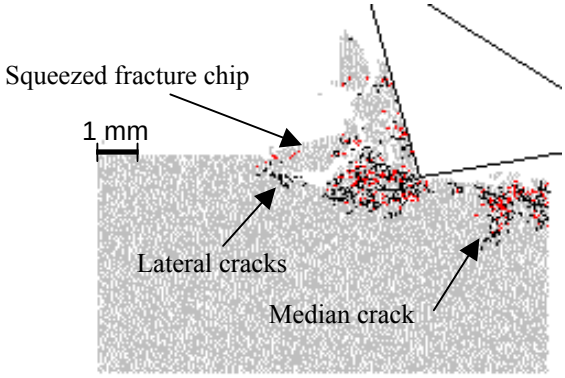

Length of cut=3.0 mm.

Figure 3.35 Simulation Results for LAM t=0.5mm, α=0 deg, V=0.5 m/s

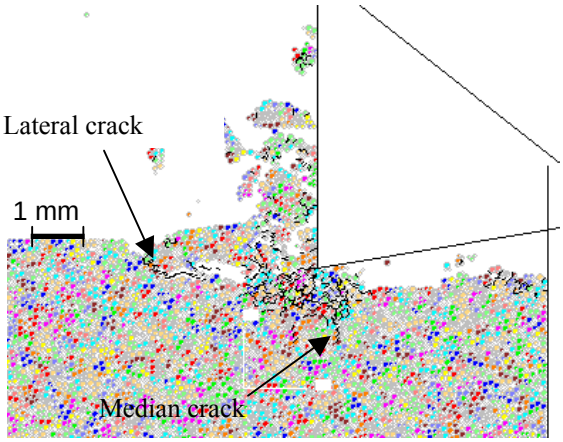

Length of cut=3.8 mm

Simulation results show that material removal and chip formation in LAM of silicon nitride are similar to conventional machining. The main results from the LAM simulations are summarized in the following:

(1) The material removal in LAM of silicon nitride ceramics is mainly realized by brittle fractures. Most of the brittle fractures in LAM are caused by lateral cracks that propagate onto the machined surface. But there are fewer crushing type material removal observed in LAM than in conventional machining.

(2) The median cracks and lateral cracks are very similar to the cracks observed in conventional machining. Median cracks will remain in machined surface and become the main defects. But there are fewer median cracks formed in LAM than in conventional machining. The sizes of the median cracks are also smaller in LAM while the lateral cracks are usually larger and longer.

(3) Both machined fracture chips and squeezed fracture chips are observed in the LAM simulation. Chip formation is mainly caused by lateral cracks. Chip sizes are generally larger in LAM than in conventional machining.

(4) The same as in conventional machining, chip formation caused by lateral cracks in LAM is mainly a macro-scale fracture process. The microcracks nucleate to form either lateral

cracks or median cracks. When the lateral cracks propagate toward the surface, chips are formed. As shown in Figures 3.33, 3.34 and 3.35, fractured chips may capture intergranular cracks.

(5) There are generally more median cracks formed under machining with negative rake angle than with zero rake angle, as illustrated by comparing Figure 3.34 with Figures 3.33 and 3.35.

3.2.4.3 Comparison Between LAM and Conventional Machining of Silicon Nitride

Although material removal in both LAM and conventional machining of silicon nitride is mainly realized by brittle fractures, LAM demonstrates more ductile behavior than conventional machining. The following are some differences observed in the simulation results:

(1) In conventional machining, there are two important material removal mechanisms: lateral fractures breaking onto surface and crushing-type material removal. These two mechanisms happen alternatively during the machining process. However, brittle fractures in LAM are mainly caused by lateral cracks propagating to the surface. Less crushing-type material removal is observed in LAM. Material removal in LAM shows more ductile material behavior.

(2) The damaged layer in LAM is thinner than in conventional machining. The cracks formed in LAM tend to develop to lateral cracks because the top surface is soft and weak due to laser heating. Therefore, LAM has less median cracks formed during the machining process. Even if a microcrack develops to a median crack, it would not propagate so deep in LAM as in conventional machining. Therefore, there is less damage to the machined surface in LAM.

(3) The chips formed in LAM are larger than the chips in conventional machining. Because of laser heating, lateral cracks are easy to propagate to form larger and longer lateral cracks and therefore, produce large chips in LAM than in conventional machining.

3.2.5 Conclusions

The simulation results of conventional machining and LAM of silicon nitride demonstrate that distinct element modeling is a promising method to model the material removal process of machining silicon nitride ceramics. It is shown that DEM can reproduce many experimental observations in machining of ceramics and realize the conceptual material removal model presented by Zhang et al. (1993). Material removal mechanisms in conventional machining of silicon nitride are characterized by brittle fractures caused by either lateral cracks or crushing. Material removal in LAM is mostly realized by propagation of lateral cracks. LAM

has less and short median cracks and thus less and shallow damage layer on the machined surface. The differences between conventional machining and LAM are attributed to the softened material of the cutting zone in LAM. This makes the lateral cracks easy to propagate.

Although the cluster model can improve the behavior of PFC2D specimens, there are some limitations in this simple cluster model. One is that the clusters are unbreakable because the bond strength inside a cluster is set to be very high. Unbreakable clusters can possibly cause unrealistic large and deep damage, especially in LAM because of the decreased bond strength set between clusters. The other limitation is that the clusters do not match the real grain sizes and shapes of silicon nitride. Thus, this simple cluster model can be improved by allowing trans-granular failure and by matching the real grain shapes and sizes of silicon nitride. Furthermore, damping coefficient may greatly affect the initiation and propagation of cracks and thus the material removal mechanism and chip formation. Further research should investigate the effects of damping coefficient on material removal in machining of silicon nitride.

3.2.6 Acknowledgements

Financial support of this work by the National Science Foundation under Grant No. DMI-0134579 is gratefully acknowledged.

3.2.7 References

Adams, R.D., Flitcroft, J.E., Hancox, N.L., and Reynolds, W.N., 1973, "Effects of shear damage on the torsional behavior of carbon fiber reinforcement plastics," Journal of Composite Materials, Vol.7, p.68-75.

Cao, Y., 2001, "Failure analysis of exit edges in ceramic machining using finite element analysis," Engineering Failure Analysis, Vol.8, p.325-338.

Chandrasekar, S., and Farris, T.N., 1997, "Machining and surface finishing of brittle solids," Sadhana - Academy Proceedings in Engineering Sciences, Vol. 22, No. pt 3, p. 473-481.

Chiu, W.-C, Endres, W.J., and Thouless, M.D., 2001, "An analysis of surface cracking during orthogonal machining of glass," Machining Science and Technology, Vol.5, No.2, p.95-215.

Hazzard, J.F., and Young, R.P., 2000, "Micromechanical modelling of cracking and failure in brittle rocks," Journal of Geophysical Research, Vol.105, No.B7, p.16683-16697.

Huang, H. Y., 1999, Discrete element modelling of tool-rock interaction, Ph.D. Thesis, University of Minnesota, Minneapolis, Minnesota, USA.

Itasca Consulting Group, Inc., 1999, "Particle flow code in 2 dimensions," Minneapolis, Minnesota, USA.

Jahanmir, S., Strakna, T.J. Quinn, G.D. Liang, H., Allor, R.L., and West, R.D., 1993a, "Effect of grinding on strength and surface integrity of silicon nitride: part I," NIST Special Publication, n 847, p.263-277.

Jahanmir, S., Strakna, T.J. Quinn, G.D. Liang, H., Allor, R.L., and West, R.D., 1993b, "Effect of grinding on strength and surface integrity of silicon nitride: part II," NIST Special Publication, n 847, p.279-291.

Kaitkay, P., 2002, Modelling of rock cutting using distinct element method, Master Thesis, Kansas State University, Manhattan, Kansas, USA.

Komanduri R., 1996, "On material removal mechanisms in finishing of advanced ceramics and glasses", Annals of the CIRP, Vol. 45, No. 1, p.509-513.

Kumbera T. G., Cherukuri H. P., Patten J. A., Brand C. J., and Marusich T. D., 2001, "Numerical simulations of ductile machining of silicon nitride with a cutting tool of defined geometry," Machining Science and Technology, Vol.5 No.3, p.341-352.

Lei, S., and Kaitkay, P., 2002, "Micromechanical modelling of rock cutting under pressure boundary conditions using distinct element methods," Transactions of the North American Manufacturing Research Institution of SME, Vol. 30, p.207-214.

Lei, S., Shin, Y. C., and Incropera, F. P., 2001, "Experiment investigation of thermo-mechanical characteristics in Laser-Assisted Machining of silicon nitride ceramics," Journal of Manufacturing Science and Engineering, Transactions of the ASME, Vol. 123, p.639-646.

Maksoud, T.M.A., Mokbel, A.A., and Morgan, J.E., 1999, "Evaluation of surface and sub-surface cracks of ground ceramic," Journal of Materials Processing Technology, Vol. 88, n 1, p.222-243.

Mantena, R., Gibson, R.F., and Place, T.A., 1986, "Damping capacity measurements of degradation in advanced materials," SAMPE Quarterly, Vol. 17, No.3, p.20-31.

Marshall, D. B., Evans, A. G., Khuri-Yakub, B.T., Tien, J.W., and Kino, G.S., 1983, "The nature of machining damage in brittle materials," Proceedings of The Royal Society of London, Series A: Mathematical and Physical Sciences, Vol.385, No.1789, p.461-475.

Odén, M., and Ericsson, T., 1996, "Near-surface deformation in an alumina-silicon carbide-whisker composite due to surface machining," Journal of the American Ceramic Society, Vol.79, No.8, p.2134-2140.

Pezzotti, G., Ota, K., and Kleeb, H.-J., 1996, "Grain-boundary relaxation in high-purity silicon nitride," Journal of the American Ceramic Society, Vol.79, No.9, p.2237-2246.

Pezzotti, G., Ota, K., and Yamamoto, Y., 2003, "Element Mechanics Behind the High-Temperature Deformation Behavior of Lutetium-Doped Silicon Nitride," Journal of American Ceramics Society, Vol. 86, n3, pp.471-474.

Potyondy, D. O., and Cundall, P. A., 1999, "Modelling of notch formation in the URL mine-by tunnel: phase IV—Enhancements to the PFC model of rock," Itasca Consulting Group, Inc., Report to Atomic Energy of Canada Limited (AECL), April. Issued as Ontario Hydro Nuclear Waste Management Division Report No. 06819-REP-01200-10002-R00.

Potyondy, D. O., and Cundall, P. A., 2004, "A bonded-particle model for rock," International Journal of Rock Mechanics and Mining Sciences, Vol.41, p.1329-1364.

Roebben, G., and Van der Biest, O., 2000, "Elastic and anelastic properties of silicon nitride at high temperatures by non-destructive impulse excitation," Materials Science Forum, Vol.325-326, p.167-172.

Roebben, G., Donzel, L., Steen, M., Schaller, R., and Van der Biest, O., 2000, "Fatigue Resistant Silicon Nitride Ceramics due to Anelastic Deformation and Energy Dissipation," Journal of Alloys and Compounds, Vol. 310, pp.39-43.

Roebben, G., Duan, R.G., Sciti, D., and Van der Biest, O., 2002, "Assessments of the High Temperature Elastic and Damping Properties of Silicon Nitride and Carbides with the Impulse Excitation Technique," Journal of the European Ceramic Society, Vol.22, pp.2501-2509.

Sims, G.D., Dean, G.D., Read, B.E., and Western, B.C., 1977, "Assessment of damage in GRP laminates by stress wave emission and dynamic mechanical measurements," Journal of Materials Science, Vol.12, p.2329-2342.

Tannant, D. D. and Wang, C. G., 2002, "Thin rock support liners modeled with particle flow code", Geotechnical Special Publication, n 117, p.346-352.

Tannant, D. D. and Wang, C. G., 2004, "Thin tunnel liners modelled with particle flow code", Engineering Computations, v 21, n 2, p 318-42.

Ueda, K., Sugita, T., and Hiraga, H., 1991, “J-integral approach to material removal mechanisms in microcutting of ceramics,” CIRP Annals, Manufacturing Technology, Vol.40, No.1, p.61-64.

Ueda, K., Sugita, T., and Tsuwa, H., 1983, “Application of fracture mechanics in microcutting of engineering ceramics,” Annals of the CIRP, Vol.32, No.1, p.83-86.

Xu, H.H.K., and Jahanmir, S., 1995, “Effect of microstructure on abrasive machining of ceramics,” Ceramic engineering and science proceedings, Vol.16, No.1, p.295-314.

Xu, H.H.K., Jahanmir, S., and Ives, K., 1996, “Material removal and damage formation mechanisms in grinding silicon nitride,” Journal of Materials research, Vol.11, No.7, p.1717-1724.

Xu, H.H.K., Padture, Nitin P., and Jahanmir, S., 1995, “Effect of microstructure on material-removal mechanisms and damage tolerance in abrasive machining of silicon carbide,” Journal of the American Ceramic Society, Vol.78, No.9, p.2443-2448.

Yang, B., Deines, T.W., Geist, C.M., and Lei, S., 2007, “An Experimental Study of Laser Assisted Milling of Silicon Nitride Ceramic,” Transactions of the North American Manufacturing Research Institution of SME, Vol. 35, pp.473-480.

Yang, B., Jiao, Y., and Lei, S., 2006, “A study on the effects of microparameters on macroproperties for specimens created by bonded particles,” Engineering Computations, Vol.23, No.6, p.607-631.

Yang, S., and Gibson, R. F., 1994a, “Dynamic Mechanical Properties of Ceramics and Ceramic Composites at Elevated Temperatures,” Materials for Noise and Vibration Control, NCA-Vol.18/DE-Vol.80, pp.43-51.

Yang, S., and Gibson, R. F., 1994b, “Internal Damping of Silicon Nitride and Silicon Nitride Composites with Silicon Carbide Whiskers to 1100°C,” Ceramic Transactions, Vol. 46, pp.709-720.

Zhang, B., Tokura, H., and Yoshikawa, M., 1988, “Study on surface cracking of alumina scratched by single-point diamonds,” Journal of materials science, Vol.23, No.9, p.3214-3224.

Zhang, G.M., Anand, D.K., Ghosh, S., and Ko, W.F., 1993, “Study of the formation of macro- and micro-cracks during machining of ceramics,” NIST Special Publication, No. 847, p.465-478.

Zhang, G.M., Cao, Y., and Rekow, D., 2000, “A computational approach to evaluate surface integrity of glass ceramics,” Transactions of NAMRI/SME, Vol.28, p.279-284.

CHAPTER 4 - Summary and Conclusions

This work is the first comprehensive machinability study of laser assisted milling of silicon nitride ceramics. It shows that laser assistance significantly enhances the machinability for silicon nitride ceramics, enabling the material to be cut by milling without breaking the cutting tip. Material removal in laser assisted milling shows plastic deformation characteristics and the size of machined chips increases as temperature increases. Cutting force and tool wear decreases significantly as workpiece temperature increases. Very good surface finish is obtained in LAMill. The LAMill-ed surface shows consistent characteristics without large microcrack zones. When temperature is higher than 1000 °C, no visible entry edge chipping is observed. And exit edge chipping decreases considerably as the temperature increases. Controlling the exit angle is an effective and economic way to eliminate the macroscale exit edge chipping. There are more supporting material ahead of the cutter when the exit angle is large so that less and smaller edge chippings are formed. A blunt exit angle will also help reduce the exit edge chipping by greatly reducing the Y direction cutting force and slightly reducing Z direction force that are directly related to exit edge chippings.

For the first time, this study extensively investigated the mechanisms of edge chipping in LAMill of silicon nitride ceramics. The mechanisms of the elevated temperature on edge chipping include softening and toughening mechanisms. When temperature increases, softening always helps to reduce edge chipping by reducing the cutting force, though the efficiency is different at different temperature range. When temperature is above the softening point and below the brittle/ductile transition temperature, the mechanism is mainly through softening. Toughening mechanism will not take effect until the temperature is well above the glassy phase transition temperature. When temperature is above the brittle/ductile transition temperature, toughening mechanism contributes significantly to the reduced edge chipping. And the largest efficiency of toughening happens in a narrow temperature range between 1200 -1400°C. The coupled effects of softening and toughening shows that the temperature range between 1200-1400°C has the most significant effect to reduce edge chipping in laser assisted machining.

This study is also the first attempt to apply distinct element method (DEM) to simulate the micro-mechanical behavior of ceramic machining. Specimens with bonded circular particles

are created to model the silicon nitride material. Extensive DEM simulations are conducted to investigate the relationships between microparameters at particle level and macroproperties of the specimens that are modeled by bonded particles. Specifically, the effects of particle size, particle size ratio, particle contact modulus, contact stiffness ratio, friction coefficient, bond normal and shear strength on the properties of the specimens are investigated. It is shown that the Young's modulus of elasticity of the specimens is mainly determined by contact modulus and affected by the contact stiffness ratio and particle size. The Poisson's ratio of the specimens is mainly determined by contact stiffness ratio and slightly affected by particle size when particle size is large. The compressive strength of the specimens is mainly determined by bond normal strength or bond shear strength and greatly affected by friction coefficient. Quantitative relationships between particle level parameters and mechanical properties of the bonded particle specimens are obtained.

Clusters are used to match the rod-shaped grain in silicon nitride when simulating the micro-mechanical behavior of machining. It is shown that DEM is a very promising method to model the material removal mechanisms, chip formation, crack initiation and propagation in machining silicon nitride ceramics. DEM can reproduce many experimental observations in machining of ceramics and realize the conceptual material removal model summarized from experiments. Material removal mechanisms in conventional machining of silicon nitride are characterized by brittle fractures caused by either lateral cracks or crushing. Material removal in LAM is mostly realized by propagation of lateral cracks. LAM has less and short median cracks and thus less and shallow damage layer on the machined surface. The differences between conventional machining and LAM are attributed to the softened material of the cutting zone in LAM. This makes the lateral cracks easy to propagate.

Although the cluster model can improve the behavior of PFC2D specimens, there are some limitations in this simple cluster model. One is that the clusters are unbreakable because the bond strength inside a cluster is set to be very high. Unbreakable clusters can possibly cause unrealistic large and deep damage, especially in LAM because of the decreased bond strength set between clusters. The other limitation is that the clusters do not match the real grain sizes and shapes of silicon nitride. Thus, this simple cluster model can be improved by allowing trans-granular failure and by matching the real grain shapes and sizes of silicon nitride. Furthermore,

damping coefficient may greatly affect the initiation and propagation of cracks and thus the material removal mechanism and chip formation.

Future experimental research should further investigate surface/subsurface cracks and residual stresses of the LAM-ed ceramic parts. It is well established that surface/subsurface cracks and residual stresses strongly affect the mechanical properties in the machined parts, especially the fracture strength and fatigue life. Hence, it is critical that surface/subsurface damages and residual stresses produced by LAM be measured and compared with those induced by grinding. The ultimate goal of crack-free machining is to minimize machining-induced strength degradation. The strength degradation of advanced ceramic parts by laser assisted machining should be investigated by bending tests and compared with that of grinding. In order to minimize the strength degradation, the mechanisms of strength degradation in LAM need to be investigated experimentally and theoretically. Furthermore, extensive parametric studies are needed to apply laser assisted machining in real industrial applications.

Further research in DEM simulation should improve the simple cluster model to match the real shape and grain size of silicon nitride ceramics. Further simulation efforts could also investigate the effects of damping coefficient on material removal. Extensive simulations are needed to establish reference process parameters for industrial applications of laser assisted machining of various advanced ceramics.

Appendix A - Publications During Ph.D. Study

Journal and Transaction Publications

1. Yang B., Shen X. and Lei S., (2009), "Distinct Element Modeling of the Material Removal Process in Conventional and Laser Assisted Machining of Silicon Nitride Ceramics", International Journal of Manufacturing Research, Vol. 4, No.1, pp.74-94.

2. Yang B., Shen X., and Lei S., (2009), "Mechanisms of Edge Chipping in Laser Assisted Machining of Silicon Nitride Ceramics", International Journal of Machine Tools and Manufacture, Vol. 49, No. 3-4, pp.344-350.

3. Yang B. and Lei, S., (2008) "Laser-Assisted Milling of Silicon Nitride Ceramic: A Machinability Study", International Journal of Mechatronics and Manufacturing Systems, Vol. 1, No. 1, pp.116-130.

4. Qian, L., Yang, B., and Lei, S., (2008) "Comparing and Combining Off-line Feedrate Rescheduling Strategies in Free-form Surface Machining with Feedrate Acceleration and Deceleration", Robotics and Computer-Integrated Manufacturing, Vol. 24, No. 6, pp. 796-803.

5. Snider J., Yang B., and Lei S., (2008) "Laser Assisted Milling of Ceramic Matrix Composites", Ceramic Industry, Vol. 158, No. 3, pp. 24-26.

6. Yang, B., Deines, T.W., Geist, C.M., and Lei, S., (2007), "An Experimental Study of Laser Assisted Milling of Silicon Nitride Ceramic," Transactions of the North American Manufacturing Research Institution of SME, Vol. 35, pp.473-480.

7. Yang, B., Jiao, Y., and Lei, S., (2006), "A Study on the Effects of Microparameters on Macroproperties for Specimens Created by Bonded Particles," Engineering Computations: International Journal for Computer-Aided Engineering and Software, Vol. 23, No. 6, pp.607-631.

8. Lei, S. and Yang B., (2005), "Distinct Element Simulation of Machining Silicon Nitride Ceramics: Material Removal Mechanism", Transactions of the North American Manufacturing Research Institute of SME, Vol. 33, pp.485-492.

Working Journal Papers

9. Shen, X., Yang, B., and Lei, S., (2009), "Modeling and Simulation of Laser Assisted Machining of Silicon Nitride Ceramics with Distinct Element Method: Part II, Milling Simulation", For Journal of Manufacturing Science and Engineering, Transactions of the ASME.

10. Shen, X., Yang, B., and Lei, S., (2009), "Machining Simulation of Laser Assisted Milling of Silicon Nitride Ceramics with Distinct Element Method", For International Journal of Machine Tools and Manufacture.

Publications in Proceedings

1. Lei, S. and Yang B., (2008), "Laser Assisted Milling of Silicon Nitride Ceramic: A Parametric Study", Proceedings of 2008 NSF Engineering Research and Innovation Conference, Knoxville, Tennessee.

2. Yang, B., Deines, T.W., and Lei, S., (2007), "A Study on Workpiece Edge Chipping in Laser Assisted Milling of Silicon Nitride Ceramic", Proceedings of the 15th International Symposium on Electromachining, April 23-27, Pittsburgh, PA USA, P481-486.

3. Qian L., Hasson MR., Yang B., Li, S., (2007), "Feedrate Rescheduling in 3D Surface Machining with Various Methods", Proceedings of 17th Conference on Flexible Automation and Intelligent Manufacturing (FAIM 2007), Philadelphia, USA, June, 2007, pp. 897-904.

4. Yang, B. and Lei, S. (2004), "Distinct Element Simulation of Conventional and Laser Assisted Machining of Silicon Nitride Ceramics: Material Removal Mechanism," in Kovacevic, R. (Ed.), 2004 NSF Design, Service and Manufacturing Grantees and Research Conference Proceedings.